SYNTHESIZING FIELD AND EXPERIMENTAL TECHNIQUES TO INVESTIGATE THE ENIGMATIC PROCESSES OCCURRING AT THE BASE OF PYROCLASTIC CURRENTS

by

Nicholas M Pollock

A dissertation

submitted in partial fulfillment

of the requirements for the degree of

Doctor of Philosophy in Geosciences

Boise State University

August 2019

© 2019

Nicholas M Pollock

ALL RIGHTS RESERVED

BOISE STATE UNIVERSITY GRADUATE COLLEGE

DEFENSE COMMITTEE AND FINAL READING APPROVALS

of the thesis submitted by

Nicholas M Pollock

Thesis Title: Synthesizing Field and Experimental Techniques to Investigate the Enigmatic Processes Occurring at the Base of Pyroclastic Currents

Date of Final Oral Examination: 23 July 2019

The following individuals read and discussed the thesis submitted by student Nicholas Michael Pollock, and they evaluated his presentation and response to questions during the final oral examination. They found that the student passed the final oral examination.

Brittany Brand, Ph.D.	Chair, Supervisory Committee
Dorsey Wanless, Ph.D.	Member, Supervisory Committee
Olivier Roche, Ph.D.	Member, Supervisory Committee
Damiano Sarocchi, Ph.D.	Member, Supervisory Committee

The final reading approval of the thesis was granted by Brittany Brand, Ph.D., Chair of the Supervisory Committee. The thesis was approved by the Graduate College.

DEDICATION

To my parents.

For the countless sacrifices you made so that
your children could follow their dreams
and for the never-ending support that encouraged
them to keep chasing them.

ACKNOWLEDGEMENTS

First, and foremost, thank you to Dr. Brittany Brand for your constant guidance, support, and encouragement during my time in graduate school. I never expected to have the opportunities and experiences that you helped to make possible. From numerous field seasons, international conference experiences, and an 8-month stay at the Laboratoire Magmas et Volcans, the opportunities that you afforded me changed the direction of my life. You consistently provided a superb model of what a scientist should be – someone who not only thoroughly investigates important scientific questions, but is also able to communicate their findings with all audiences, and who supports the development and interest in the sciences through educational outreach activities. Thank you for everything.

Thank you also to my committee members: Dr. Dorsey Wanless for daily guidance and support both in my research and as a teaching assistant; Dr. Olivier Roche for hosting me during my 8-month stay in France and providing me with expert guidance for my experimental work; and Dr. Damiano Sarocchi for welcoming me during a summer stay in Mexico and numerous field seasons spent together.

Thank you to the entire Boise State University Department of Geosciences. Many people shaped my experience as a graduate student through their guidance and mentorship. This is certainly not an exhaustive list, but thank you to: Dr. Karen Viskupic, Dr. Matt Kohn, Dr. David Wilkins, Dr. Walt Snyder, Dr. Jim McNamara, Dr. Jen Pierce, and Dr. Mark Schmitz. You all taught me about being an effective researcher, an engaging instructor, and a community-engaged scientist.

Thank you to my fellow graduate students for cultivating the supportive and intellectually stimulating environment in which I've been fortunate to work for the past four and a half years. All my fellow students played a role in fostering this environment, but thank you especially to: Alex Witsil, Jake Anderson, Darin Schwartz, Aaron Marshall, Carson MacPherson-Krusty, Emma McCully, Andrew Gase, Claire Harrigan, Molly Anderson, and Robin Trayler.

Thank you to my Boise Family: Kayla Kinkead, Penny, and Balto. Your constant support and never-ending supplies of gummy bears throughout nearly my entire time in graduate school, and especially over the past few months, helped to keep me sane. Your patience and understanding during the long hours are appreciated, but your ability to provide welcome distractions and breaks from work are what ultimately helped me to make it through this process. I couldn't have done it without you.

Finally, thank you to my parents. From an early age, you instilled in all of your children the importance of education, and you made countless sacrifices to ensure that we had the best possible educational experiences. Thank you for allowing me to follow my passions, and for your constant reassurance that in pursuing my interests, I was making the right decision.

The completion of this dissertation certainly did not come about in isolation; everyone listed above (and countless others) contributed to this body of work. This achievement is also yours. Thank you.

ABSTRACT

Pyroclastic currents are the deadliest hazard associated with explosive volcanic eruptions. These gravity-driven currents consist of volcanic gases and solid particles that range in size from fine ash to boulders. The dangers associated with pyroclastic currents stem from their unpredictability and ability to travel extremely long distances, sometimes in excess of 100 km. To mitigate the risk to populations and infrastructure, we must understand the processes that control the runout distance of pyroclastic currents. The runout distance depends on the complex interplay of processes related to sediment transport, erosion, and deposition. Historically, studies focused on understanding sediment transport and deposition, but studies within the last 15 years demonstrate the important effect of erosional processes on the behavior of pyroclastic currents.

This dissertation research builds on recent studies to investigate how pyroclastic currents interact with the bed via erosion and mixing processes. I seek to answer questions related to the mechanisms by which erosion occurs, how the properties of the bed affect erosion and mixing processes, and how interactions between the flow and the bed affect flow behavior and runout distance. To address these questions, I combine detailed field studies of pyroclastic current deposits with analogue laboratory experiments that simulate pyroclastic currents in a controlled environment. Synthesizing these two approaches, field and experimental, allows for even greater insight into basal processes than either approach could provide on its own.

Ultimately, I show that erosion occurs via a fluid-like mixing process as a result of granular shear instabilities formed at the flow-bed interface. The mixing process generates wave-like structures at the contact between the flow and the bed, and the structures can be preserved in the deposits of both natural and experimental flows. The dimensions of the structures recorded in the deposits directly relate to flow parameters, such as velocity and thickness, at the time the structures formed. I apply scaling relationships derived from experimental data to sedimentary structures observed in the deposits of the pyroclastic currents produced during the May 18, 1980 eruption of Mount St Helens. This approach produces quantitative estimates of the flow velocity and thickness, important flow parameters that were unconstrained prior to this study. Additionally, the experiments suggest that the erosion and mixing processes decrease the runout distance of pyroclastic currents relative to non-erosive flows, which has important implications for hazard mitigation. Finally, the datasets produced both from the field and experimental studies can be used to test and refine numerical models of pyroclastic currents with the ultimate goal of improving the accuracy of risk assessments for these hazardous flows.

While this dissertation research improves our understanding of the erosion and mixing processes that occur at the flow-bed interface in pyroclastic currents, the final conclusions also beget new questions. Future studies should investigate other mechanisms by which erosion occurs because the mechanism discussed here is not likely to be the single way in which pyroclastic currents entrain bed material. Continued work to synthesize experimental and field studies has the potential to produce additional methods to derive quantitative information from natural pyroclastic deposits. Finally, the next major goal moving forward in the study of pyroclastic currents must be to obtain in situ measurements

of flows in real time. Such a dataset will provide the means to test many of the hypotheses set forth regarding the internal processes that govern the behavior of these dangerous volcanic phenomena.

TABLE OF CONTENTS

LIST OF TABLES

LIST OF FIGURES

LIST OF APPENDIX FIGURES

CHAPTER ONE: INTRODUCTION

Pyroclastic currents are gravity-driven mixtures of volcanic gases and solid particles that range in size from fine ash to large boulders (Figure 1.1a; Sparks et al. 1978; Sheridan 1979; Branney and Kokelaar 2002). Most commonly, these currents occur during explosive volcanic eruptions when an unstable ash column or lava dome collapses (Branney and Kokelaar 2002), but the flows can be generated via a number of other mechanisms as well (Williams 1957). Pyroclastic currents travel extremely long distances, occasionally greater than 100 km, at temperatures over 500° and speeds in excess of 100 m/s (Sparks et al. 1978; Sheridan 1979; Branney and Kokelaar 2002). This combination of parameters makes pyroclastic currents extremely hazardous to populations or infrastructure located along the current's flow path.

In order to mitigate hazards associated with pyroclastic currents, we must understand the processes that control the behavior and ultimately the runout distance of these dangerous flows. Unfortunately, making direct measurement of pyroclastic currents in real time is both difficult and dangerous due to their unpredictability and the presence of a dilute upper ash cloud that obscures the dense interior from view (Figure 1.1b). The dense basal portion of pyroclastic currents transports the vast majority of the flow mass (>95%; Breard and Lube, 2017) and, as a result, exerts strong control on the overall flow behavior (Valentine 1987). Therefore, understanding the processes that occur in this dense basal portion of the flow is essential for understanding the hazard potential of pyroclastic currents.

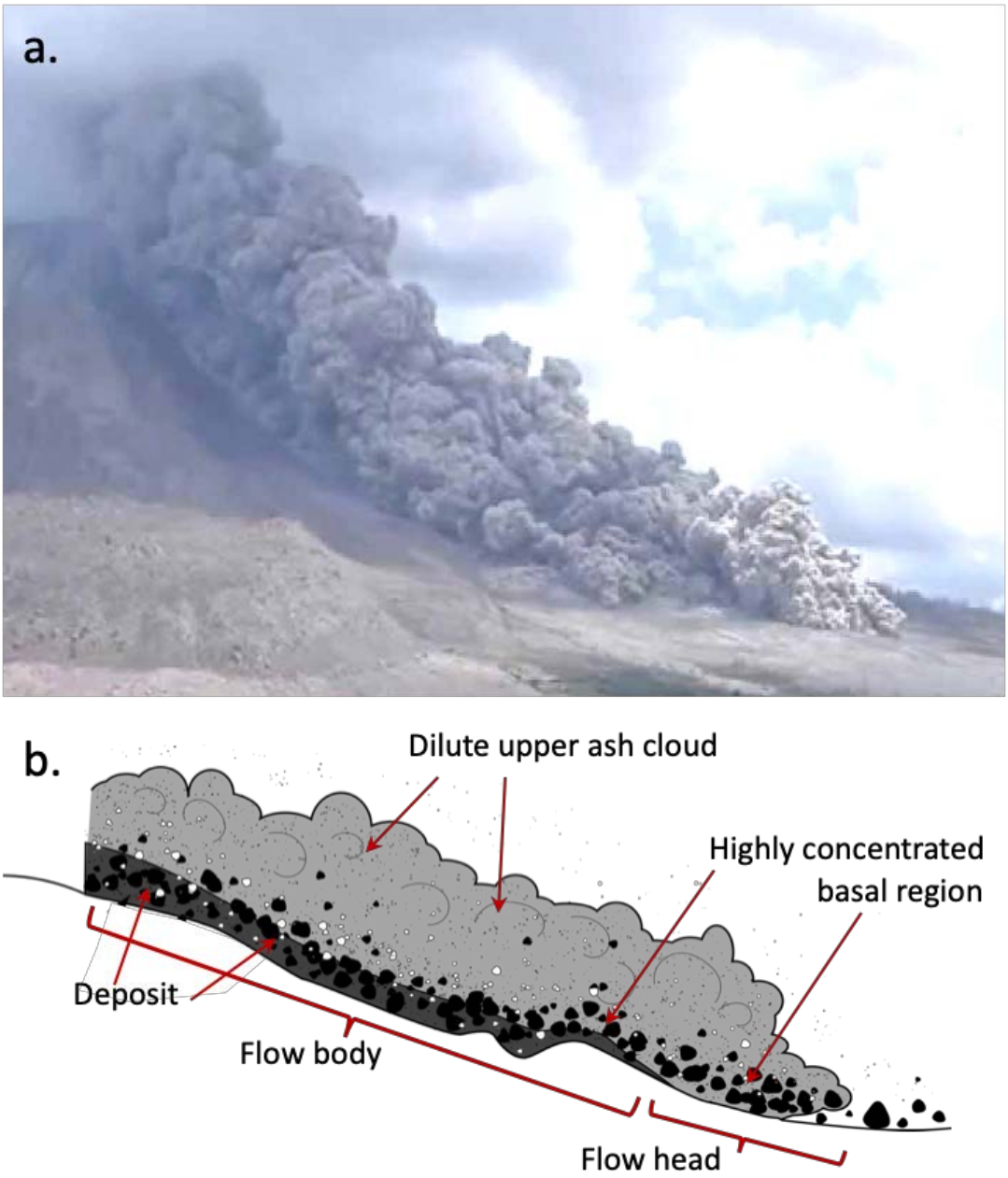

Figure 1.1(a) Image of pyroclastic current generated during an eruption at Sinbung Volcano in June 2015 (Photo: Tom Pheiffer, Volcano Discovery). (b) Schematic showing the generalized structure of a pyroclastic current with a dense basal region that is obscured from view by the presence of a large, buoyant upper ash cloud. The dense basal portion of the flow transports more than 95% of the total flow mass.

To overcome the lack of direct measurements of pyroclastic currents, we integrate observations of deposits left behind by pyroclastic currents with analogue experiments and

numerical models to investigate the processes occurring in the highly concentrated basal region. Detailed field studies of deposit characteristics lend insight into the mechanisms of sediment transport and deposition (e.g. Sparks 1976; Calder et al. 2000; Druitt et al. 2002; Brand et al 2014b), and in some cases can provide quantitative information about the flow conditions at the time of deposition (e.g. Clarke and Voight 2000; Dellino and La Volpe 2000; Taddeucci and Palladino 2002; Brand et al. 2014; Pollock et al. 2019). Analogue experiments and numerical models provide the ability to quantitatively investigate the behavior of simulated currents in controlled environments (e.g. Valentine and Wohletz 1989; Dartevelle 2004; Roche et al. 2010; Lube et al. 2015). These studies also give the opportunity to test physics-based models that describe the behavior of pyroclastic currents (e.g. Burgisser and Bergantz 2002; Dufek and Bergantz 2007b; Esposti Ongaro et al. 2012; Gueugneau et al. 2019), which are already widely used for hazard assessment and will only continue to grow in importance (Todesco et al. 2002; Esposti Ongaro et al. 2002).

For decades, both the field-based and experimental and numerical studies focused on investigating the mechanisms of sediment transport and deposition in pyroclastic currents (e.g. Sparks 1976; Wilson and Walker 1982; Dufek and Bergantz 2007). As a result, the community progressed significantly in our knowledge of these processes and their effect on the behavior and runout distance of pyroclastic currents. However, within the last 15 years, the community identified an additional set of processes that can also affect flow behavior and runout distance: erosional processes. While field evidence clearly demonstrates that pyroclastic currents erode material from the bed during transport (e.g. Rowley et al. 1981; Kieffer and Sturtevant 1988; Sparks et al. 1997; Cole et al. 1998; Calder et al. 2000; Brand et al. 2014b; Bernard et al. 2014; Pollock et al. 2016), only

recently have studies observed the effect of erosion and entrainment on flow behavior. Recent experimental investigations suggest that under specific conditions erosion of bed material can increase the runout distance of pyroclastic currents by up to 50% (Mangeney et al. 2010; Farin et al., 2014), which is a considerable margin of increase as it concerns the hazard assessment of these flows. While these recent advances demonstrate that bed erosion occurs and that it affects the overall behavior of pyroclastic currents, many questions remain regarding the processes occurring at the flow-bed interface.

Figure 1.2 Deposits from pyroclastic currents produced during the May 18, 1980 eruption of Mount St Helens.

This dissertation research investigates the erosion and mixing processes that occur at the flow-bed interface, which exert significant control on the behavior of pyroclastic currents. Specifically, I seek to answer the following questions:

1. By what mechanisms do pyroclastic currents erode material from the bed? Do the deposits record evidence of these mechanisms?
2. How do the characteristics of the bed affect the erosion processes? How do the characteristics of the bed affect overall flow behavior?
3. Once erosion occurs, how is the subsequent flow behavior affected?

4. Do the structures produced as a result of erosion contain information about the conditions in the flow at the time the erosion occurred?

To address these questions, my research combines detailed field studies of the pyroclastic current deposits with a series of analogue laboratory experiments that simulate pyroclastic currents. In the field, I investigate the deposits from the pyroclastic currents produced during the May 18, 1980 eruption of Mount St Helens (Figure 1.2). The deposits contain evidence for erosion in the form of both distinctive accidental lithics (Pollock et al. 2016) and sedimentary structures produced via mixing processes at the flow-bed interface (Figure 1.3a; Chapter 2; Pollock et al. 2019). The sedimentary structures record the conditions in the flow at the time the structures formed, and the dimensions of the structures provide quantitative information about important flow parameters.

In the laboratory, I use analogue experiments to investigate pyroclastic currents under controlled conditions (Figure 1.3b; Chapters 3 and 4). The experiments explore how the slope and size of particles in an erodible bed affect erosion and mixing processes occurring at the flow-bed interface. Two basal processes that affect the flow runout distance include the downward diffusion of gas into the porous bed and the mixing that occurs between the flow and the bed. The experiments demonstrate how the downward diffusion of gas into the bed effectively decreases the runout distance relative to flows travelling over a smooth surface (Chapter 3).

The mixing structures produced at the flow-bed interface have dimensions of height and length that scale with flow parameters such as velocity and flow height (Chapter 4). The experimental data defines quantitative scaling relationships between the structures and the flow parameters. The strength of this approach is ultimately shown in Chapter 4 where

I show how the scaling relationships derived from the experiments allow for the extraction of quantitative information from mixing structures preserved in the deposits of natural pyroclastic currents. Synthesizing the field and experimental approaches allowed for more in-depth answers to the initial research questions than either approach could have provided on its own.

Figure 1.3 (a) Sedimentary structure in the pyroclastic current deposits from Mount St Helens produced via mixing between the flow and the bed. For scale, person is 1.5 m tall. (b) Experimentally produced mixing structures. Spacing between black lines in background is 2 cm. By investigating the conditions under which these structures form in the laboratory, we can extrapolate those findings to the field.

As a direct result of this dissertation research, we better understand the processes that occur in the basal region of pyroclastic currents and how those processes affect the flow runout. The experiments produced quantitative relationships that can extract important information from structures contained in the deposits of pyroclastic currents.

This type of quantitative data about the flow conditions in natural pyroclastic currents is essential to farthering our understanding of these dangerous currents. The field-based datasets can be used to validate numerical models of pyroclastic currents, which are increasingly important in hazard and risk assessments. Finally, while this research answered a number of questions related to the behavior of pyroclastic currents, it has also opened a series of new questions that require answers and will need to be investigated in the coming years if we hope to continue farthering our understanding of these dangerous volcanic phenomena.

CHAPTER TWO: INFERRING PYROCLASTIC DENSITY CURRENT FLOW CONDITIONS USING SYN-DEPOSITIONAL SEDIMENTARY STRUCTURES

Abstract

The processes occurring in the basal region of concentrated pyroclastic density currents (PDCs) influence the mobility, runout distance, and damage potential of a current, but directly observing these processes is extremely difficult. Instead we must investigate the deposits to glean information regarding the conditions of sediment transport and deposition. The PDC deposits of the May 18, 1980 eruption of Mount St Helens (Washington, USA) contain sedimentary structures consisting of bed material reworked into undulose structures and recumbent flame structures. The structures vary over two orders of magnitude in size with lengths ranging from 8 cm to 18 m and heights ranging from 4 cm to 1.8 m. Despite the large range in sizes, the structures remain self-similar in form, suggesting a common mechanism for formation. The structures are interpreted as the record of granular shear instabilities, similar to Kelvin-Helmholtz instabilities, formed at the interface between a shearing, high concentration flow and the substrate in the moments just prior to deposition. The morphology of the structures suggests that the basal region of PDCs must be both highly concentrated and also highly mobile in the moments before final deposition, likely a result of elevated pore fluid pressures. We use a modified instability growth criterion to estimate PDC flow velocities at the time of formation; for the Mount St Helens PDCs, the velocity estimates range from 0.2 to 7.5 m s^{-1} with larger structures requiring higher flow velocities. Combining the velocity estimates with the dimensions of

the structures suggests deposition rates of 4 to 32 cm s^{-1}. Such high deposition rates indicate that the deposits likely accumulated in a stepwise manner, rather than either progressively or *en masse*. The structures suggest that sections of the deposit accumulated during punctuated periods of high deposition lasting at most a few seconds followed by periods of bypassing (i.e. non-deposition) or erosion lasting minutes to tens of minutes. Our findings motivate continued experimental and numerical work to understand how the formation of recumbent flame (and similar) structures affects subsequent flow behavior in terms of runout distance and hazard potential.

Introduction

The highly-concentrated basal region of pyroclastic density currents (PDCs) transports the vast majority of the total flow mass (Valentine 1987; Branney and Kokelaar 2002; Breard and Lube 2017); processes within this region influence the runout distance and damage potential of these dangerous volcanic phenomena (Sparks et al. 1993; Sulpizio et al. 2014; Dufek et al. 2015). Unfortunately, investigating the basal region of PDCs is notoriously challenging due to the difficulty of making direct observations in real time. Therefore, we investigate PDC deposits for insight into the enigmatic processes that occur at the flow base. PDC deposits record important information about transport and depositional processes occurring in the moments prior to, during, and following deposition (Branney and Kokelaar 2002). As such, we must continue to explore ways to derive quantitative information about the parent flows from PDC deposits. This type of field data is essential in assessing the accuracy of numerical models and ultimately understanding PDC behavior (e.g. Bernard et al. 2014; Roche 2015; Benage et al. 2016).

This study investigates deposits from topography-controlled, high-concentration PDCs, which generally have particle concentrations that range from a few volume percent to nearly max packing. The generalized structure of PDCs is derived primarily from experimental observations, suggesting a non-depositional flow head followed immediately by the flow body below which a deposit aggrades (e.g. Girolami et al. 2010; Roche et al. 2010; Roche 2012; Lube et al. 2015; Breard and Lube 2017). Conditions in the flow head include high shear stress (Girolami et al. 2010) and an underpressure at the flow base (with respect to a static substrate) that produces an upward directed pressure gradient (Roche 2012; Roche et al. 2013), both of which may aid in entraining material from the bed. The flow body is thought to be a relatively low-shear environment with high pore fluid pressures that would hinder substrate entrainment. Despite these observations from experiments, many questions remain regarding the conditions and processes occurring in the basal region of PDCs. This basal region is the portion of the current through which any sedimentation must occur, and similarly controls erosive processes. Therefore, understanding processes in the basal region is integral to the interpretation of flow characteristics from PDC deposits.

One way to understand the processes of mass and momentum transfer at the base of PDCs is to investigate depositional evidence for the shear conditions at the flow-bed interface. Uniform, undisturbed, and undeformed ash fall layers overlain by thick ignimbrites are often cited as evidence that PDCs can be largely non-erosive and non-shearing (Valentine et al. 1989; Cas et al. 2011). Occasionally, however, flow-bed contacts suggest significant shear stress exerted on the bed. A number of studies identify depositional evidence for erosional channels (Sparks et al. 1997; Calder et al. 2000; Brand

et al. 2014b; Gase et al. 2017) or substrate derived lithics in subsequent PDC deposits (Buesch 1992; Bernard et al. 2014; Brand et al. 2016; Pollock et al. 2016), both of which may be related to shear stress exerted on the bed by the PDC. However, observations of deposits alone lend little insight into how these processes occur or how substrate erosion affects flow behavior.

The studies listed above describe outcrops that either demonstrate that erosion occurred while PDCs passed through an area, leaving behind scours and channels, or that PDCs deposited material eroded from some upstream source; fewer studies discuss outcrops with evidence for substrate erosion or deformation that occurred syn-depositionally. Syn-depositional substrate deformation captures in a single outcrop both the deformed substrate and deposits from the flow responsible for the deformation. Such an outcrop lends insight into the complex interplay between shear stress, erosion, and deposition occurring at the flow-bed interface.

Features associated with syn-depositional substrate deformation, including reverse faults (LaBerge et al. 2006), vortical structures at dune crests (Giannetti and Luongo 1994) and overturned and recumbent vortical features within well-bedded deposits (Douillet et al. 2015; Douillet et al. 2018), appear in the deposits from both dilute and concentrated PDCs. For example, Douillet et al. (2018) described ‘shark fin’ structures that occur with periodicity in the deposits of dilute PDCs at Tungurahua Volcano, and attribute them to shear horizons related to traction carpets. For high-concentration PDCs, LaBerge et al. (2006) described reverse faults formed syn-depositionally at the base of the Peperino Tipico Ignimbrite, at Monte Cimino, Italy. The reverse faults show that high-concentration PDCs can also transmit high shear stress to the substrate syn-depositionally. Finally,

Rowley (2010) proposed a few examples of shear-related deformation structures in PDC deposits. The most notable structure is from the Tanjung formation in the Banten province of West Java, Indonesia, and they proposed that the structures may be related to shear instabilities formed at the base of PDCs. The above field studies all demonstrated that behavior in the basal region of PDCs can transition back and forth from shearing to depositional over short timescales and that evidence for basal shear can be recorded in the PDC deposits, but using syn-depositional sedimentary structures to extract quantitative information about parent PDCs remains relatively unexplored.

Here we present evidence for syn-depositional basal shear recorded in deposits from the high-concentration PDCs produced during the May 18, 1980 eruption of Mount St Helens (MSH), USA. The PDC deposits contain numerous convex, undulose structures (Figure 2.1a) as well as recumbent flame structures (Figure 2.1c) located at contacts between flow units as well as within individual units. The undulose and recumbent flame structures range in size over almost two orders of magnitude, but are self-similar in form, potentially suggesting a similar mechanism of formation. The structures observed in the MSH deposits closely resemble sedimentary structures produced in previous analogue and numerical experiments (e.g. Goldfarb et al. 2002; Ciamarra et al. 2005; Rowley et al. 2011). We compare the recumbent flame structures in the deposits to similar structures produced in controlled laboratory environments to investigate the conditions under which the MSH flame structures formed. We use the dimensions of the recumbent flame structures to constrain flow concentration and depositional style as well as extract quantitative information about important flow parameters including basal slip velocity and deposition rates.

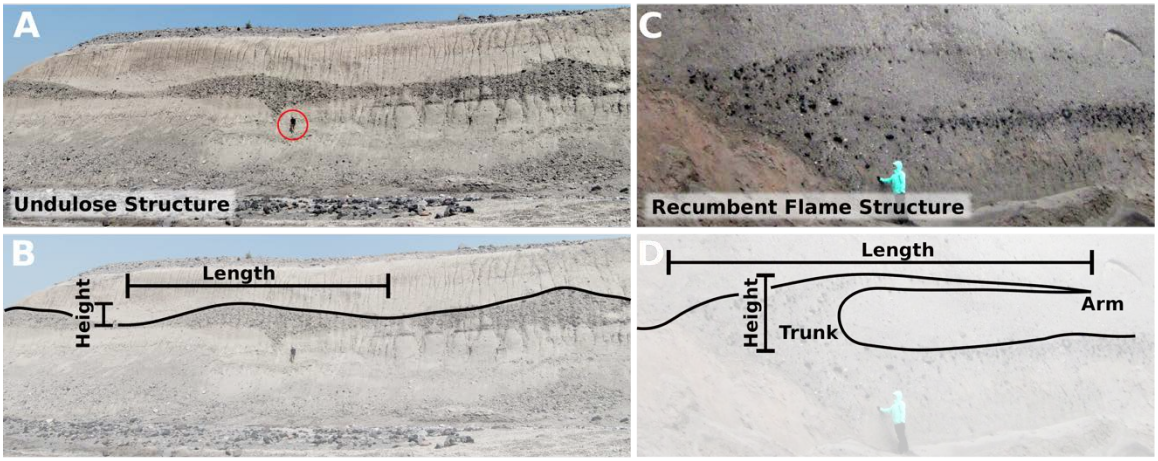

Figure 2.1 (a) Set of three undulose structures composed of course lithics found in the PDC deposits at Mount St Helens. Person shown for scale in red circle is 1.6 m tall. (b) Sketch showing measurement scheme for undulose structures where length is the distance between the toughs on either side of a crest, and height is the maximum vertical displacement from the contact. (c) Example of recumbent flame structure found in the PDC deposits at Mount St Helens where a substrate composed of coarse lithics was sheared and partially mixed into the current as it flowed from left to right. Image modified from Brand et al. (2017). (d) Sketch showing measurement scheme for recumbent flame structures.

Terminology

In this work, we will present two types of sedimentary structures observed in the PDC deposits from the May 18, 1980 eruption at MSH: undulose and recumbent flame structures. Both types of structures consist of a basal layer composed of reworked bed material and an overlying upper layer that shows no evidence of internal deformation. The deposits at MSH contain undulose structures that appear as a wavy, convex, basal layer consisting of alternating troughs and crests (Figure 2.1a). The recumbent flame structures have a concave lee surface with an overhanging arm, where the basal layer protrudes up into the overlying layer before bending, becoming sub-horizontal, and thinning in the downflow direction (Figure 2.1c).

The undulose structures share some morphologic similarities with traditional fluvial or aeolian bedforms such as regular spacing and their general convex shape (cf. Allen 1984). However, unlike ripples and dunes, the undulose structures generally lack internal stratification, a key characteristic of traditional bedforms (e.g. Bristow et al. 2000; Rodríguez Santalla et al. 2009; Martinius and Gowland 2011). For this reason, we use the non-genetic, descriptive term undulose structures to describe the MSH structures.

Additionally, features similar to the recumbent flame structures described herein are given many different names in the literature, including sheared, recumbent, or truncated flame structures (Sparks et al. 1985; Matsumoto et al. 2008; Rowley 2010; Rowley et al. 2011), vortical reworking features (Rowley et al. 2011), sheared wavelike structures (Roche et al. 2013), erosion waves (Farin et al. 2014), overturned laminae/ beds or vortex bedding (Douillet et al. 2015), and 'shark fin' structures (Douillet et al. 2018). Flame structure is a traditional soft sediment deformation term that describes a finger-like protrusion of a basal layer into an overlying layer. Unfortunately, in the literature, the term "flame structure" has become intertwined with formation mechanisms: either an unstable loading of a dense layer atop a less dense layer (i.e. Raleigh-Taylor instabilities) or earthquake-induced liquefaction, depending on the study (see Shanmugam 2017 for discussion of issues with terminology). Although the issue of implicit interpretation exists in the literature for the term "flame structures", the structures observed in the MSH deposits more closely resemble (recumbent) flame structures than any other previously described sedimentary structures. To avoid adding to the already cumbersome terminology and the genetic implications associated with some of the other terminology mentioned above, we follow Rowley et al. (2011) and use the non-genetic term recumbent flame structure to

describe the structures observed in the MSH PDC deposits. However, we ultimately interpret a mechanism of formation for the recumbent flame structures that differs from either an unstable density contrast or earthquake-induced liquefaction.

Geologic Setting

Previous Investigation of PDC Deposits from the May 18, 1980 Eruption of MSH

The May 18, 1980 eruption of MSH included a series of concentrated PDCs that produced stacks of sheet-like and elongated tongue and lobe-like deposits throughout the pumice plain (Figure 2.2a and 2.2b; Rowley et al. 1981; Kuntz et al. 1981). Following the eruption, vertical exposures of the PDC deposits existed only in walls of a few phreatic explosion craters. Consequently, for the few years following the eruption, observations of the deposits were mostly limited to surficial characteristics (Kuntz et al. 1981; Rowley et al. 1981).

Surficial observations allowed for investigation of at least the uppermost, late-stage flows. For example, levees and longitudinal ridges on the surface of the deposits constrained local flow directions for the latest PDCs (Rowley et al. 1981; Kuntz et al. 1990). Rowley et al. (1981) additionally describe the treacherous nature of walking on the deposits due to its quicksand-like nature. They note that a large rock thrown into the deposits caused “splashes and waves and tiny jets of air to escape from the surface”. Rowley et al. (1981) also describe deflation of the PDC deposit surfaces of 1 m or more in the hours to days following emplacement. Together, these observations support an interpretation of low permeability deposits with associated high gas retention rates. While these surficial observations are important, the lack of incision through the deposits in 1980

and 1981 prohibited rigorous investigation of PDCs deposited in the early or middle portions of the eruption.

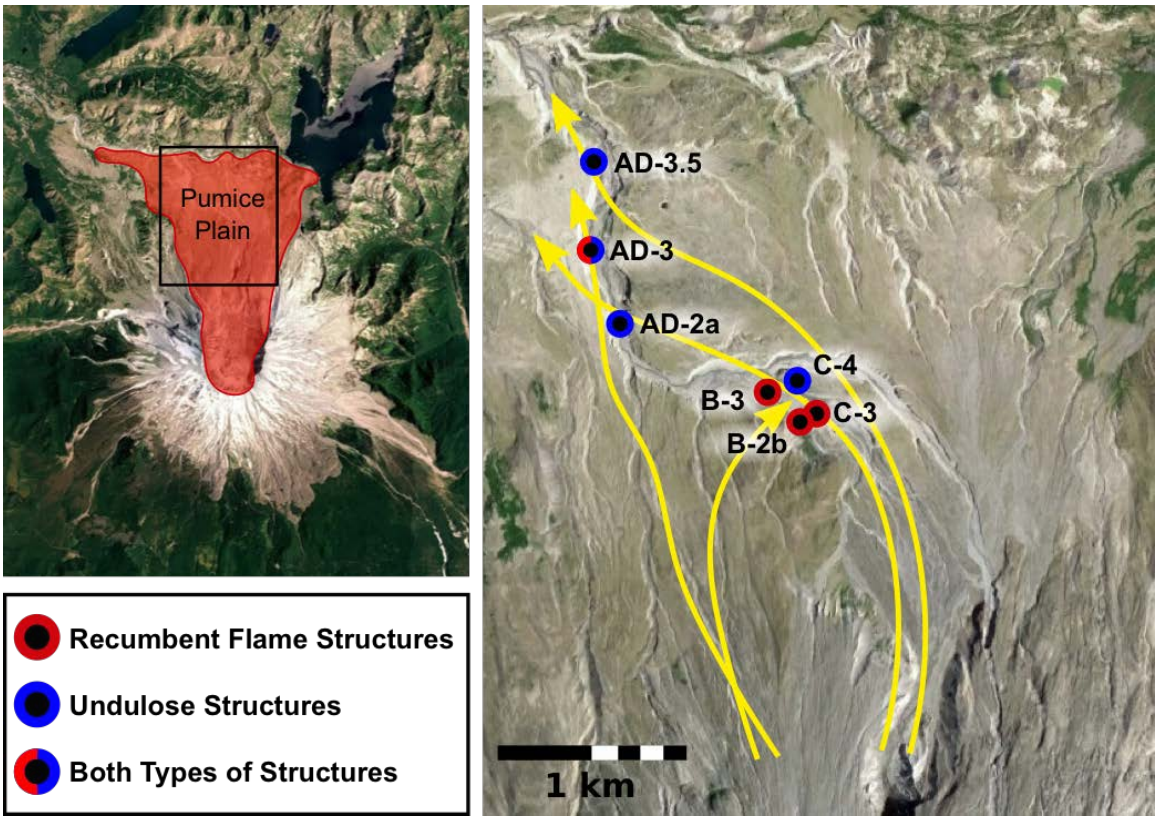

Figure 2.2 (a) Aerial image of MSH showing extent of PDC deposition during the May 18, 1980 eruption. (b) Inset from (a) showing locations of outcrops containing recumbent flame structures (red circle), undulose structures (blue circle), or both (red/blue circle). Yellow lines indicate inferred PDC flow paths from Brand et al. (2014). Both images from Google ©2019, Map data ©2019.

In the nearly 40 years since the eruption, incision through the PDC deposits produced up to 40 vertical meters of new exposures along drainages cut throughout the pumice plain. A flood event in 1982 exposed more than 10 m of new outcrop in the central pumice plain (Simon and Klimetz 2012). Criswell (1987) used the new exposures to produce the first detailed, chronostratigraphic correlation of the PDC deposits. Their study combines visual observations made during the eruption with a detailed investigation of the

exposed deposits to correlate deposit characteristics to the eruption chronology. From their observations, Criswell (1987) distinguishes a lower, middle, and upper pyroclastic flow sequence and correlates each sequence to time periods during the May 18 eruption. However, Criswell (1987) also note that at the time of their study the lower sections of the deposits were not exposed.

Additional incision through the PDC deposits continued over the two decades following the study of Criswell (1987), resulting in an addition 20-30 m of new exposures (Simon and Klimetz 2012). Modern day outcrops include complete incision through what Criswell (1987) calls the lower sequence, as well as exposure of the basal contacts of the PDC deposits with both the debris avalanche and lateral blast deposits. Following this additional incision, Brand et al. (2014b) revisited the PDC deposits and used the new exposures to refine PDC units and their correlation to the eruptive chronology. The following abbreviated chronostratigraphic description of the PDC deposits follows from observations of Christiansen and Peterson (1981), Rowley et al. (1981), Criswell (1987), and Brand et al. (2014b).

Chronostratigraphy of PDC Deposits at MSH

The May 18, 1980 eruption of Mount St Helens began with the largest volcanic flank failure in recent history when the over-steepened north flank of the volcano catastrophically failed and slid off to the north towards Johnston Ridge (Christiansen and Peterson 1981; Glicken 1996). Removal of the north flank led to rapid decompression of the cryptodome and hydrothermal system and initiated the lateral blast that travelled more than 20 km to the north as a dilute density current (Christiansen and Peterson 1981).

Following the landslide and the lateral blast, the eruption column stabilized into a Plinian ash column that rose 20 km into the atmosphere (Christiansen and Peterson 1981).

The ash column steadily persisted until the early afternoon when the column destabilized and began to collapse, generating the series of PDCs that deposited throughout the pumice plain (Christiansen and Peterson 1981; Criswell 1987). Three main periods of PDC emplacement occurred during the afternoon of the eruption: an initial PDC phase when intensity of the eruption continued to build, a climactic phase, and a final phase associated with the waning of eruptive intensity (Criswell 1987; Brand et al. 2014b). Brand et al. (2014b) describe five primary PDC flow units deposited during these three phases. Units I and II are dominantly diffusely-stratified to massive lapilli tuffs emplaced during the first PDC phase. The PDCs that deposited Units I and II were confined by pre-existing topography and had highly concentrated basal regions that fluctuated between high and low shear environments (Brand et al. 2014b). During the climactic phase of the eruption, the most voluminous PDCs deposited Units III and IV, both dominantly block-rich massive lapilli tuff with occasional lithic breccia and pumice lens facies. Brand et al. (2014b) interpret that the Unit III and IV PDCs had highly concentrated basal regions and travelled up and around debris avalanche hummocks, eventually burying the pre-existing topography. The PDCs produced during the final phase are only found across the surface of the pumice plain and not exposed in outcrop; as such, Unit V is not discussed.

PDC Flow Directions

Previous studies constrain PDC flow directions in a variety of ways including both surficial features and outcrop observations. As mentioned above, Rowley et al. (1981) describe levees and ridges that define flow directions for the PDCs exposed at the surface.

Kuntz et al. (1990) uses these surficial structures to map detailed flow directions for late-stage surficial PDCs. Brand et al. (2014b) combine the surficial observations of Rowley et al. (1981) and Kuntz et al. (1990) with outcrop scale observations to refine estimates of flow directions. Synthesized observations of structural features such as levees, erosional scours, and pumice lens orientations provide information about flow direction at the outcrop scale (Brand et al. 2014b). Because topography exerts control over the behavior of dense PDCs (De Vita et al. 1999; Rossano et al. 2004), observations of paleotopography, and specifically paleovalleys, can also lend additional insight into flow directions for the PDCs.

Methods

Over the course of three rigorous field campaigns, we identified 22 total syn-depositional sedimentary structures: 11 undulose structures and 11 recumbent flame structures. While the number of observed structures is somewhat limited, very few descriptions of similar structures appear in the PDC literature, especially for concentrated PDCs (e.g. Giannetti and Luongo 1994; Rowley 2010; Douillet et al. 2015). Additionally, the structures are well-distributed across seven outcrops that range from proximal to distal (Figure 2.2b). By synthesizing our observations of these rare structures with the wealth of pre-existing studies on the MSH PDC deposits, analogue experiments, and numerical modeling, we believe the structures lend important insight and quantitative information about the complex processes occurring in the basal region of PDCs.

To investigate the structures, we collected scaled digital images of each structure and measured its dimensions. When accessible, we excavated into the deposits to a minimum of 30 cm to ensure the observed structures were not surficial features related to

fluvial deposition or reworking. Over the three field campaigns, we did not find any structures that were purely surficial.

We describe both the undulose and recumbent flame structures in terms of their length and height. For undulose structures, the length is measured as the distance between successive troughs, and the height is the distance from the lowest part of a trough to the top of the crest (Figure 2.1b). Recumbent flame structures have two main structural components, here termed the trunk and the billow (Figure 2.1d). The trunk is the main body of the recumbent flame structure that protrudes up into the overlying layer from the otherwise horizontal substrate. The billow is the sub-horizontal arm of the wave that extends downstream and thins away from the trunk. For the recumbent flame structure, we define the length as the distance from the initial upward perturbation of the trunk to the end of the billow, and the height is the maximum upward displacement of the substrate from the otherwise horizontal contact. Although the morphology of the two types of structures is different, we consider the measurements for length and height comparable. We then use linear regression to investigate the correlation between the length and height of structures of different sizes.

Results

Both the recumbent flame and undulose structures are found throughout the MSH PDC flow Units II, III, and IV; the structures are located both at the contact between flow units and within single flow units. The recumbent flame structures at MSH range in size over two orders of magnitude, with lengths from 0.08 m to 17.9 m and heights from 0.04 to 1.80 m. Despite this significant range in size of the structures, they are self-similar in form; the length of the structures scales closely with the height (R^2=0.93). The undulose

structures range in length from 4.0 to 35.7 m and heights from 0.25 to 4.1 m (Table 1). Most undulose structures are relatively symmetric and internally massive (Figures 2.1a, 2.4b, 2.4c), while others are asymmetric and have shorter upstream and longer downstream sides. One undulose structure shows faint internal bedding parallel to the lee face (AD-2a; Figure 2.4a). Similar to the recumbent flame structures, the length of the undulose structures scales with height (R^2=0.96; Figure 2.5). No significant trends exist between height or length and distance from the vent for either type of structure.

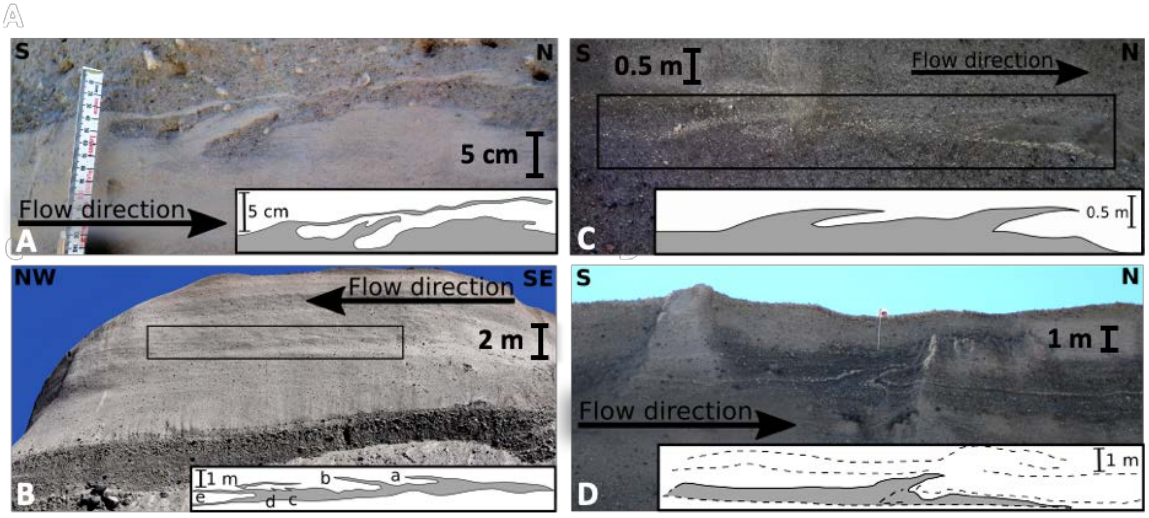

Figure 2.3 Examples of recumbent flame structures found in outcrops B-3 (a), B-2a (b), and AD-3 (c and d) with insets showing their structure (see Figure 2.2 for outcrop locations). Images previously published in Brand et al. (2017). See Table 1 for outcrop details.

The deformed bed is primarily earlier PDC deposits (Figures 2.3b-2.3d, 2.4b-2.4c), but also includes debris avalanche deposits (Figure 2.4a) and a single light-colored ash layer (Figure 2.3a). The debris avalanche deposits result from the catastrophic landslide that initiated the eruption and have a bimodal grain size distribution, with high proportions of fine ash and large blocks (Glicken 1996). In its only known exposure, the fine-grained,

well-sorted ash layer sits just above the debris avalanche deposit (Figure 2.3a). Due to the well-sorted nature of the layer and its stratigraphic setting, we interpret the ash as co-ignimbrite fallout either from the lateral blast or one of the earlier PDCs. One set of undulose structures occurs in contact with debris avalanche deposits (Figure 2.4a), and a single set of recumbent flame structures occur in contact with the co-ignimbrite ash deposit (Figure 2.3a). The recumbent flame structure formed from the ash layer is the only structure with a basal layer that is significantly more fine-grained than the upper layer; in all other examples, the basal layer is either coarser or similar to the upper layer in its mean grain size.

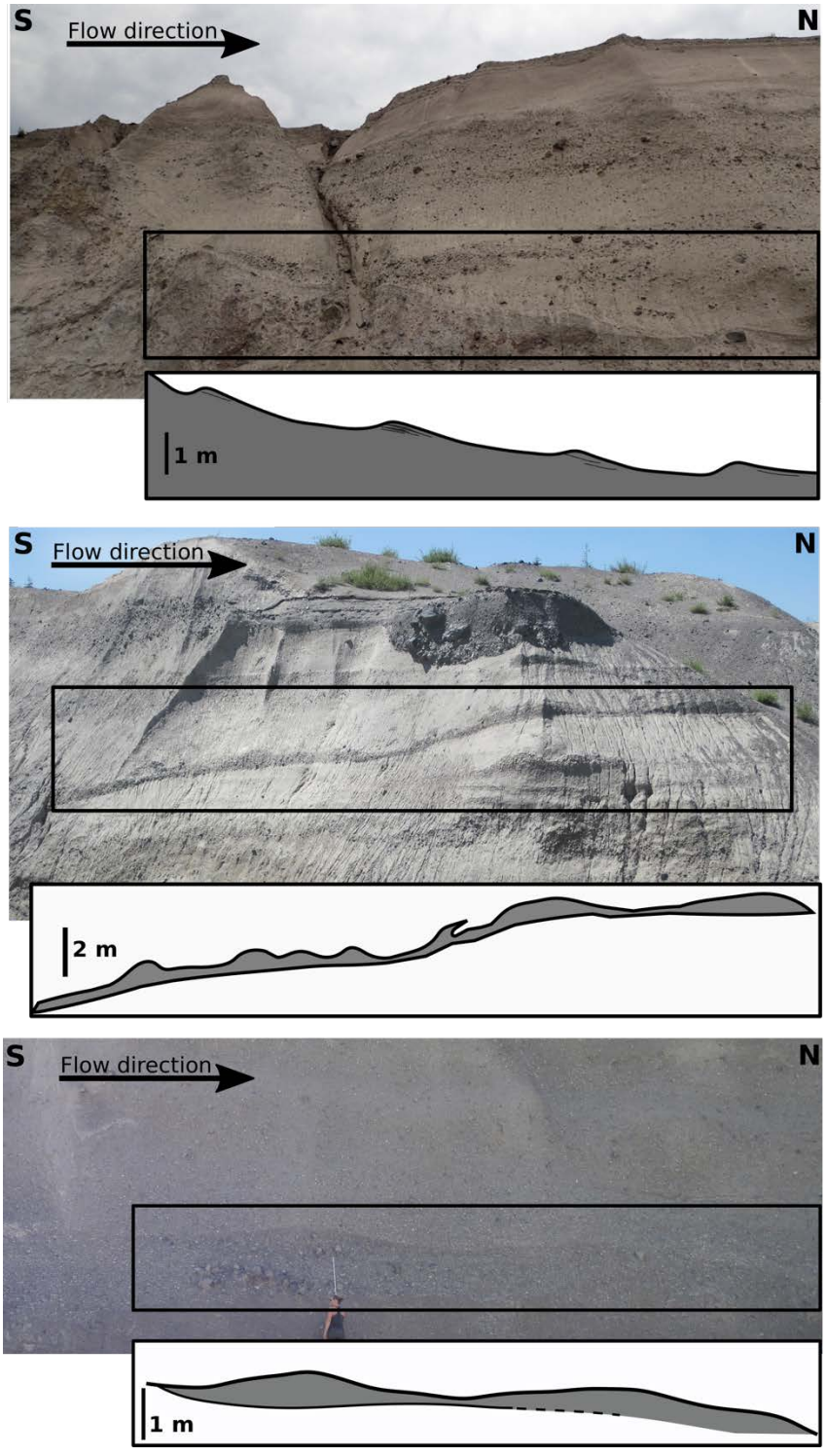

Figure 2.4 Examples of undulose structures found in the outcrops AD-2a (a), AD-3.5 (b), and AD-3 (c) with insets showing their structure. See Figure 2.2 for outcrop locations and Table 1 for outcrop details.

The vast majority of undulose and recumbent flame structures occur with both the upper and basal layers consisting of PDC deposits. Given the general similarity of the PDC deposits, a distinct textural difference is necessary to observe the deformed contact. For example, a pumice-rich (e.g. Figure 2.3d) or dense lithic block-rich basal layers (e.g. Figure 2.1a, 2.1c, 2.4b) can define the contact and delineate the structure.

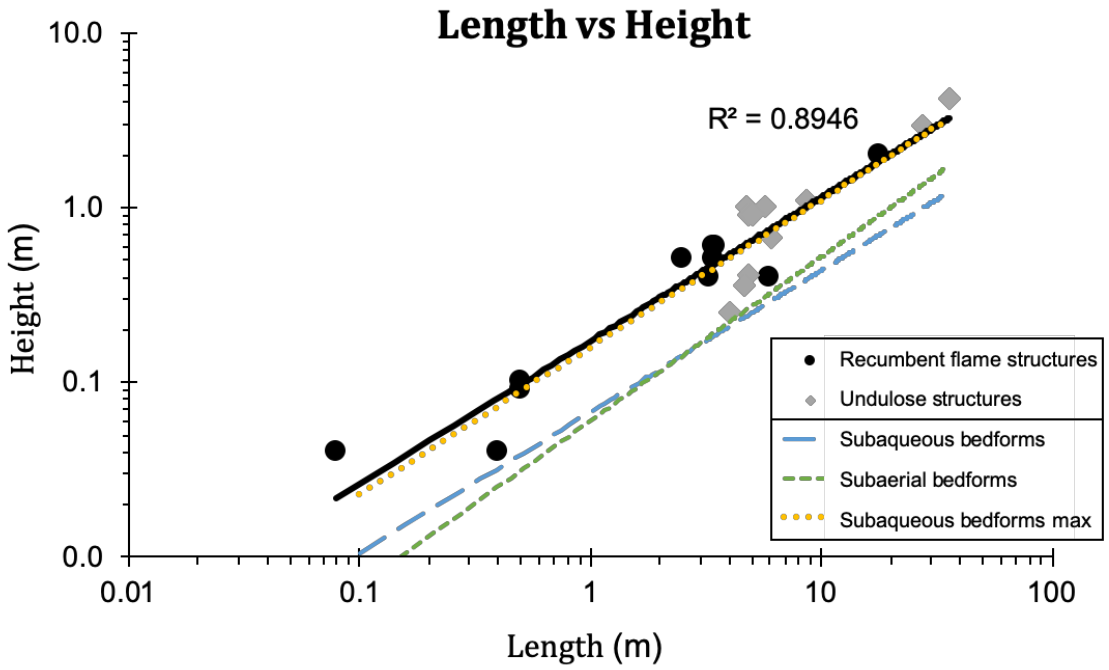

Figure 2.5 Aspect ratio of the structures plotted as length versus height. Black circles indicate recumbent flame structures, gray diamonds indicate undulose structures, and solid black line is best-fit for all MSH structures. Also plotted are best-fit lines for subaqueous (blue long dashes) and subaerial (green short dashes) bedforms and the maximum height for subaqueous bedforms (yellow dots) from Flemming (1988).

Discussion

Interpretations from Field Observations

The morphology of the structures allows for some general interpretations about flow characteristics including shearing conditions, flow direction, concentration, and

deposition rates. The undulose and recumbent flame structures comprise a lower layer that is deformed and elongated, suggesting that the PDCs interacted with and deformed the bed material during transport (cf. Owen et al. 2011). The elongation of the structures suggests some amount of shear exerted on the flow-bed interface by the overriding flow as is observed in the deposits of other high-energy currents including tsunamis (cf. Matsumoto et al. 2008). Therefore, we assume the elongation direction of the undulose and recumbent flame structures can be used a reliable indicator of approximate local flow direction. This idea is farther supported by the coincidence of flow directions indicated by the undulose and recumbent flame structures with previous interpretations of flow direction (Brand et al. 2014b).

Previous work on the MSH deposits interpret that the PDCs produced on May 18 were highly concentrated based on depositional characteristics (Brand et al. 2014b, 2016; Pollock et al. 2016). Additionally, Breard et al. (2018) introduced a nondimensional dense-dilute number (T_{de-di}) that predicts the dominant transport mode (dense or dilute) based on geometry and granulometry of the resulting deposit. The dense-dilute number is defined as (Breard et al. 2018):

$$T_{de-di} = \frac{A^3 d_{S,1/2}}{V^{5/3} L^2} \qquad (Eqn.\ 2.1)$$

where A is the inundation area, V is the total deposit volume, L is the runout distance, and $d_{S,1/2}$ is the Sauter mean diameter at one half of the total runout. The Sauter mean diameter characterizes the importance of fluid drag on particle transport (Breard et al. 2018, 2019) and can be estimated by:

$$d_S(mm) = 2^{-\left[\mu_{PSD}(\phi) + \frac{ln2}{2}{\sigma_{PSD}}^2(\phi)\right]} \qquad (Eqn.\ 2.2)$$

where μ_{PSD} and σ_{PSD} are the mean and standard deviation of the particle size distribution in ϕ units (full derivation in Breard et al. 2019). The transition in transport mode based on T_{de-di} occurs at ~$6{\cdot}10^{-2}$, with greater values of T_{de-di} indicating dilute transport and values of T_{de-di} less than ~$6{\cdot}10^{-2}$ indicating dense transport (Breard et al. 2018). We calculate T_{de-di} for the MSH PDC deposits using deposit geometry data from Rowley et al. (1981) and granulometry data from Brand et al. (2014b). The T_{de-di} for the MSH deposits is $4.5{\cdot}10^{-4}$, which thus suggests the PDCs transported the bulk of their material as high-concentration, dense flows.

Two additional observations of the recumbent flame structures farther support the interpretation of concentrated PDC conditions; first, the billow of the wave is generally at or above the highest point in the trunk of the wave, and second, the billow (composed of bed material) is underlain by flow deposit (Figure 2.3). If the flow were significantly expanded relative to the bed (i.e. low particle concentration) as the flow came to rest, the flow material underneath the billow would compact due to expelling of the gas (Figure 2.6). The compaction of the flow material would cause the billow to be depressed relative to the highest point of the wave trunk. But, because the billow is at or above the height of the trunk, compaction of the flow deposit during deposition must have been minor, indicating that the basal region of the flow was highly concentrated while the recumbent flame structure was growing and being deposited.

We interpret that the undulose structures also form due to shear exerted on the flow-bed interface; however, the lack of a billow prohibits constraining the flow concentration. One possibility is that the undulose structures form in lower concentration flows that cannot sustain the formation of a billow, and any material that is momentarily uplifted quickly

falls back to the bed (Figure 2.6). A second possibility is that the undulose structures form in flows of similar concentration to the recumbent flame structures, but the undulose structures represent an earlier phase of growth. From both analogue and numerical experiments, a shearing, unstable interface is known to evolve from wavy, undulose forms to breaking waves (Goldfarb et al. 2002; Ciamarra et al. 2005), and the undulose structures possibly represent an earlier phase in the evolution of the recumbent flame structures.

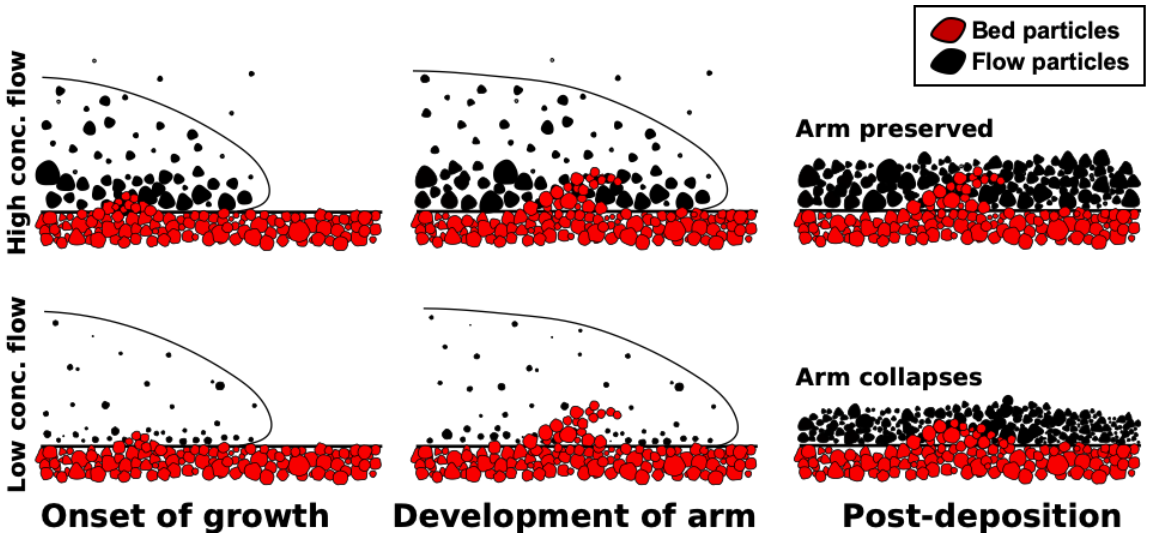

Figure 2.6 Schematic of the onset, growth, and deposition of granular shear instability at the flow-bed interface for different concentration currents. PDCs with high-concentration basal regions are able to preserve recumbent flame structures, while low concentration PDCs are not able to support the arm of the recumbent flame structure and it collapses back to the bed.

Preservation of the recumbent flame structures in the deposits suggests the behavior in the basal region must quickly transition from non-depositional and shearing to rapid deposition. Growth of the recumbent flame structures necessarily requires uplift of the bed (Matsumoto et al. 2008), and, if the bed is being uplifted, the flow (at least locally) must be non-depositional. But if the flow remains non-depositional following the onset of uplift, the structure will be completely amalgamated into the flow body, removing any evidence

that the structure ever formed (Rowley et al. 2011). The preservation of the recumbent flame structure thus requires rapid deposition on the order of the height of the structure in the moments following the onset of bed uplift. Such rapid deposition implies that, given the thickness of the deposits, a current sustained for minutes to hours must only be depositing intermittently, with significant periods of non-deposition.

Mechanism of Formation

Recumbent Flame Structures Related to Traditional Bedforms?

Flemming (1988) compiled measurements of more than 1500 subaqueous and subaerial ripples and dunes and extracted relationships between bedform spacing and height for each group. Figure 2.5 shows the calculated least squares regression line for the relationship between spacing and height for subaqueous (blue line) and subaerial (green line) bedforms. As Flemming (1988) demonstrates, a different length to height relationship exists for subaqueous versus subaerial bedforms. A strong correlation exists between the height and the length of the MSH structures, but the relationship deviates from that of the subaqueous and subaerial bedforms (Figure 2.5). The heights of sedimentary structures in the MSH PDC deposits exceed the average height for either subaerial or subaqueous bedforms of the same length. In addition, more than half (55%) of the structures measured in the deposits at MSH plot above the maximum height of subaqueous bedforms of the same length (yellow line).

Similar to how different relationships exist for bedforms formed in water versus wind, the difference in transport processes and material for PDCs could explain the different relationship. However, the lack of internal stratification in all but one structure additionally distinguishes the MSH structures from traditional bedforms. While some

similarities in morphology exist, the lack of internal stratification and the differences in length to height relationships suggest that a different mechanism produced the structures observed in the MSH PDC deposits.

Recumbent Flame Structures Related to Traditional Soft Sediment Deformation?

Soft sediment deformation encompasses over 120 distinct features that record deformation of sediments prior to lithification (Shanmugam 2017). Two of the most common types of soft sediment deformation structures, load casts and flame structures, occur when a high-density layer sits unstably atop a lower density layer. The high density material sinks down into the underlying layer creating load casts, while finger-like injections of the less dense material protrude into the overlying layer creating flame structures (Allen 1984; Collinson and Thompson 1989; Collinson 1994; Owen 1996; Dasgupta 1998; Chiarella et al. 2016; Shanmugam 2017). Traditional flame structures are natural examples of Rayleigh-Taylor instabilities (Allen 1984). While classic flame structures rise vertically from the interface, they can also be sheared or recumbent in nature (Dasgupta 1998; Matsumoto et al. 2008). The recumbent flame structures somewhat resemble the recumbent flame structures in the MSH PDC deposits. However, key observations suggest that the MSH recumbent flame structures are not traditional flame structures.

At MSH, the recumbent flame structures most commonly occur at an interface between or within PDC deposits. Both the upper and lower layers commonly contain material of the same size and density characteristics. In the moments prior to final deposition of a PDC, the flow will be slightly expanded relative to the bed due to particle collisions during transport (Savage 1998) and diffusion of pore fluid pressure (Druitt et al.

2007; Breard et al. 2019). Therefore, the density of the PDC will always be equal to or less dense than the resulting deposit. These observations suggest that the vertical arrangement of a flowing PDC and an underlying deposit will be stable in terms of density stratification, prohibiting the formation of Raleigh-Taylor instabilities. Additionally, in some cases, the basal layer contains a high proportion of dense lithic blocks relative to the upper layer, indicating a higher bulk density relative to the upper layer (e.g. Figure 2.1c), farther inhibiting the formation of traditional flame structures.

Although the recumbent morphology of the recumbent flame structures does suggest interaction between a fluid-like flow and a readily-deformable bed, the recumbent flame structures cannot be traditional flame structures. So-called recumbent flame structures in tsunami deposits have been interpreted to record syn-sedimentary deformation of the substrate due to shear stress exerted on the bed by the runup of the tsunami (Matsumoto et al. 2008). A similar, alternative mechanism must be responsible for the formation of the MSH recumbent flame structures.

Undulose and Recumbent Flame Structures as Granular Shear Instabilities

Previous experimental studies investigating the behavior of granular flows have produced structures similar to those observed in the PDC deposits at MSH (e.g. Goldfarb et al. 2002; Ciamarra et al. 2005; Rowley et al. 2011; Roche et al. 2013; Farin et al. 2014). For example, Goldfarb et al. (2002) investigated the behavior of two parallel granular flows traveling next to each other and shearing along a vertical contact. As slope increases, the contact between the two flows evolves from planar to wavy and eventually to the formation of breaking waves. Goldfarb et al. (2002) attributed the formation and growth of the waves to granular shear instabilities formed at the unstable interface between the two flows.

However, the experimental flows of Goldfarb et al. (2002) sheared along a vertical contact and waves grew in the horizontal plane, without the restorative force of gravity. The aspect ratio and overall structure of the recumbent flame structures produced by Goldfarb et al. (2002) were similar to those observed by us in the PDC deposits at MSH ($R^2 = 0.96$), but the recumbent flame structures at MSH exist in a vertical plane along a horizontal contact where the effects of gravity cannot be ignored.

Ciamarra et al. (2005) used numerical simulations of horizontally flowing dry granular flows to study the interactions between the flow and its bed. The simulations demonstrate that the flows exert high shear stress on the bed, causing the contact to deform and become wavy due to the onset of shear instability growth (Figure 2.7a). The waves are similar in shape and aspect ratio to the undulose structures observed at MSH. If the interface continues to evolve under high shear, the waves grow, develop billows, and begin to resemble breaking waves (Ciamarra et al. 2005), similar in shape and aspect ratio to the recumbent flame structures at MSH. Ciamarra et al. (2005) suggested that the instabilities formed in the simulations were analogous to Kelvin-Helmholtz instabilities formed in shearing Newtonian fluids.

A series of recent laboratory experiments investigating granular flows with erodible, granular substrates produce similar structures to those in the numerical results of Ciamarra et al. (2005) (e.g. Mangeney et al. 2010; Rowley et al. 2011; Roche et al. 2013; Farin et al. 2014). Rowley et al. (2011) described shear-derived vortical features formed as colored granular charges travel over a granular substrate (Figure 2.7b). Mangeney et al. (2010) and Farin et al. (2014) observed down-flow migration of erosion waves whose amplitude and wavelength increased as slope increased (Figure 2.7c). Experiments of

Roche et al. (2013) produced sheared flame structures propagating at the interface between a fine-grained granular substrate and both initially fluidized and dry granular flows. The flows in all of these experiments contained particles with the same density as those in the bed, and the particle concentration of the flows must be lower than that of the bed because the expansion due to particle collisions (Savage, 1998) and pore fluid pressure diffusion (Druitt et al. 2007). Therefore, the bulk density of the flows is less than that of the bed during growth of the waves. The authors of these studies all attributed the recumbent flame structures to granular shear instabilities that could be akin to Kelvin-Helmholtz instabilities (Rowley et al. 2011; Roche et al. 2013; Farin et al. 2014).

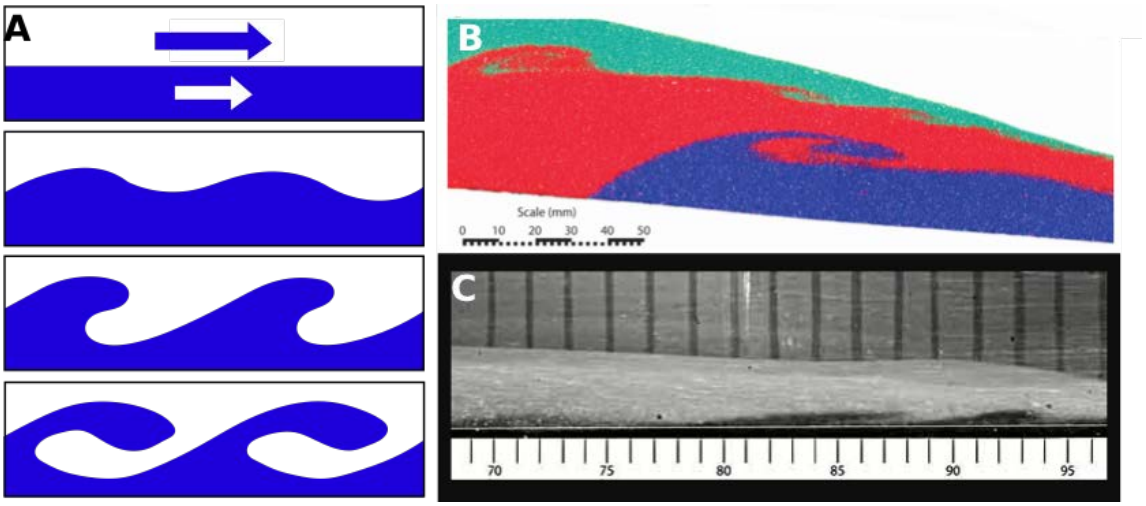

Figure 2.7 Examples from previous studies producing recumbent flame structures. (a) Sketch after Ciamarra et al. (2005) showing evolution of sheared interface during numerical simulations. (b) Shear induced mixing features adapted from Rowley et al. (2011). (c) "Erosion waves" produced in experiments of Farin et al. (2014).

In addition, laboratory experiments demonstrated that underpressure relative to the ambient environment forms just behind the sliding head of granular flows (Roche et al. 2010). Pore fluid pressures in the substrate remain equal to the ambient, which leads to an upward-directed pressure gradient from the upper surface of the bed up into the flow

(Roche et al. 2010). The upward pressure gradient is proposed to aid PDCs in the entrainment of large lithics from the bed (Roche et al. 2013, 2016; Roche 2015; Pollock et al. 2016). The numerical results of Ciamarra et al. (2005) demonstrated that such a pressure gradient would reinforce and even exacerbate the upward perturbation initially caused by the shear instability. As such, the combination of the pore fluid pressure gradient and surface instability likely both contribute to the growth of the structures observed in the experiments.

Based on the synthesized results from previous numerical and laboratory studies, we follow Rowley et al. (2011) and interpret the recumbent flame structures in the PDC deposits at MSH to be the record of granular shear instabilities formed during high shear conditions at the flow-bed interface. The majority of recumbent flame structures are located at unit contacts, suggesting that the instabilities formed during passage of the flow head. The flow head is thought to be a high shear environment (Girolami et al. 2010) and is associated with an upward directed pressure gradient (Roche et al. 2010), and thus it is perhaps not surprising that instabilities form under the flow head. However, the recumbent flame structures at MSH also exist within flow units, meters above the unit contact and deposited long after passage of the initial flow head. This observation indicates that high shear conditions also exist during intermittent periods of non-deposition from the body or perhaps during pulsating or unsteady flow behavior.

Implications for Flow Conditions

The formation of Kelvin-Helmholtz instabilities along an interface between two shearing Newtonian fluids can be predicted using an instability growth criterion (Kundu and Cohen 2004). The criterion shows that for given a density contrast between the two

fluids, instabilities will develop when the velocity difference across the interface exceeds a minimum threshold. Rowley et al. (2011) and Farin et al. (2014) adapted the instability growth criterion for granular fluids and observed that the growth criterion predicted the formation of shear instabilities in their experiments. We similarly use the instability growth criterion and measurements of the MSH recumbent flame structures to estimate the PDC velocity necessary to initiate instability growth. Because we cannot constrain the concentration of the flows during formation of the undulose structures, we use only the recumbent flame structures in these calculations. From Rowley et al. (2011), the instability growth criterion states that an interface will be unstable, leading to the growth of shear instability waves, when:

$$v_1 - v_2 \geq \sqrt{\frac{g\lambda}{2\pi}\left(\frac{\phi_2}{\phi_1} - \frac{\phi_1}{\phi_2}\right)} \qquad (Eqn.\ 2.3)$$

where v_1 and v_2 are the velocities of the flow and substrate, respectively, g is the acceleration due to gravity, and λ is the wavelength of the structure. Here, $(\phi_2/\phi_1) - (\phi_1/\phi_2)$ is the relative solid volume fraction between the flow and the substrate, where ϕ_1 is the volume fraction of particles in the flow and ϕ_2 is the volume fraction particles in the substrate (Rowley et al. 2011). We assume the velocity of the substrate is negligible at the time of instability growth, and therefore:

$$v_1 \geq \sqrt{\frac{g\lambda}{2\pi}\left(\frac{\phi_2}{\phi_1} - \frac{\phi_1}{\phi_2}\right)} \qquad (Eqn.\ 2.4)$$

To solve for the velocity at the time of instability formation, we use the length of the recumbent flame structures and some assumptions about the solid volume fraction in the flow and substrate. As discussed above, preservation of the billows without distortion

suggests a high solid volume fraction in the PDC during shear instability growth. Quantitatively constraining the solid volume fraction in PDCs from the deposits alone is impossible. However, many analogue experiments observed a basal region where solid volume fractions are only slightly expanded relative to the loose-packing solid volume fraction (Rowley et al. 2014; Breard and Lube 2017). Breard and Lube (2017) measured solid volume fractions in the dense basal regions of their experimental flows ranging from 20-60%. Gase et al. (2018) used ground penetrating radar to estimate the intergranular pore space in the PDC deposits at MSH. They found a solid volume fraction of 48-70%, which we use to constrain the solid volume fraction of the bed during deformation.

Using the literature-based estimates of 20-60% and 48-70% for the solid volume fractions of the flow and substrate, respectively, along with the range of lengths for structures recorded by us in the MSH deposits (0.08 - 17.9 m), the instability growth criterion (Eqn. 2.4) gives minimum basal slip velocities at the time of formation between 0.2-0.5 m s^{-1} for the smallest structures and 2.9-7.5 m s^{-1} for the largest structures (Table 1). Our estimates assume a static bed; however, if the forces exerted on the substrate by the flow cause the velocity of the substrate to be non-zero, the flow velocities necessary to cause instability growth would increase (cf. Equations 2.3 and 2.4). In addition, as the particle concentration of the flow approaches that of the substrate, the flow velocity necessary to cause instability growth decreases. Finally, elevated pore pressure within the fresh PDC deposits would decrease the particle concentration, farther facilitating instability growth.

Experiments producing recumbent flame structures observed that the shear instabilities form behind the head of the current (Mangeney et al. 2010; Roche et al. 2013;

Farin et al. 2014); as such, our calculated velocities for MSH likely do not reflect velocities at the flow front, but instead reflect a basal slip velocity at the time of instability formation. Farthermore, because several recumbent flame structures are found within flow units rather than the unit contacts, the velocity estimates may reflect the intermittent basal slip velocity of individual PDC pulses, or unsteadiness within a single current.

Implications for Deposition

Our observations of the recumbent flame structures suggest that in the moments prior to deposition the basal portion of the current exists in a highly concentrated state, and likely near maximum packing (see Section 5.1). The highly-concentrated basal layer must be at least as thick as the structure is tall (10s of cm to a few meters), yet the layer remains mobile enough to begin mixing with the bed. The preservation of the structures in the deposits thus suggests that the basal portion of the flow transitions from mobile to depositionally frozen relatively quickly, and the morphology of the flame structures allows us to investigate the style of deposition both qualitatively and quantitatively.

Traditionally, deposition at the base of PDCs was argued to be either *en masse* or progressive in nature (Branney and Kokelaar 2002). *En masse* deposition occurs when the entire thickness of the flow comes to rest, preserving the vertical characteristics of the flow in the resulting deposit (Sparks 1976; Wright and Walker 1981; Carey 1991). In contrast, progressive aggradation suggests that material is incrementally accumulated from the base of a PDC during sustained deposition (e.g., Fisher 1966; Branney and Kokelaar 2002; Girolami et al. 2008; Girolami et al. 2010). A more recently proposed third depositional style combines *en masse* and progressive aggradation: stepwise aggradation (Branney and Kokelaar 1992; Sulpizio and Dellino 2008). In stepwise aggradation, the deposit grows in

pulses during punctuated periods of high deposition rates separated by periods of non-deposition or erosion (e.g. Sulpizio and Dellino 2008; Charbonnier and Gertisser 2011; Sarocchi et al. 2011; Macorps et al. 2018).

The MSH recumbent flame structures suggest intermittent periods of rapid deposition, consistent with the stepwise aggradation model. As mentioned above, the preservation of the recumbent flame structures requires rapid deposition of material on the order of the height of the structure in the moments following the onset of structure growth. The velocity estimates obtained in the previous section allow us to quantitatively constrain the rates of deposition. We assume that the bed material is uplifted and then carried horizontally a certain distance until it comes to rest. The timescale for deposition is given by the estimated flow velocity and the horizontal distance the material traveled prior to deposition, given by the length of the billow. By combining the height of the recumbent flame structure with this timescale for deposition, we can estimate a rate of deposition. For example, our velocity calculations suggest that growth of the largest structure (Figure 2.3a) was initiated when flow velocities were at least 2.9 m s^{-1}, and the material traveled 17.9 m prior to deposition. From this, we estimate a maximum deposition time of 6.2 seconds. Because the structure is 2.0 m thick, the deposition rate can thus be estimated to be at least 32 cm s^{-1}. A similar approach leads to deposition rates of 4 cm s^{-1} for the smallest recumbent flame structures. These are minimum estimates, based on the lowest calculated velocities. If we instead use the highest estimated velocities, the deposition rates increase to 83 cm s^{-1} and 25 cm s^{-1} for the largest and smallest recumbent flame structures, respectively.

If the entire (8.2 m thick) deposit containing the largest recumbent flame structure accumulated at the lowest estimated deposition rate, deposition would last ~26 seconds.

Based on visual observations of the eruption, individual flows were likely emplaced over at least 10s of minutes (Criswell 1987). We therefore suggest that deposition of the MSH PDCs predominantly occurred in a stepwise fashion, with short periods (tens of seconds long) of high deposition rates followed by significant periods (minutes-long) when currents were either bypassing (i.e. non-depositional) or erosional.

The MSH deposition rates estimated here are an order of magnitude higher than those estimated for PDCs from other large eruptions. For example, Wilson and Hildreth (1997) suggest deposition rates of $\geq$0.25 cm s^{-1} for the Bishop Tuff, and Scott et al. (1996) suggest deposition rates of $\geq$1.23 cm s^{-1} for the PDCs generated during the June 15, 1991 eruption of Mount Pinatubo. However, the deposition rates for the Bishop Tuff and Mount Pinatubo are averaged over the entire thickness of the deposit assuming steady, progressive aggradation. Using structures similar to those observed in the MSH deposits can allow for farther constraint of deposition rates by identifying sections of the deposits rapidly laid down during the longer flow event.

Conclusions

The deposits of the high-concentration, column-collapse derived PDCs produced during the May 18, 1980 eruption of MSH record evidence for syn-depositional basal shear exerted by the PDCs on the substrate. High shear on the flow-bed interface results in the growth of granular shear instabilities that manifest themselves as recumbent flame structures preserved in the deposits. Similar granular shear instabilities occur in both numerical and experimental investigations and are regarded as being akin to Kelvin-Helmholtz instabilities. We use the dimensions of the recumbent flame structures and a modified instability growth criterion to calculate the minimum basal slip velocities at the

time of instability initiation. Our velocity estimates range from 0.2-7.5 m s^{-1} for the MSH PDCs. The preservation of the recumbent flame structure suggests that the basal region of PDCs exists in a highly concentrated, but still mobile, state until the material in the basal flow region is rapidly deposited. Using the velocity estimates and the dimensions of the structures, we estimate minimum deposition rates between 4 and 32 cm s^{-1}. Given that most PDC outcrops at MSH are on the order of 10-20 m thick, the entire thickness of an outcrop would have accumulated in a few minutes if these deposition rates were sustained. However visual observations show that individual flows were emplaced over tens of minutes. We therefore suggest the PDCs deposited in a stepwise fashion with periods of punctuated high rates of deposition in between extended periods of non-deposition or erosion.

In addition, we suggest that undulose and recumbent flame structures may often grow during deposition of a PDC and are either subsequently mixed into the current and destroyed, or not visible due to lack of contrasting textures. These structures, and the processes that form them, may be more common in the basal portion of concentrated PDCs than previously thought.

One of the greatest challenges in volcanology is constraining PDC flow, transport, and depositional conditions from a given deposit. Numerical simulations and scaled, granular flow experiments can help establish relationships between depositional features and conditions within the PDC (e.g. Clarke and Voight 2000; Taddeucci and Palladino 2002; Roche et al. 2013). While continued experimental work is necessary to fully validate the use of the instability growth criterion for fluidized PDCs, our field-based approach

shows promise for extracting quantitative information about flow conditions from PDC deposits.

Acknowledgements

This work was funded by a grant from the National Science Foundation (Award Number: 1347385). The authors thank Dr. Eric Breard, one anonymous reviewer, the associate editor, Dr. Richard Brown, and the executive editor, Dr. Andrew Harris, for their thoughtful and constructive comments that improved the quality of this manuscript.

Table 2-1 Measurements of syn-depositional sedimentary structures found in the PDC deposits at MSH.

Outcrop	Distance from vent (km)	Recumbent Flame (RF) or Undulose	Flow Unit	At Unit contact or within Unit	Figure Number	Length (m)	Height (m)	Velocity range (m/s)	Deposition Rate (cm/s)
B-2a	5.0	RF	III	Within unit	3b	3.3	0.4	1.2-3.2	15
B-2a	5.0	RF	III	Within unit	3b	2.5	0.5	1.0-2.8	20
B-2a	5.0	RF	III	Within unit	3b	0.5	0.09	0.5-1.2	9
B-2a	5.0	RF	III	Within unit	3b	0.5	0.1	0.5-1.2	10
B-2a	5.0	RF	III	Within unit	3b	3.4	0.6	1.3-3.3	23
C-3	5.1	RF	III	Within unit	1c	17.9	2.0	2.9-7.5	32
C-4	5.2	Undulose	IV	Within unit	1a	35.7	4.1	N/A	N/A
C-4	5.2	Undulose	IV	Within unit	1a	27.3	2.9	N/A	N/A
B-3	5.4	RF	III	At contact	3a	0.4	0.04	0.4-1.1	4
B-3	5.4	RF	III	At contact	3a	0.08	0.04	0.2-0.5	10
AD-2a	5.7	Undulose	II	At contact	4a	4.8	0.41	N/A	N/A
AD-2a	5.7	Undulose	II	At contact	4a	4.6	0.35	N/A	N/A
AD-2a	5.7	Undulose	II	At contact	4a	4	0.25	N/A	N/A
AD-3	5.9	RF	III	Within unit	3c	3.4	0.5	1.3-3.3	19
AD-3	5.9	RF	III	Within unit	3c	6	0.4	1.7-4.3	11
AD-3	6.1	RF	IV	Within unit	3d	3.5	0.6	1.3-3.3	22
AD-3	6.1	Undulose	II	At contact	4c	6.1	0.67	N/A	N/A
AD-3.5	6.5	Undulose	III	At contact	4b	5.7	1.0	N/A	N/A
AD-3.5	6.5	Undulose	III	At contact	4b	4.7	1.0	N/A	N/A
AD-3.5	6.5	Undulose	III	At contact	4b	4.8	0.9	N/A	N/A
AD-3.5	6.5	Undulose	III	At contact	4b	5	0.9	N/A	N/A
AD-3.5	6.5	Undulose	III	At contact	4b	8.7	1.1	N/A	N/A

CHAPTER THREE: THE EFFECTS OF AN ERODIBLE BED ON THE BEHAVIOR OF GAS-PARTICLE FLOWS – IMPLICATIONS FOR PYROCLASTIC CURRENTS AND SNOW AVALANCHES

Abstract

Gas-particle flows are a common, and often dangerous, phenomenon occurring at the Earth's surface that include pyroclastic currents and snow avalanches. The behavior of these flows is complex and controlled by processes occurring both internally and at the flow margins, where flows interact with their external environment. Here we present the results of experiments investigating how fluidized and non-fluidized gas-particle flows interact with an erodible, granular bed at various slope angles. These experiments examine the effect of basal processes, including material entrainment and pore fluid pressure diffusion, on flow runout distance. As in previous studies, we observe significant basal entrainment of bed material just behind the flow front; the combination of shear in the bed and underpressure in the head contribute to an upward directed pressure gradient that promotes the rapid mixing of bed material into the flow. However, unlike previous studies, we do not observe an increase in runout distance for flows travelling over erodible beds. We believe the key difference between our study and previous studies is the thickness of our erodible bed. Elevated pore fluid pressures occur within the flow body due to particle settling and drag, and potentially in uppermost part of the erodible bed due to shearing. When the bed is porous but thin, the pore fluid pressure can only diffuse upwards through the overlying flow, extending its runout. In contrast, when the bed is sufficiently thick, as

in our experiments, the pore fluid pressure diffuses both up through the flow and down into the bed, effectively decreasing the runout distance relative to flows on thin beds. The results of our experiments, synthesized with those of previous studies, demonstrates that the characteristics of the bed can dramatically affect the runout distance of gas particle flows, both positively and negatively. The bed thickness, permeability, yield strength, and the state of pore fluid pressure must all be considered when either interpreting or predicting the runout of gas-particle flows. The results of our study have implications for the hazard potential of natural pyroclastic currents and snow avalanches that may travel over a variety of bed types, each with their own characteristics that enhance or inhibit the runout distance.

Introduction

Fluid-particle flows occur in a variety of settings across the surface of the Earth and play an integral role in sediment transport and landscape evolution (Delannay et al., 2015). Examples of fluid-particle flows in nature include debris flows, landslides, snow avalanches, and pyroclastic currents, all of which pose hazards to populations or infrastructure located along their potential flow paths. Providing accurate hazard assessments for these flows is essential, and at the center of that problem lies understanding both the internal and external processes that control the flow behavior.

Processes occurring within these gravity-driven flows include both particle-particle collisions and particle-fluid interactions. These small-scale internal processes dissipate flow energy as friction due to collisions and fluid drag and play a significant role in controlling the overall behavior of these flows (Dufek, 2016). The relative importance of particle-particle and particle-fluid interactions changes as a function of the particle concentration. As particle concentration increases, particle-particle collisions become more

frequent, and thus begin to dominate the overall behavior. Particle concentrations in gravity-driven flows can range from fractions of a percent up to maximum packing, which gives rise to a wide range of flow behavior (Delannay et al., 2015; Dufek, 2016).

In addition to understanding the small-scale internal processes, we must also understand the external interactions that occur between gas-particle flows and their environment during transport. External interactions include mixing with the ambient environmental fluid (typically air or water) and entrainment of the bed material over which the flows travel. Recent studies demonstrate that mixing with the ambient fluid affects the behavior of both dilute pyroclastic currents and subaqueous turbidity currents (e.g. Felix and Peakall, 2006; Andrews and Manga, 2012; Andrews, 2014, Benage et al. 2016). While these studies demonstrate that runout distance is affected by interactions with the environment at the top, sides, and front of the flows, both field and experimental studies suggest that similarly complex interactions occur at the base of fluid-particle flows as well (e.g. Mangeney et al., 2010; Iverson et al., 2011; Chédeville and Roche, 2014; Farin et al, 2014; Pollock et al., 2019). Here we present the results of analogue laboratory experiments that farther investigate the processes that occur at the flow-bed interface of gas-particle flows, and we seek to understand how those processes affect the overall flow behavior.

Controls on the behavior of fluid-particle flows

The behavior of fluid-particle flows is affected by the complex interplay of many parameters including properties of the solid particles (e.g. density, grain size, friction angle), properties of the interstitial fluid (e.g. density, viscosity), and the properties of the mixture (e.g. solid volume fraction, permeability, hydraulic conductivity; e.g. Savage, 1984; Iverson, 1997; GDR MiDi., 2004). Here we focus our brief review on the effects of

the parameters most relevant to our experiments on gas-particle flows: pore fluid pressure and interaction with an erodible bed.

Effects of pore fluid pressure

Elevated internal pore fluid pressures significantly affect the behavior of both gas-particle and water-particle flows (e.g. Iverson, 1997; Major and Iverson, 1999; McElwaine and Turnbull, 2005; McArdell et al. 2007; Roche et al. 2010; Roche 2012). Pore fluid pressure decreases the interactions between particles, thereby decreasing the loss of flow energy to friction and collisions between particles and ultimately increasing the flow runout distance (Roche et al. 2010; Roche 2012). For fine-grained gas-particle flows, elevated pore fluid pressures result in the overall flow kinematics being more consistent with flows of inertial fluids than those of dry granular flows (Roche, 2012).

The overall behavior of experimental fluidized granular flows, as identified from experiments, is divided into three phases that relate to the diffusion of pore fluid pressure (e.g. Roche et al., 2008). The flows first accelerate due to the collapse of the column and initial movement of material into the channel. The second phase is characterized by a constant flow velocity and is related to the rate of pore pressure diffusion (Roche et al. 2008; 2010). The transition between the second and third phases occurs when pore fluid pressures decreased to the point that flows enter a dry granular flow regime, which leads to flow deceleration and stopping.

Mechanisms of pore fluid pressure generation

Numerical simulations suggest that elevated pore fluid pressure can be generated due to decreased porosity during compaction if the boundary does not allow gas to simply escape from the granular mixture (Goren et al., 2010). Experiments measure elevated pore

fluid pressures generated during compaction and collapse of columns and due to sedimentation and particles settling in the body of flows (Roche, 2012), both scenarios apparently confirming that decreasing pore volume leads to increases in pore fluid pressures. Additionally, when flows travel over a rough bed their runout can more than double relative to flows travelling over a smooth bed, which is attributed to autofluidization of the flow (Chédeville and Roche, 2014; Chédeville and Roche, 2015). Autofluidization occurs when flow particles fall into the interstices between bed particles and eject interstitial air up into the overriding flow. The addition of air to the flow increases the pore fluid pressure, reduces the effects of particle-particle collisions, and allows for increased runout distances (Chédeville and Roche, 2014; Chédeville and Roche, 2015). These studies show that the efficiency of this process increases non-linearly as the size of particle in the non-erodible bed increases.

Effects of an erodible bed

The work of Iverson et al. (2011) demonstrates that interaction of debris flows with an erodible bed can lead to either increases or decreases in flow momentum depending on the properties of the bed. The authors argue that when a flow entrains wet sediment, pore fluid pressures increase, which leads to increased flow velocity and momentum. Conversely, when dry sediment is eroded, flow momentum and runout distance decrease. For gas-particle flows, Mangeney et al. (2010) and Farin et al. (2014) observe that the runout distance of dry granular flows can increase by up to 50% when the flows travel overtop a thin, erodible bed. These two studies observe that as the bed angle approaches the angle of repose for the material, the intensity of erosion increases, and the flow velocities and runout distance increase as well. Farin et al. (2014) point out that the

increase in runout distance cannot be completely explained by an increase in flow mass via entrainment. Instead, they suggest that basal entrainment supports the development of an extended slow propagation phase, which leads to increased runout distances. However, the ultimate cause of the increased duration of the slow propagation phase remains unclear.

Roche et al. (2013) observe different efficiencies and styles of particle entrainment depending on the relative sizes of particles in the flow and bed. The study of Roche et al. (2013) investigates the flow velocities necessary to uplift particles of a given size, but did not investigate how the entrainment of the uplifted particles affects subsequent flow behavior. Therefore, despite evidence suggesting erosion of bed particles increases flow runout distance in dry granular flows, questions remain regarding whether the relative sizes of particles in the flow and bed affect this process. Additionally, the effect of fluidization (both initial fluidization and autofluidization) on erosion efficiency and subsequent flow behavior, specifically for thick erodible beds, remains relatively unexplored.

The studies discussed above demonstrate that the characteristics of the bed affect the runout distance of flows via both autofluidization and erosion, but the interplay between these two processes is complex. In this study, we seek to disentangle the effects of erosion and autofluidization on flow runout distance. Our experiments systematically vary the slope, size of particles in the bed, and level of fluidization (dry vs. fluidized) to assess the relative effects of autofluidization and erosion on flow runout distance. Specifically, we address the following research questions:

1. How do the characteristics of the bed (erodibility, grain size, slope) affect the behavior of granular flows?
2. Is there evidence for autofluidization of the flows even when the bed is erodible?

3. Does the presence of an erodible bed affect fluidized granular flows in the same way as dry granular flows?
4. How does the thickness of the erodible bed affect the process of pore pressure diffusion and thus the runout distance of granular flows?
5. What is the effect of slope on current unsteadiness?

Methods

Experimental Set-Up

Our experiments use a similar apparatus to that of earlier dam break experiments by Roche et al. (2010) and Chédeville and Roche (2014; 2015) and fulfill scaling requirements to dense pyroclastic currents as presented in Roche (2012). The apparatus consists of a 20 x 10 cm particle reservoir connected to a channel that is 3 meters long and 10 cm wide with a rectangular cross section (Figure 3.1). A sliding sluice gate separates the reservoir from the channel. The gate opens by the release of a counterweight that lifts the gate rapidly enough that the gate motion does not affect the flow of particles. The channel can incline to slopes up to 20° from horizontal. The walls of the device are clear plexiglass to allow for observation and measurement with high speed video camera.

Prior to each experiment, we fill the reservoir to a height of 30 cm with sub-spherical glass beads averaging 80 μm in diameter and a density of 2500 kg/m^3. The apparatus attaches to a system that supplies compressed gas to the base of the reservoir via a series of manometers and dryers to control air flux and moisture content, respectively. The gas travels through a porous plate at the base of the reservoir both to dry the particles (for a minimum of 10 minutes prior to each experiment) and, for experiments on fluidized flows, to generate pore fluid pressure in the granular mixture before opening the gate.

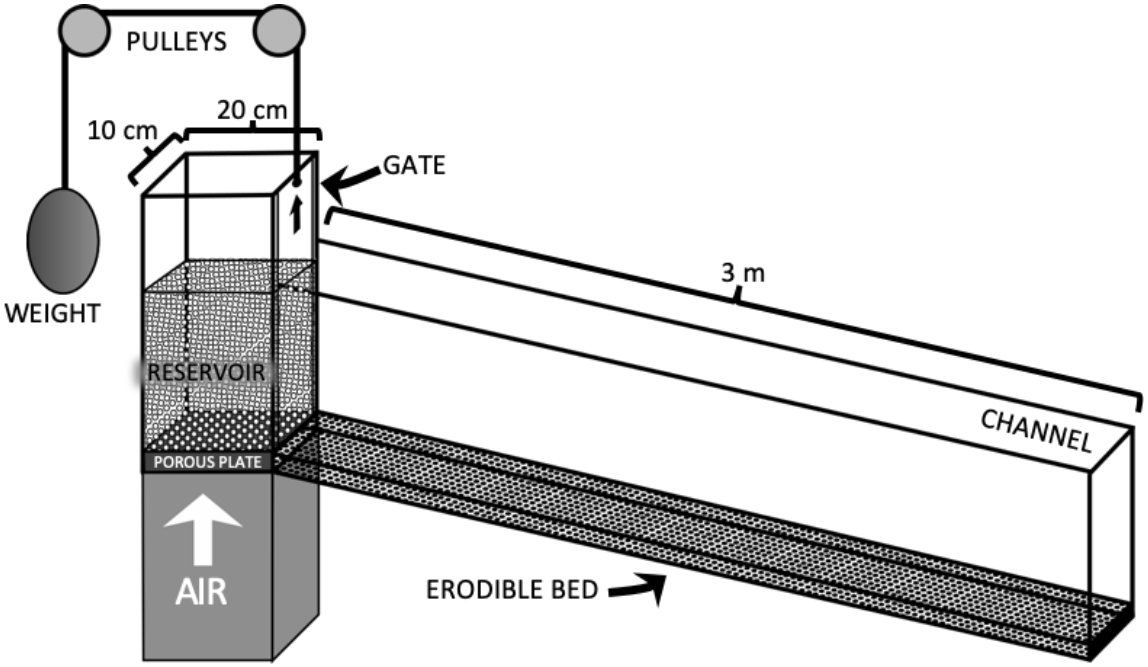

Figure 3.1 Schematic of experimental device. The channel is 3 m long and 10 cm wide and is attached to a reservoir, which is 10 cm wide and 20 cm long. Prior to each experiment the channel base is inclined to the desired slope angle (up to 15 degrees) and covered with 4 cm of erodible particles. Additionally, the reservoir, which is filled with particles, can be supplied with air via a series of manometers and dryers to effectively fluidize the granular mixture in the reservoir prior to opening the gate and initiating the experiment.

For fluidized experiments, the air flow velocity is 13 mm/s, which is above the minimum fluidization velocity, U_{mf}, (Roche, 2012) and allows for slight expansion of the granular mixture (~3-5%). No gas is supplied to the base of the channel so that after the gate opens and flows propagate into the channel, the flows defluidize progressively via pore pressure diffusion. Due to the low permeability of the granular material ($k \sim 10^{-11}$ m^2), the timescale for pore pressure diffusion is slow relative to advection of the granular mixture into the channel. The difference in timescales results in elevated pore fluid pressures in the flows as they propagate into the channel. The flows then progressively defluidize until the flows reach the purely dry granular regime and final deposition occurs (Roche et al., 2010; Roche, 2012).

In addition, a bed of mobile particles covers the base of the channel prior to each experiment. Prior to the experiment, the channel base is covered with a single layer of 3 mm particles that are glued to the bed to add roughness. The mobile, erodible bed consists of sub-spherical colored particles with average diameters of 40, 80, 375, 500, 700 μm and densities of 2500 kg/m^3. The colored particles allow for easy observation of erosion and mixing processes between the flow and substrate. The beads are poured into the channel, and then we produce a level, but not compacted, surface by dragging a board across the surface. This process ensures an even bed thickness of 4 cm for all experiments. We chose a thickness of 4 cm because in tests we observed no movement of particles at the contact between the bed and the base of the channel; the lack of particle movement suggests all forces exerted on the bed by the flow are absorbed within the bed itself rather than being transmitted to the channel base.

High-speed video and image processing

A high-speed video camera records each experiment at 1000 frames/sec. We used automated image analysis techniques to measure flow front kinematics. First, the entire sequence of images for an experiment is read into MATLAB before being down sampled to 200 frames/sec. Starting at the beginning of the experiment, we analyze each successive pair of images together. We crop and filter the images to enhance contrast and brightness. Then one image is subtracted from the other to show where differences exist between the image pair. In our experiments, the difference exists due to the flow propagating between images. Size and contrast thresholds are applied to the differenced image to highlight the position of the flow front in the second image. We record the position of the flow front for that set of image pairs along with a time signature. This process repeats for every image

pair in the entire sequence allowing us to produce a position vs. time dataset for each experiment from which we calculate flow velocities.

We validated our automated image analysis technique by manually measuring the flow front position for a subset of 15 experiments and comparing the results. The position vs. time data from the two approaches differs by less than 3%.

Results

Effect of slope and bed grain size on runout distance

The initial column height, H, controls the overall kinematics of granular flows (Roche et al. 2008). Therefore, the column height is the fundamental length scale parameter to which we scale the runout distance (Roche et al. 2008). We report the runout distances of our experimental flows as the normalized flow runout distance (r/H) to allow for easier comparison with other studies.

In our experiments, the runout distance increases with increasing slope (Figure 3.2). We find that a fluidized flow travels farther than a non-fluidized flow of the same initial conditions. Fluidized flows travel between 48% and 118% farther than their non-fluidized counterparts, with an average increase in runout distance of 78% (Figure 3.3). The effect of increased runout distances in initially fluidized flows decreases only slightly at higher slope angles with an average increase of 84% on horizontal slopes versus a 60% increase on 15 degree slopes (Figure 3.3).

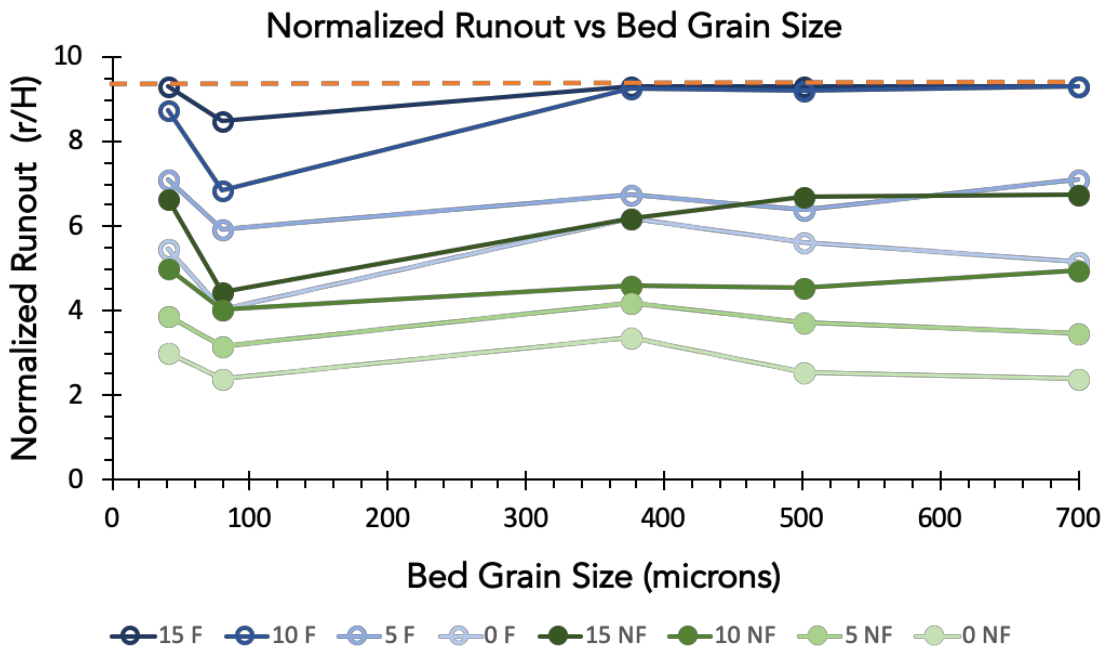

Figure 3.2 Runout distance is relatively unaffected by the size of particles in the bed except when the particles in the bed are 80 microns when the runout distance decreases. Blue and green colors represent fluidized and non-fluidized flows, respectively, and progressively darker color indicates increasing slope. Dashed orange horizontal line indicates the end of the channel.

Comparing the runout distance of fluidized flows to dry flows reveals no trends with either increasing bed grain size or increasing slope angle; fluidized flows travel between ~50% and 120% farther than dry flows regardless of slope or bed grain size. A slight decrease in the runout distance of fluidized flows (relative to dry flows) may occur for flows travelling at the highest slope angle (15 degrees), although the decrease is not substantial. These observations contrast with results of previous experiments that investigate how bed properties affect flow behavior. For example, Chédeville and Roche (2014) observe that the runout distance of fluidized flows relative to dry flows increases with increasing bed grain size. This effect continues up to 1.5 mm and then decreases up to the largest grain sizes used in their experiments, 6mm.

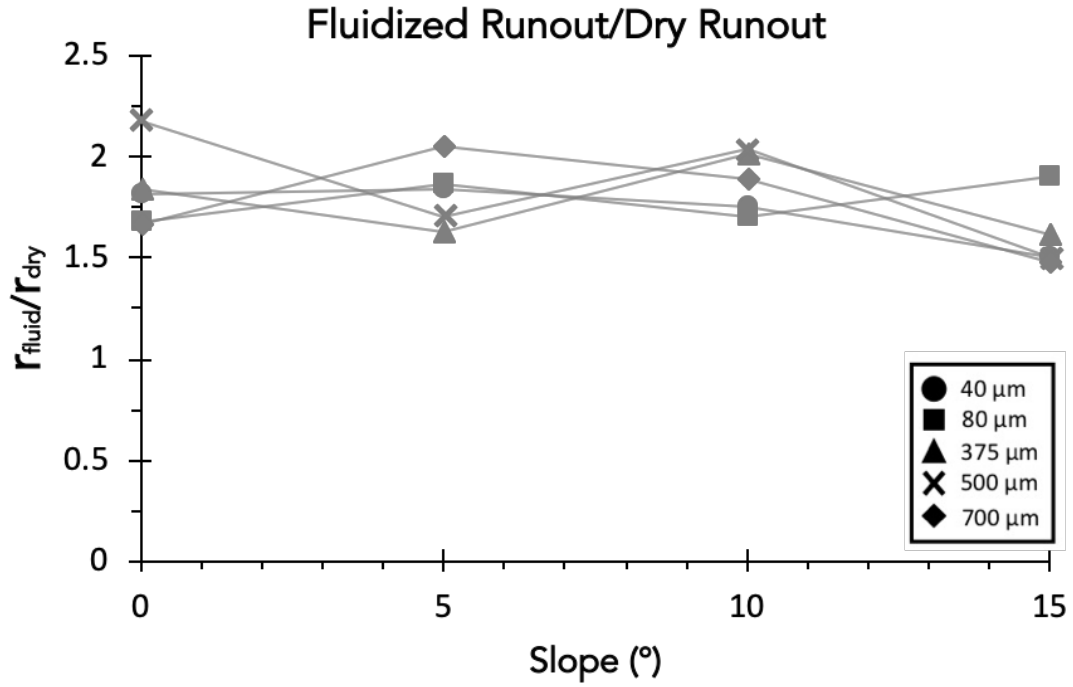

Figure 3.3 Runout distance of fluidized flows relative to runout distance of non-fluidized flows. In general, the difference between the runout distance of fluidized flows and non-fluidized flows remains constant as slope increases. Fluidized flows travel between 50% and 120% farther than non-fluidized flows.

Additionally, Chédeville and Roche (2015) observe that the runout distance of fluidized flows is more significantly affected by the presence of a rough, fixed bed at higher slope angles than the runout of dry flows (see Figure 5b in Chédeville and Roche, 2015). When considering our experiments in the context of the results of previous studies, the lack of trends in relative runout distances between fluidized and dry flows is perplexing (Figure 3.3). This observation suggests that some process limits the effects of the autofluidization described by Chédeville and Roche (2014; 2015), which we will revisit in the discussion below.

For experiments conducted at a given slope angle, as the bed grain size changes, relatively little variation in flow runout distance exists (relatively straight lines across

Figure 3.2); the runout distance is more significantly controlled by level of fluidization (blue vs green; Figure 3.2) and slope (shading; Figure 3.2). However, the flow runout distance decreases when the bed grain size is 80 μm, which is also the size of particles in the flow. Compared to the averages for the other 4 bed grain sizes, flows that travel over a bed of 80 μm particles travel 13 to 30% shorter distances.

Flow front kinematics

In Figures 3.4a – 3.4j, the normalized flow front position in the channel, r/H, is shown as a function of the normalized time, t/t_0 where $t_0 = (H/g)^{1/2}$ (Lajeunesse et al. 2004; Roche et al. 2008). Similar to previous experiments (e.g. Roche et al. 2008), flows propagate in three distinct phases indicated by slope changes in the position versus time plots (Figure 3.4a – 3.4j). The first phase is the primary acceleration phase, during the second phase the flows propagate at relatively constant velocity, and the final phase is the deceleration and stopping of the flow.

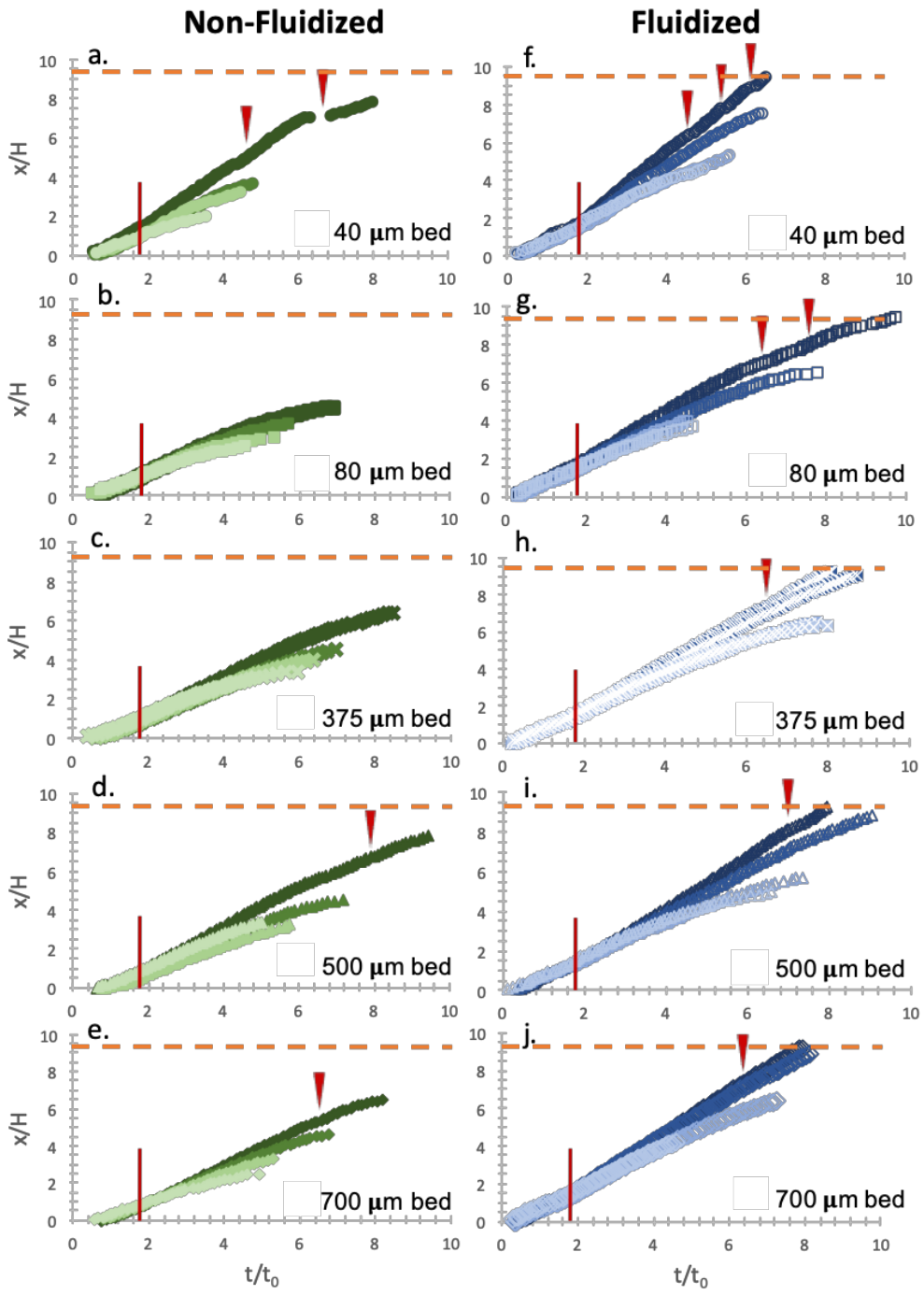

Figure 3.4 (a) – (j) Plots of normalized position (x/H) versus normalized time (t/t0 where $t_0 = (H/g)^{½}$) for both non-fluidized (green) and fluidized (blue) flows travelling over erodible beds of different grain sizes. Darker colors indicate higher slopes, from 0 to 15 degrees. The vertical red bar indicates the transition from first phase of acceleration to the second, constant velocity phase. Red arrows indicate pulsating behavior at the flow front. Horizontal orange line indicates the end of the channel.

The primary acceleration phase relates to the collapse of the granular material once the gate is opened and the flow begins to propagate out into the main channel (Roche et al., 2008; Roche, 2012). The transition from the initial acceleration phase to the constant velocity phase occurs at a similar normalized time (t/t0) for all experiments (indicated by slope change and vertical red line at $t/t_0 \approx 1.8$ in Figures 3.4a-3.4j). In contrast, the onset of the deceleration phase is strongly controlled by the degree of fluidization and slope of the bed, but appears to be independent of the size of bed particles. The deceleration phase begins later for fluidized flows relative to non-fluidized flows of the same initial configuration (slope and bed grain size). The deceleration phase also begins later for flows at higher slopes compared to those on shallower slopes. In some cases, where the flow exits the channel, the flow never enters the deceleration phase.

Pulsating Behavior

Pulsating behavior at the flow front occurs in both fluidized and non-fluidized flows but is most prominent at high slope angles (above 10 degrees) and in fluidized flows. Slight slope inflections or occasionally complete breaks in the position versus time plots in Figure 3.4a – 3.4j suggest pulsation of the flow front, with individual pulses marked with red arrows. As the shape of the curves suggests, the flow front begins to decelerate prior to being overtaken by a more rapidly moving pulse that then becomes the new flow front. The flow then propagates at a relatively constant velocity until that flow front begins to decelerate before either completely stopping or being overtaken by another pulse.

The maximum number of pulses recorded in any experiments occurred for the fluidized flow propagating on a 15 degree slope over a bed of 40 μm particles. In this experiment, three distinct flow pulses were recorded (Figure 3.4f). Similarly, the maximum

number of pulses (2) observed in a non-fluidized flow was the flow travelling on a 15 degree slope over a bed of 40 μm particles (Figure 3.4a). We calculate a Froude number for each experiment using the average flow velocity and flow thickness using:

$$Fr = \frac{U}{\sqrt{gh}} \qquad (Eqn.\ 3.1)$$

Where U is the average velocity, g is gravity, and h is the flow height. These calculations demonstrate a clear correlation between pulsating behavior and increased Froude number (Figure 3.5). As Froude number increases, the flow is increasingly likely to exhibit pulsating behavior at the flow front.

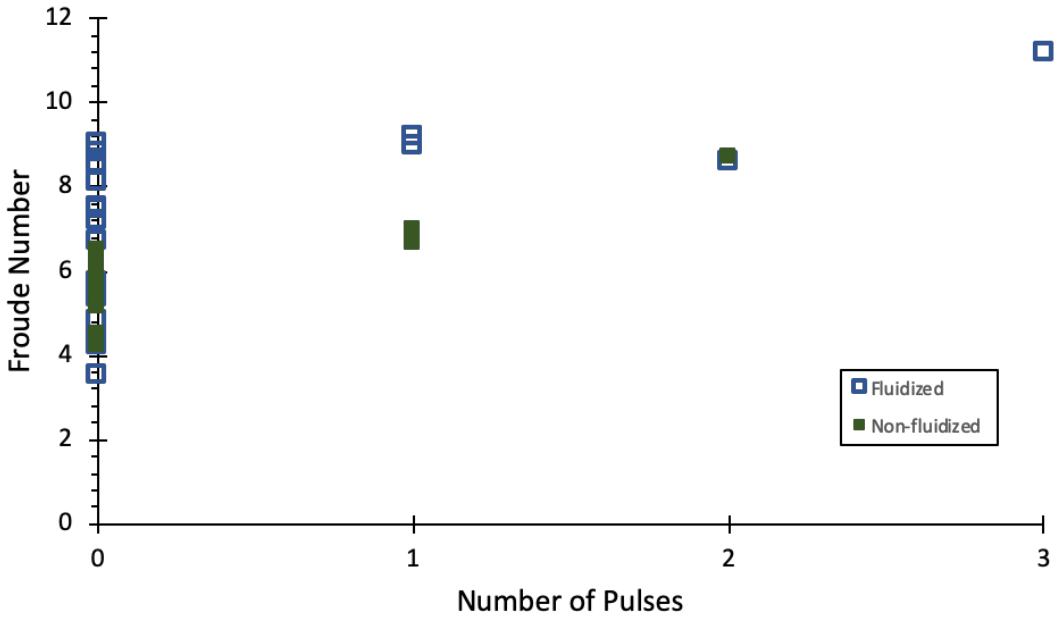

Figure 3.5 Calculated Froude numbers for each flow plotted against the number of pulses observed in the experiments. While the range in Froude numbers for flows without pulses is wide (3.5 – 9.0), any flow for which pulsating occurred has Froude numbers above 6.6 and are some of the highest Froude numbers observed for any flows.

Flow-Bed Interactions

In both fluidized and non-fluidized experiments and at all bed slope angles, erosional mixing and basal entrainment occurs between the flow and the bed (see Chapter 4 for full discussion of mixing structures). As the flow moves over the bed, the flow-bed interface first becomes wavy before material begins to uplift into the flow a few cm behind the flow head (Figure 3.6). The uplifted bed material travels with the flow a given distance before either being frozen and preserved in the deposit or being completely amalgamated into the flow. When preserved, the mixing manifests itself in the deposits as recumbent flame structures; bed material protrudes up into the overlying flow deposit before bending, becoming subparallel with the bed, and thinning in the downstream direction of flow. At low slope angles, the deposited structures retain a wave-like shape to them, but at higher slopes, the structures are significantly stretched and elongated until they appear almost as a thin layer of bed material in the flow deposit. When preserved, the recumbent flame structures vary in length from sub-cm on horizontal slopes to over 10 cm on 10 and 15-degree slopes. Their height similarly varies from just a few mm up to 3-4 cm.

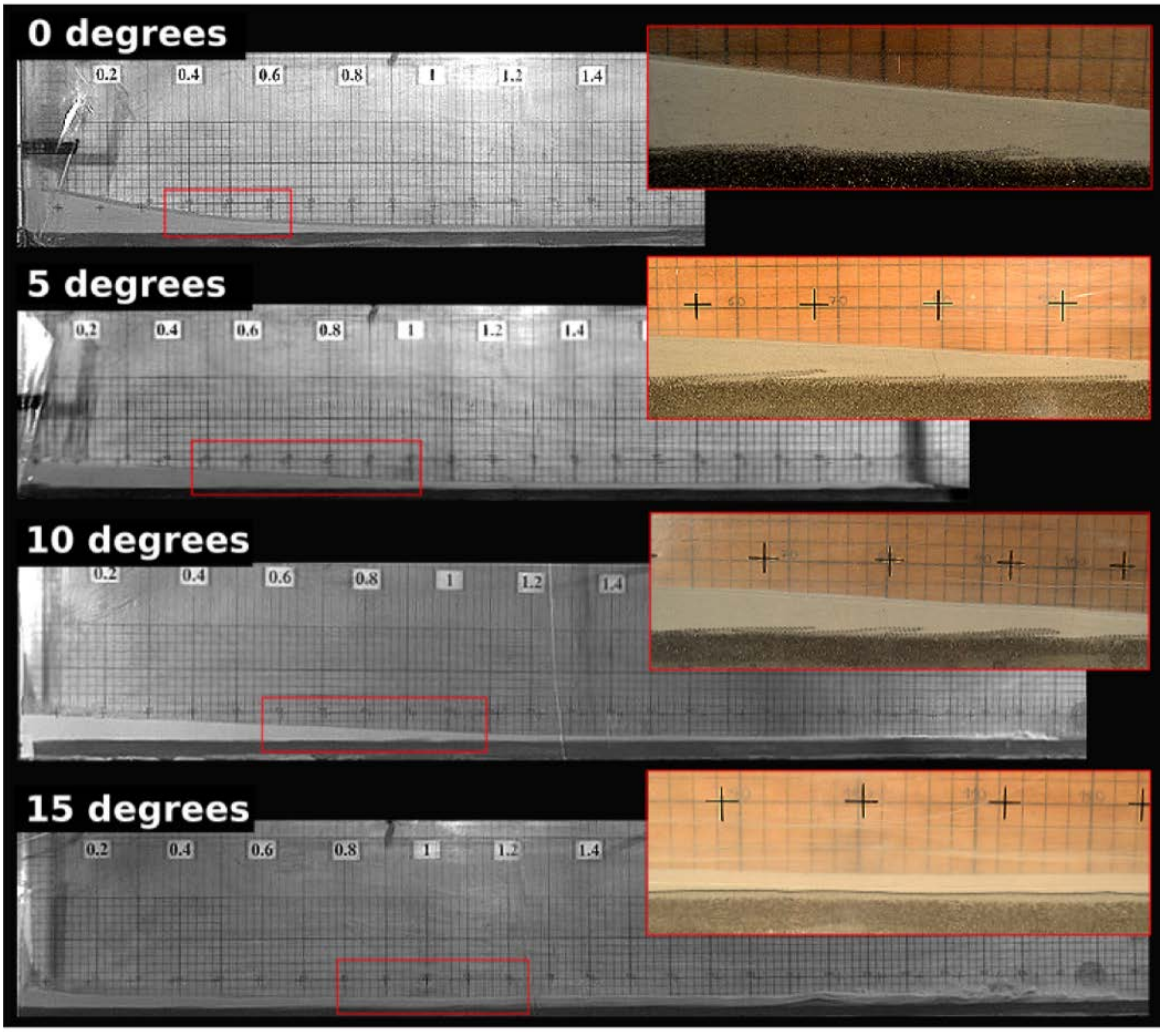

Figure 3.6 Examples of fluidized flows travelling on 0, 5, 10, and 15 degree slopes with insets showing detail of mixing and basal entrainment structures.

Discussion

Effects of bed characteristics on flow behavior

The results of our experiments agree with those of previous studies regarding the effect of slope and the effect of fluidization on the runout distance of granular flows. Similar to the results of Farin et al. (2014) on dry granular flows and Chédeville and Roche (2015) on initially fluidized flows, our experiments show that runout distance increases as the slope of the bed increases. Also, similar to studies by Roche et al. (2008), the initially

fluidized granular flows travel farther than dry flows in all configurations. However, Roche et al. (2008) observe that flows fluidized at U_{mf} travel 120% to 140% farther than non-fluidized flows of similar initial configuration, which is a much larger increase than the 48% to 118% increase observed in our experiments (average of 78%). Because the experiments of Roche et al. (2008) used a smooth, non-erodible bed, a few differences in our experimental configuration may account for the minimized effect of fluidization we observed: bed roughness, bed thickness, bed erodibility, and flow/substrate friction coefficient. We discuss below the implications for each of these parameters and their potential effect on flow runout distance to disentangle the combined effects.

Autofluidization as a means of increasing runout distance?

Previous studies investigate the effect of bed roughness on flow runout distance and observe that as the size of particles fixed to the bed (i.e. non-erodible) increases, the runout distance of the flows increases (Chédeville and Roche, 2014). This effect continues up to a bed roughness of 3 mm; non-erodible beds with >3 mm beads act as obstacles, thus causing a decrease in flow runout (Chédeville and Roche, 2014). Supported by measurements of pore fluid pressure, the authors attribute the increased runout distance to autofluidization of the flow; when particles fall into the interstices between bed particles, the interstitial air is expelled upwards into the overriding flow. The expelled air allows the flow to remain fluidized longer, thus increasing the distance that flow can travel.

In our experiments, the runout distance remains nearly constant as flows travel over erodible beds of progressively larger grains from 40 μm up to 700 μm (Figure 3.2). The exception is the decreased runout distance observed when flows travel overtop a bed of 80 μm particles (the same diameter as flow particles). The lack of an increase in runout

distance when the bed contains progressively larger particles either suggests that autofluidization, as observed in previous experiments, does not have the same effect when the bed is erodible, or that autofluidization does not occur.

Additionally, in comparing our experiments on a horizontal slope to those of Chédeville and Roche (2014), we observe that the runout distance for dry flows in both studies are within error (Figure 3.7). However, fluidized flows traveling overtop an erodible bed (this study) do not travel as far as fluidized flows traveling overtop a non-erodible bed (Chédeville and Roche, 2014) comprised of the same size particles (Figure 3.7). This observations again suggests that autofluidization is not as effective when the bed is erodible, that some other process negates the effect of autofluidization, or both.

To farther examine whether autofluidization occurs in our flows, we compare our results to the work of Chédeville and Roche (2015) who studied how slope affects the autofluidization process. Their study investigated how travelling over a fixed (i.e. non-erodible) bed of 3 mm particles inclined up to 30 degrees affected flow behavior relative to travelling over a smooth, non-erodible bed. They measured high pore fluid pressures at all slope angles and observed that the runout distance increased due to autofluidization at slopes up to 12 degrees.

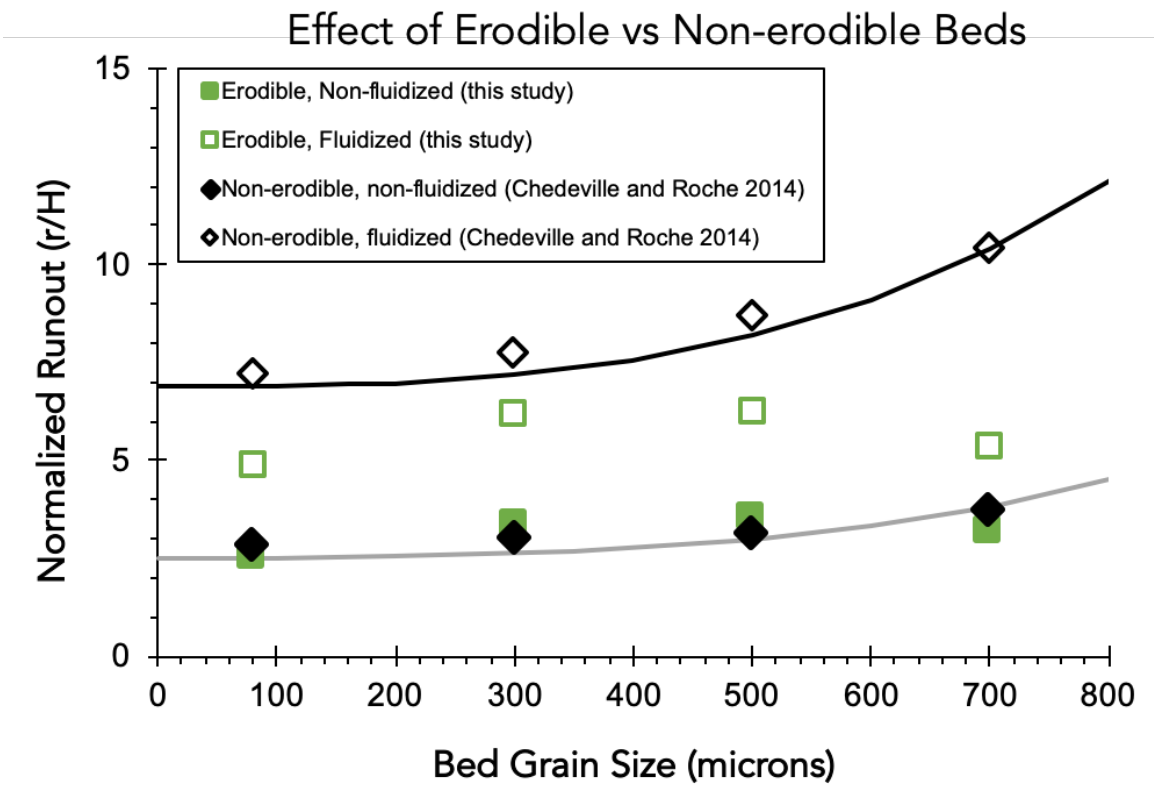

Figure 3.7 Comparison of runout distance of our flows on horizontal, erodible beds (green squares) to those of Chédeville and Roche (2014) on horizontal, non-erodible beds with particles glued to the channel base (black diamonds). Runout distances for non-fluidized flows are similar regardless of whether particles are fixed to the bed or erodible (open symbols). In contrast, fluidized flows travelling over an erodible bed do not travel as far as fluidized flows travelling over non-erodible beds (closed symbols).

When we compare our runout distances for flows travelling over an erodible bed to those of Chédeville and Roche (2015) that travelled over a rough, fixed bed, we observe that our flows travel significantly shorter runout distances (Figure 3.8a and 3.8b). Our dry flows over erodible beds travelled 5-25% farther than dry flows travelling over a smooth bed (Figure 3.8a). This observation suggests that some autofluidization may occur that causes the flows to travel farther over an erodible bed than when the flow is smooth. However, when we compare the runout distances for fluidized flows in both studies, we see that our flows travel 20-50% shorter distances than flows travelling overtop of a smooth

bed in the experiments of Chédeville and Roche (2015) (Figure 3.8b). The decreased runout distance relative to flows travelling over a smooth bed indicates that if autofluidization is occurring in our experiments, its effect must be diminished by some other process(es), or autofluidization does not occur in the case of an erodible bed.

Because our experiments do not measure the pore fluid pressure within the flow, we cannot definitely determine whether autofluidization occurs in our flows. However, if autofluidization does occur, the decreased runout distance of our flows relative to those of Chédeville and Roche (2014; 2015) suggests other processes limit how far the flows can travel.

Bed thickness and pore pressure diffusion

For decades, elevated internal pore fluid pressures in the body of gas-particle flows have been invoked to explain the long runout distances of certain geophysical flows including pyroclastic currents and snow avalanches (e.g. McElwaine and Turnbull, 2005; McArdell et al., 2007). A variety of mechanisms possibly explain the origin of the elevated pore fluid pressures including gas supplied by external (e.g. burning vegetation or vaporizing surface water; Wilson 1980) or internal sources (e.g. degassing pyroclasts; Wilson 1980), differential gas-particle motion causing upward expelling of gas (Goren et al., 2010), or air lubrication via downward flux of gas (Lube et al., 2019). Regardless of

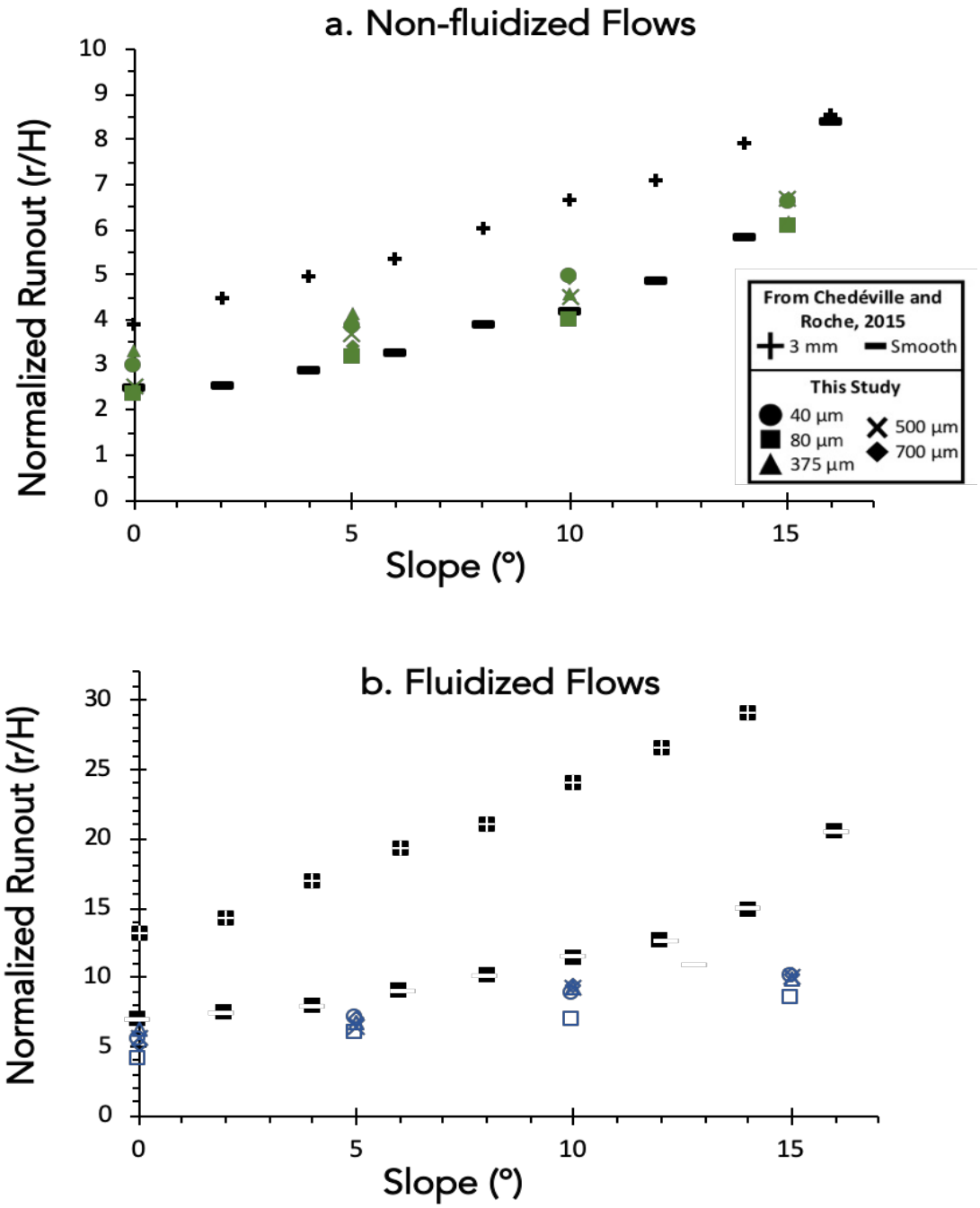

Figure 3.8 Runout distance for flows at different slope angles with erodible beds compared with data from Chédeville and Roche (2015) for flows at different slope angles with either 3 mm beads glued to the bed (pluses) or a smooth bed (dashes). A. For a given slope angle, our non-fluidized flows over an erodible bed travel farther than flows travelling over a smooth bed, but not as far as flows travelling over a bed with 3 mm fixed beads. B. In contrast, our fluidized flows on an erodible bed travel shorter distances than either fluidized flows travelling over a smooth bed or a bed with 3 mm fixed beads.

mechanism for generation, studies measure elevated pore fluid pressures in the bodies of experimentally-produced debris flows (e.g. Iverson, 1997; Major and Iverson, 1999) and gas-particle flows simulating pyroclastic currents (e.g. Roche et al. 2010; Lube et al., 2019). In addition, field measurements of debris flows and snow avalanches suggest natural flows generate the same elevated internal pore fluid pressures measured in experiments (e.g. McElwaine and Turnbull, 2005; McArdell et al., 2007).

The effect of the elevated pore fluid pressures is to reduce particle interactions that dissipate flow energy as friction, and this effect will persist as long as pore fluid pressures remain elevated. Therefore, the diffusion timescale of pore fluid pressure is an important parameter for understanding the overall behavior of gas-particle flows (e.g. Major and Iverson, 1999; Roche et al., 2010). Previous studies that calculate the timescale of pore pressure diffusion assume pore pressure originates at the base of a flow and diffuses as a result of the pore pressure gradient through the height of the flow until it equilibrates with the ambient (Druitt et al., 2007). For the majority of these previous experiments, this assumption holds true because the impermeable channel base forces the upward diffusion of pore fluid pressure (e.g. Mangeney et al. 2010; Roche et al. 2010; Farin et al. 2014; Lube et al. 2019).

In our experiments, however, the bed is not rigid or thin, and instead consists of a permeable network of beads that is at least as thick as the flows (4 cm). We interpret that the presence of the porous bed allows pore fluid pressure to diffuse in two directions, both upwards through the flow and down into the substrate (Figure 3.9). Because of this difference in boundary conditions in our experiments, the flow thickness is no longer the appropriate length scale for modelling the pore pressure diffusion timescale. The

bidirectional diffusion of pore fluid pressure decreases the timescale for pore pressure diffusion. A decreased diffusion timescale leads to frictional forces dominating earlier in the flow evolution and thus an earlier onset of deceleration and flow stoppage, which may explain the decreased runout distance we observe in our experiments relative to those of earlier studies. It is likely that the thin, erodible beds of Mangeney et al. (2010) and Farin et al. (2014) would behave somewhat in between the end members of an impermeable base and a thick porous base.

Mechanism of erosion

Previous experiments measure a negative pore fluid pressure (relative to the ambient) just behind the leading edge of gas-particle flows (Roche et al., 2010, Roche, 2012), debris flows (Major and Iverson, 1999), and snow avalanches (Louge et al., 2011). The low pore fluid pressure in the flow head produces an upward directed pressure gradient from the bed up into the flow, assuming that the pore fluid pressure of the bed remains at atmospheric. For snow avalanches in particular, the upward directed pressure gradient is associated with basal entrainment of bed material into the flow (Louge et al., 2011). Sometimes this effect is so dramatic that it causes “eruption currents” to form as blowouts at the fronts of snow avalanches (Louge et al., 2011) and leads to increases in the flow mass by more than 10 times the original mass (Sovilla et al., 2006). A similar process explains erosion by high-concentration pyroclastic currents whereby individual clasts can be uplifted from the bed into the flow (Roche et al., 2013; Pollock et al., 2016).

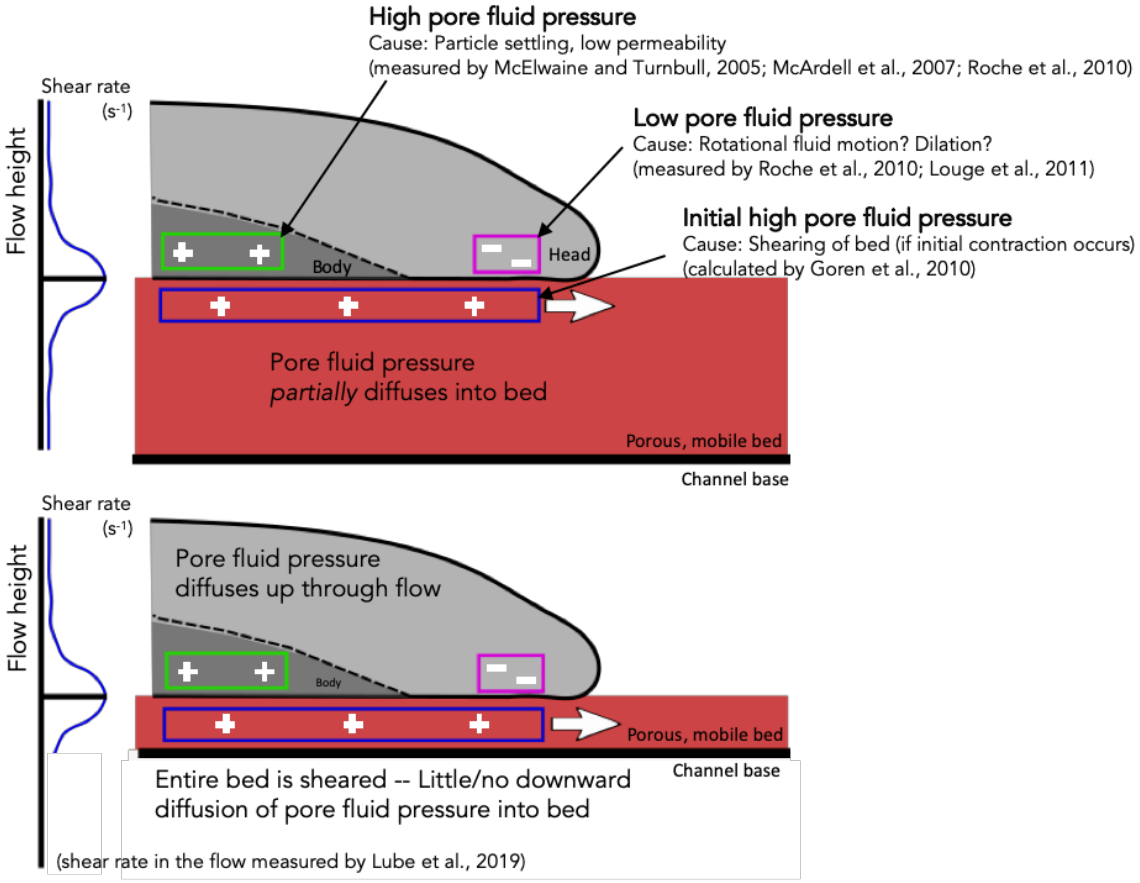

Figure 3.9 Sketch synthesizing previous work that measures pore fluid pressure in gas-particle flows. Negative pore fluid pressures (relative to ambient) occur just behind the flow front (pink box), while elevated pore fluid pressures occur in the body of flows as particle sediment and the flow compacts (green box). Additionally, elevated pore fluid pressures are expected in the uppermost part of a mobile bed due to shear (blue box). In summary, the combination of these pore fluid pressure "zones" within the gas-particle system results in a high pore fluid pressure gradient just behind the head of the current directed upwards from the bed into the flow. The high pressure gradient aids in basal entrainment and explains our observation of high material entrainment rates in the head of the current. Additionally, the elevated pore fluid pressure zone at the flow-bed interface within the body of the flow determines the overall behavior of the current. If the erodible bed is thin, the pore fluid pressure must diffuse upwards through the flow, extending runout distances. However, if the erodible bed is thick, pore fluid pressures can diffuse both up through the flow and into the bed as well, decreasing the runout distance relative to flows travelling over thin beds.

In our experiments, both dry and initially fluidized flows entrain bed material via mixing that occurs just behind the head of the current. The flow-bed interface becomes wavy before material is uplifted and carried along with the flow. This mixing process is more efficient in initially fluidized flows relative to dry flows. We suggest that the mixing and entrainment observed in our experiments is due to the fluid-like properties of the flows (Roche et al., 2010). The formation of pressure gradients at the flow-bed interface just behind the leading edge of the flows may additionally aid in the mixing and entrainment processes. The pressure gradient could result from either rotational motion in the flow head (McElwaine, 2005) or relative motion between the flow and the static substrate (Breard et al., 2019).

In addition, the mixing structures produced in our experiments resemble recumbent flame structures found in the deposits of turbidity currents (Dasgupta, 1998), pyroclastic currents (Rowley et al., 2011; Douillet et al., 2018; Pollock et al., 2019), and tsunamis (Matsumoto et al., 2008). Following previous studies, we suggest that the structures form as the result of granular shear instabilities formed at the flow-bed interface (Rowley et al., 2011; Farin et al., 2014; Pollock et al., 2019). The morphology of these mixing structures may reflect conditions within the flow (Rowley et al., 2011; Pollock et al., 2019), and similar experiments to those presented here may provide the ability to extract scaling relationships that relate the dimensions of the structures to flow parameters. However, a full analysis of the evolution of these structures and the potential derivation of scaling relationships is outside the scope of this study.

Unsteadiness at high slopes

Our experiments reveal unsteady, pulsating behavior in both fluidized and non-fluidized flows, which becomes more common as the bed slope angle increases. In addition, pulsation at the flow front is more common in fluidized flows than non-fluidized flows, but pulsating does occur in both instances. Because both high bed slope angles and fluidization promote higher flow velocities (Figure 3.4), unsteadiness appears to develop preferentially at higher velocities and also correlates with calculated Froude numbers (Figure 3.5). Unsteadiness and pulsating flow front behavior occurs in other experiments of fluid-particle mixtures including fluidized and non-fluidized granular flows (Chédeville and Roche, 2014; Chédeville and Roche, 2015), dilute particle-laden density currents (Andrews and Manga, 2012; Andrews, 2014; Andrews, 2019), and experimentally produced debris flows (Davies, 1990).

While the pulsating behavior in our experiments is associated with high velocity flows and high Froude numbers, the ultimate cause of the unsteadiness remains unclear. In debris flows, the preferential segregation of large clasts to the flow front is thought to promote surging behavior observed in both experiments and nature (e.g. Davies, 1990; Hungr, 2000; Savage and Iverson, 2003). However, the flows in our experiments comprise monodisperse particles. The high Froude numbers indicate supercritical flow in which the flow velocities are greater than the velocities at which instabilities formed at the surface would travel. However, these flow velocities are average velocities over the entire flow length and may not reflect the decreased flow front velocities that occur just prior to a pulse overtaking the flow front. Therefore, pulsating behavior may reflect deceleration of the front of the flow that ultimately allows more rapid, trailing parts of the flow overtake the

flow front. The more rapid trailing parts of the flow could be instabilities formed at the upper flow surface, or simply the body of the flow that travels rapidly enough to overtake the flow front. More work is necessary to fully understand the causes of unsteadiness in gas-particle flows.

Implications for gas-particle flows in nature – pore pressure diffusion and basal entrainment

Field evidence demonstrates that basal entrainment occurs for naturally occurring gas-particle flows, including both pyroclastic currents (e.g. Rowley et al., 1981; Sparks et al., 1997; Cole et al., 1998; Calder et al., 2000; Bernard et al., 2014; Pollock et al., 2016) and snow avalanches (e.g. Sovilla et al., 2001; Sovilla et al., 2006; Steinkogler et al., 2014). Additional studies show that basal entrainment affects the behavior of gas-particle flows in complex ways depending on the nature of the entrained material. Snow avalanches preferentially entrain colder temperature snow (Steinkogler et al., 2014), which can lead to bulking of the flow mass by ten times its original mass (Sovilla et al., 2006). For dilute pyroclastic currents, numerical models suggest basal entrainment increases the runout distance by over an order of magnitude (Fauria et al., 2016). Additionally, the runout distance of dilute pyroclastic currents is strongly influenced by the temperature of the entrained material, with entrainment of colder clasts promoting enhanced runout distances (Fauria et al., 2016). While these studies show that basal entrainment can affect flow runout distance, our experiments demonstrate that, under certain conditions, characteristics of the bed that promote pore pressure diffusion into the bed exert an even stronger control on the runout distance of gas-particle flows.

Simply stated, our results and those of previous experiments suggest that flow runout can be affected, either positively or negatively, by the permeability of the bed. Our experiments employ a thick bed of cohesionless, monodisperse particles whose permeability is $k \sim 1.1 \cdot 10^{-11}$ m^2 (Roche, 2012). In nature, the bed material could be quite varied. For pyroclastic currents, the bed material is likely either earlier pyroclastic deposits, soils derived from volcanic material, or bed rock; for snow avalanches the bed material is typically ice or snow. The permeability of pyroclastic deposits from the Taupo Volcanic Zone ($k = 3.6 \cdot 10^{-11}$ - $2.2 \cdot 10^{-12}$ m^2; Breard et al., 2019) and for volcanic soils (Moldrup et al., 2014) are similar to the permeabilities of the granular beds used in our experiments. Additionally, the experimental granular beds have slightly lower permeabilities than those reported for icy snow cover (Albert and Perron, 2000) or melting snow (Colbeck and Anderson, 1982). Therefore, based on the permeabilities of beds expected in nature, we hypothesize that a similar downward diffusion of pore pressure could occur for natural gas-particle flows.

Finally, as suggested by Iverson et al. (2011), the pre-existing pore fluid pressure conditions of the entrained bed material can affect the flow behavior in dramatically different ways. For pyroclastic currents, two commonly encountered bed conditions that could affect pore fluid pressure conditions are wet river valleys and the deposits of recent pyroclastic currents. When travelling down a river valley, pyroclastic currents will interact with water in both the stream itself and also the saturated sediments in the surrounding area. The elevated temperatures of pyroclastic currents would vaporize any surface or pore water the flow contacts. The rapid addition of gas into the current serves as an additional source of pore fluid pressure.

Additionally, over the course of an eruption, a pyroclastic current may travel overtop of recently deposited material from earlier pyroclastic currents. In the case of Mount St Helens, the low permeability of the pyroclastic current deposits allowed for the retention of gas days and even weeks after the eruption. When clasts were thrown into the deposits, ripples formed at the deposit surface and gas and ash splashed out of the impact site (Rowley et al., 1981). Similar to the observations of Iverson et al. (2011), if a pyroclastic current travelled overtop of these gas-rich deposits and entrained material with elevated pore fluid pressures, the current may travel farther than expected.

In summary, the characteristics of the bed affects the runout of gas-particle flows in complex ways. The runout distance, and thus hazard potential, of these flows will either increase or decrease depending on the bed thickness, permeability, yield strength, and the state of pore fluid pressure in the bed. Future studies, including numerical modeling, will be necessary to farther constrain the relationships between bed properties, pore pressure diffusion, and overall flow behavior.

Conclusions

Here we present the results of laboratory experiments investigating how the characteristics of the bed affect the behavior of both fluidized and non-fluidized gas-particle flows. The size of particles in the bed appears to have a negligible effect on flow runout distance. However, when the particles in the bed are the same size as particles in the flow, a slight decrease in runout distance occurs, which is likely due to roughness imposed by the bed and a lack of autofluidization.

In contrast to previous studies and despite our observation that basal entrainment readily occurs, we do not observe an increase in runout distance for fluidized flows

traveling overtop an erodible bed relative to fluidized flows travelling overtop a rough, fixed bed. To explain this discrepancy, we point to the importance of pore fluid pressure diffusion. From previous studies, we know that pore fluid pressure lows occur in the flow head and elevated pore fluid pressures occur in the body. Additionally, we know from numerical modeling that elevated pore fluid pressures should also occur (at least initially) in the sheared upper portion of the erodible bed if the bed was originally at loose packing. Together, these observations suggest the presence of an upward directed pressure gradient in the flow head and a zone of high pore fluid pressure near the flow-bed interface in the flow body.

The upward directed pressure gradient in the flow head explains the entrainment and mixing of bed material into the flow head. The effect of the elevated pore fluid pressure zone in the body depends on the thickness of the bed. If the erodible bed is thin, the majority of pore fluid pressure is forced to diffuse upwards through the flow. The upward diffusion of pore fluid pressure effectively increases the runout distance of the flows. If instead, as was the case in our experiments, the erodible bed is thick, we interpret that pore fluid pressures can diffuse both up through the flow and down into the bed. The diffusion of pore fluid pressure in two directions results in decreased runout distances relative to either flows over a thin erodible bed or a rough, fixed bed.

The results of our experiments demonstrate that bed characteristics can strongly affect the behavior of gas-particle flows, such as pyroclastic currents and snow avalanches, because bed properties play a key role in processes related to the diffusion of pore fluid pressure. Understanding pore fluid pressure diffusion is essential for understanding the

behavior of gas-particle flows and ultimately to better predicting the hazards associated with these dangerous currents.

Finally, our study motivates continued experimental and numerical studies investigating processes related to pore fluid pressure diffusion in gas-particle flows. Future work could explore how the behavior of gas-particle flows change as the thickness of an erodible, porous bed increases. Additionally, experiments using a porous, but rigid (i.e. non-erodible), bed of varying thickness could help to farther disentangle the effects of pore fluid pressure diffusion and material addition via basal entrainment. Finally, the dimensions of the mixing structures produced at the flow-bed interface may relate to important flow parameters, and future studies can extract these scaling relationships with the ultimate goal of using the relationships to extract information from natural deposits. These future studies will continue to improve our understanding of what controls the behavior of pyroclastic currents and snow avalanches.

Acknowledgements

This work is funded by a grant from the National Science Foundation (Award Number: 1347385).

CHAPTER FOUR: SHEAR INSTABILITIES FORMED AT THE FLOW-BED INTERFACE IN FLUIDIZED GRANULAR FLOWS

Abstract

Gas-particle flows occur in a variety of settings across the Earth's surface with examples including pyroclastic currents and snow avalanches. The processes of sediment transport, deposition, and erosion all affect the overall behavior and runout distance of gas-particle flows. Over the past 50 years, the processes of transport and deposition have been relatively well-studied, but many questions remain regarding the erosional processes that occur within gas-particle flows and their effects on flow behavior. Here we present the results of analogue laboratory experiments that investigate the erosion and mixing processes that occur between a fluidized gas-particle flow and a granular bed. Mixing at the flow-bed interface produces wave-like structures where the bed material is uplifted into the overriding flow and dragged along some distance before being deposited. We investigate the evolution of these mixing structures through time and determine the relationship between the morphology of the structures and physical flow parameters. The size of mixing structures, both length (L) and height (H), increases with increasing flow velocity and increasing bed grain size. We observe that the increases in length and height scale with the flow velocity and the flow thickness, and we use the experimental data to extract the quantitative scaling relationships. These relationships allow us to extract quantitative information about the flow conditions at the time the structures formed. For

example, the flow velocity is equal to $\alpha L^{\frac{1}{4}}$ where α is an experimentally determined constant and the flow thickness is between 2.5H and 7.5H. We use a local gradient Richardson number to explore whether shear on the flow-bed interface is sufficient to induce mixing, and find that the shear forces are strong enough to overcome the buoyant forces, thus possibly leading to the observed mixing observed. We suggest that the mixing structures form as a result of granular shear instabilities on the flow-bed interface that subsequently propagate along the interface until recorded in the deposits. We believe the granular shear instabilities to be analogous to Kelvin-Helmholtz instabilities that form in pure fluids and that the instabilities are able to form in our experiments due to the fluid-like properties of the flow-bed interface. Finally, we demonstrate how the scaling relationships extracted from the experimental data allow for the quantitative extraction of flow parameters from the deposits of natural pyroclastic currents that were produced during the May 18, 1980 eruption of Mount St Helens. The largest structures suggest flow velocities of ~8 $m \cdot s^{-1}$ and flow thickness of 5-15 m, both of these agree well with estimates for the parameters of similar pyroclastic currents. This approach shows promise for synthesizing field and experimental approaches to extract information about flow velocities and thicknesses from natural deposits, and the datasets produced as a result could potentially be used to test the numerical models that are becoming increasingly important for hazard and risk assessment for these dangerous currents.

Introduction

Fluid-particle flows are complex, multiphase mixtures of solid particles and gas or liquid whose dynamics are largely a function of the proportion of particles to fluid (Delannay et al. 2015; Dufek 2016). These flows naturally occur in a variety of settings

across Earth's surface, and examples include pyroclastic currents, snow avalanches, debris flows, and turbidity currents. Fluid-particle flows often occur with little warning and can pose a significant threat to populations or infrastructure located along their paths; Thus, understanding the processes that control the behavior of these flows is essential.

Over a century of research investigates the interaction of water with a granular bed for the purposes of understanding subaqueous sediment transport (Sorby 1859; Forchheimer 1914; Gilbert 1914). Numerous studies examine both the effect of the flow on bed characteristics (i.e. grain size, bedforms, channel morphology; e.g. Allen 1976; Bridge and Best 1988; Southard and Boguchwal 1990)) as well as the effect of bed characteristics on flow behavior (e.g. Thibodeaux and Boyle 1987; Clifford et al. 1992; Boano et al. 2007). While these processes are well-studied for aqueous systems, similar investigations of flow-bed interactions for gas-particle flows are limited to the last few decades. In this study, we build on recent additions to the granular flow literature and examine the interaction of gas-particle flows with a granular bed, the processes by which mixing occurs between the flow and its bed, the morphology of the structures produced as a result of the flow-bed interactions, and how such structures can be used to extract quantitative information from the deposits of natural pyroclastic currents.

Recent experimental studies demonstrate that mixing occurs between a granular flow and its initially static granular bed (e.g. Mangeney et al. 2010; Rowley et al. 2011; Roche et al. 2013; Farin et al. 2014), and that in some scenarios mixing and material entrainment increase the runout distance of granular flows by up to 50% (Mangeney et al. 2010; Farin et al. 2014). These experimental studies propose that the erosion and mixing occurs because of the formation of granular shear instabilities at the flow-bed interface

(Rowley et al. 2011; Farin et al. 2014). Additionally, field studies on the deposits of pyroclastic currents reveal sedimentary structures that suggest syn-depositional mixing between the flow and its bed (Rowley 2010; Douillet et al. 2018; Pollock et al. 2019). Pollock et al. (2019) suggest that recumbent flame structures preserved in the pyroclastic current deposits from the May 18, 1980 eruption of Mount St Helens represent the record of granular shear instabilities formed in natural gas-particle flows. The authors propose that these structures record important information about the flow conditions (i.e. velocity and deposition rates) at the time of emplacement. However, the previous studies, both field-based and experimental, suggest that granular shear instabilities form at the interface between gas-particle flows and granular substrates, additional systematic investigations of the mixing processes that occur between granular flows and their beds are necessary to fully elucidate these basal processes.

Here we present the results from a series of experiments investigating the formation of mixing structures formed at the flow-bed interface of fluidized granular flows. Our experiments systematically explore how the slope and size of particles in the erodible bed affect mixing between the flow and its bed. We observe that mixing occurs in all experimental configurations, but the height and length of the structures vary over an order of magnitude and depend on the initial conditions. We hypothesize that these mixing structures form due to granular shear instabilities and represent the equivalent of Kelvin-Helmholtz instabilities in pure fluids. We use an analytical approach to investigate whether shear is sufficient to induce the mixing observed in the experiments. Finally, we determine the relationships between the morphology of the structures and measurable flow parameters

with the goal of using the dimensions of mixing structures preserved in natural deposits to infer the conditions of formation.

Background

Sedimentary structures record the conditions of their formation

Since at least the 1960s, studies explored the relationships between the morphology of sedimentary structures and the conditions that produced them (e.g. Yalin 1964, Allen 1968). The goal of these types of studies is to use the morphology of sedimentary structures preserved in the rock record to interpret the conditions at the time the structures formed. Examples of scaling relationships that allowed for quantitative interpretations of the rock record include using the dimensions of bedforms to interpret flow height and velocity (Yalin 1964), flute marks in fluvial sediments to interpret flow velocity (Allen 1968), grain size characteristics of turbidite deposits to interpret the hydraulic conditions (Komar 1985), and the imprint of raindrops to interpret atmospheric conditions (Som et al. 2012). The scaling relationships originally derived by Yalin (1964) still appear in sedimentology textbooks and successfully predict the morphology of subaqueous bedforms for the vast majority of flow conditions (Allen 1984; Garcia 2008). While recent studies question the application of the bedform scaling relationships to certain flow conditions (cf. Bradley and Venditti 2017), attempts persist to find the appropriate scaling relationships to relate sedimentary structures to the conditions of their formation (e.g. Bartholdy et al. 2015; Lapotre et al. 2017; Bradley and Venditti 2019).

Despite the more than 50 years of research exploring scaling relationships for subaqueous sedimentary structures, the investigation of flow-bed interactions and the structures formed at the base of gas-particle flows is relatively recent (e.g. Mangeney et al.

2010; Rowley et al. 2011; Roche et al. 2013; Farin et al. 2014). While some sedimentary structures (bedforms, for example) preserved in the rock record are likely to be truncated by erosive surfaces (Allen 1984), gas-particle flows such as pyroclastic currents potentially preserve certain sedimentary structures in their entirety and without subsequent erosion (Pollock et al. 2019). If scaling relationships can be developed for such structures formed in gas-particle flows, the preservation potential in deposits from gas-particle flows is an advantage in interpreting flow conditions from structure morphology.

Sedimentary structures in experimental and numerical gas-particle flows

Previous experimental studies investigating the interaction between granular flows and a granular bed observe that shearing of the flow-bed interface leads to the reworking and entrainment of bed material into the flow (e.g. Ciamarra et al. 2005; Rowley et al. 2011; Roche et al. 2013; Farin et al. 2014). For example, Goldfarb et al. (2002) investigates the evolution of the contact between two parallel granular flows traveling next to each other at different velocities and shearing along a vertical contact. As the difference in velocities between the two flows increases, the contact evolves from planar to wavy and eventually to the formation of breaking waves. Goldfarb et al. (2002) attributes the growth of the waves to granular shear instabilities formed at the unstable interface between the two parallel flows. Similarly, Ciamarra et al. (2005) numerically simulates dry granular flows travelling over an erodible bed to study the interactions between the flow and its bed. The simulations demonstrate that high shear stress is exerted on the bed by the flow, eventually producing a wavy contact due to the onset of shear instability growth. Ciamarra et al. (2005) suggest that the instabilities observed in their numerical experiments are analogous to Kelvin-Helmholtz instabilities formed in shearing Newtonian fluids.

A series of recent granular flow experiments investigate how flows interact with erodible, granular beds and produce structures similar to those observed in the numerical results of Ciamarra et al. (2005) (e.g. Mangeney et al. 2010; Rowley et al. 2011; Roche et al. 2013; Farin et al. 2014). For example, Rowley et al. (2011) observe vortical mixing features formed as colored granular charges travel over a granular bed. The experiments of Mangeney et al. (2010) and Farin et al. (2014) produce "erosion waves" that propagate downstream at the flow-bed interface and whose amplitude and wavelength increase as the bed slope increases. Roche et al. (2013) observe sheared flame structures propagating at the interface between a fine-grained granular substrate and both initially fluidized and dry granular flows. The authors of these studies attribute mixing at the flow-bed interface to granular shear instabilities, which are akin to Kelvin-Helmholtz instabilities that form in pure fluids (Rowley et al. 2011; Roche et al. 2013; Farin et al. 2014).

Here, we use the general term "mixing structure" to refer to any instance of bed material being reworked and uplifted in the flow before being deposited and preserved with the flow material. We extend the previous research that investigates the interaction of granular flows with an erodible bed to test the following hypotheses:

1. Mixing between a gas-particle flow and a granular bed occurs due to shear exerted on the flow-bed interface, which leads to granular shear instabilities similar to Kelvin-Helmholtz instabilities that form in pure fluids.
2. The structures formed as a result of mixing will propagate along the flow-bed interface at a velocity that is proportional to its distance from the flow front (i.e. a horizontal velocity gradient exists that decreases with distance from the flow front).

3. The dimensions of the mixing structures (length and height) will scale with flow parameters such as flow velocity and flow thickness.
4. The scaling relationships observed in the experimental mixing processes can be applied to mixing structures observed in the deposits of natural gas-particle flows to extract quantitative information from the sedimentary structures.

Methods

Experimental apparatus

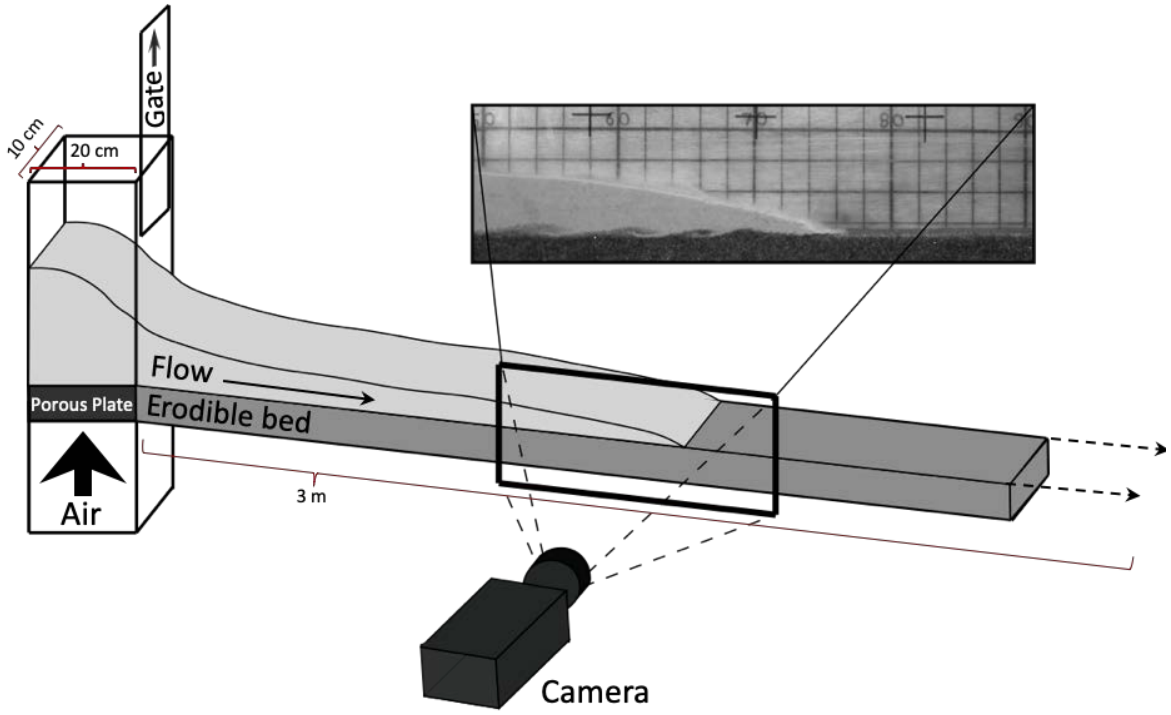

Figure 4.1 Sketch of experimental apparatus modified from Pollock (Chapter 3). Apparatus consists of reservoir that attaches to a 3 m long channel by means of a sluice gate that opens via a counterweight. The reservoir connects to a compressed air system that supplies air to the base through a porous plate which allows for fluidization of the granular mixture prior to initiating an experiment. Camera captures 30-50 cm window in the middle of the flow runout to maximize observation of mixing that occurs between the flow and bed (inset).

The experiments presented here use the same experimental apparatus as Roche et al. (2013), Chedeville and Roche (2014; 2015), and Pollock (Chapter 3). The experimental design fulfills scaling requirements to natural pyroclastic currents as presented in Roche (2012), and the flow produced in the experiments are most analogous to the highly-concentrated end members of pyroclastic currents. The apparatus consists of a 3 m long, 10 cm wide channel constructed with perspex walls to allow for viewing of internal flow processes (Figure 4.1). The channel connects to a 20 cm by 10 cm reservoir that is filled with glass beads prior to the initiation of each experiment. A sluice gate separates the reservoir from the channel, and the gate is opened by the dropping of a counterweight. The gate opens rapidly enough to not affect the flow behavior once the flow exits the reservoir (Roche 2012). Additionally, a porous plate sits at the base of the reservoir and connects to a compressed air system capable of fluidizing the glass bead granular mixture prior to each experiment. The plate has pores that are 20 μm in diameter so that beads will not clog the pores. The compressed air system utilizes a series of manometers to control the air flux and dryers to minimize the effects of cohesion between particles. Finally, the channel inclines from horizontal up to a maximum of 20 degrees.

Prior to each experiment, we fill the reservoir to a height of 30 cm with sub-spherical, glass beads. The glass beads have an average diameter of 80 μm and density of 2500 kg/m^3. The base of the channel is roughened with a layer of fixed 3 mm glass beads and atop this basal layer, we pour an erodible bed of sub-spherical glass beads with average diameters of 40, 80, 375, 500, and 700 μm. The density of the beads in the erodible is the same as those that fill the reservoir, 2500 km/m^3. We fill the channel base to an even thickness of ~4 cm. We chose a thickness of 4 cm because in tests, once the bed was 4 cm

thick no movement of particle occurred at the contact between the erodible bed and the channel base, suggesting that all energy exerted by the flow on the erodible bed is taken up by the bed itself and not transferred to the channel base.

For all experiments, once the reservoir is filled with glass beads, air fluxes through the porous plate at the base of the reservoir for a minimum of 10 minutes to dry the granular mixture and control for effects of humidity. We run two types of experiments, fluidized and non-fluidized. For non-fluidized experiments, at the end of 10 minutes the air flux is shut off and the granular mixture completely defluidizes prior to opening of the gate. For fluidized experiments, at the end of 10 minutes the air flow velocity is adjusted to ~13 mm·s-1, which is above the minimum fluidization velocity (U_{mf}, Roche et al. 2006) and leads to slight expansion of the granular mixture (~3-5%). No gas is supplied from the channel base so that once the gate opens and the granular mixture propagates into the channel, the flows progressively defluidize via pore pressure diffusion. Because the permeability of the granular mixture is low (k~10^{-11} m^2; Roche et al., 2010; 2012), the timescale for pore pressure diffusion is slow relative to the timescale for advection of material into the channel. Therefore, the flow remains at least partially fluidized until enough gas diffusion occurs that behavior transitions to that of pure granular flow, eventually leading to stopping and deposition of the flow (Roche et al. 2010).

Measuring flow behavior and mixing processes

A high-speed video camera records each experiment with a field of view that ranges from 30 to 50 cm in length. For each experiment, the field of view is chosen based on observations of previous experiments to maximize the opportunity to observe mixing processes. The camera records the experiment at 1000 frames/s to allow for observation

of the rapid and often small-scale mixing processes. For each experiment, we calculate the flow front velocity across the field of view and measure the evolution of mixing structures that form at the flow-bed interface. We manually measure the dimensions of the mixing structures at three points in time for each experiment: shortly after *onset* of structure formation (the flow is about halfway across the field of view), after the *growth* of the structures for a period of time (when the flow front is exiting the field of view), and when the flow stops and the structures are preserved during *deposition* (Figure 4.2). For each point in time, we measure the length and height of each mixing structure and the thickness of the flow overtop of each structure (also depicted in Figure 4.2). In addition to the flow velocity, we also measure the velocity of the mixing structures as they propagate at the flow-bed interface and record the distance between the structures and the flow front.

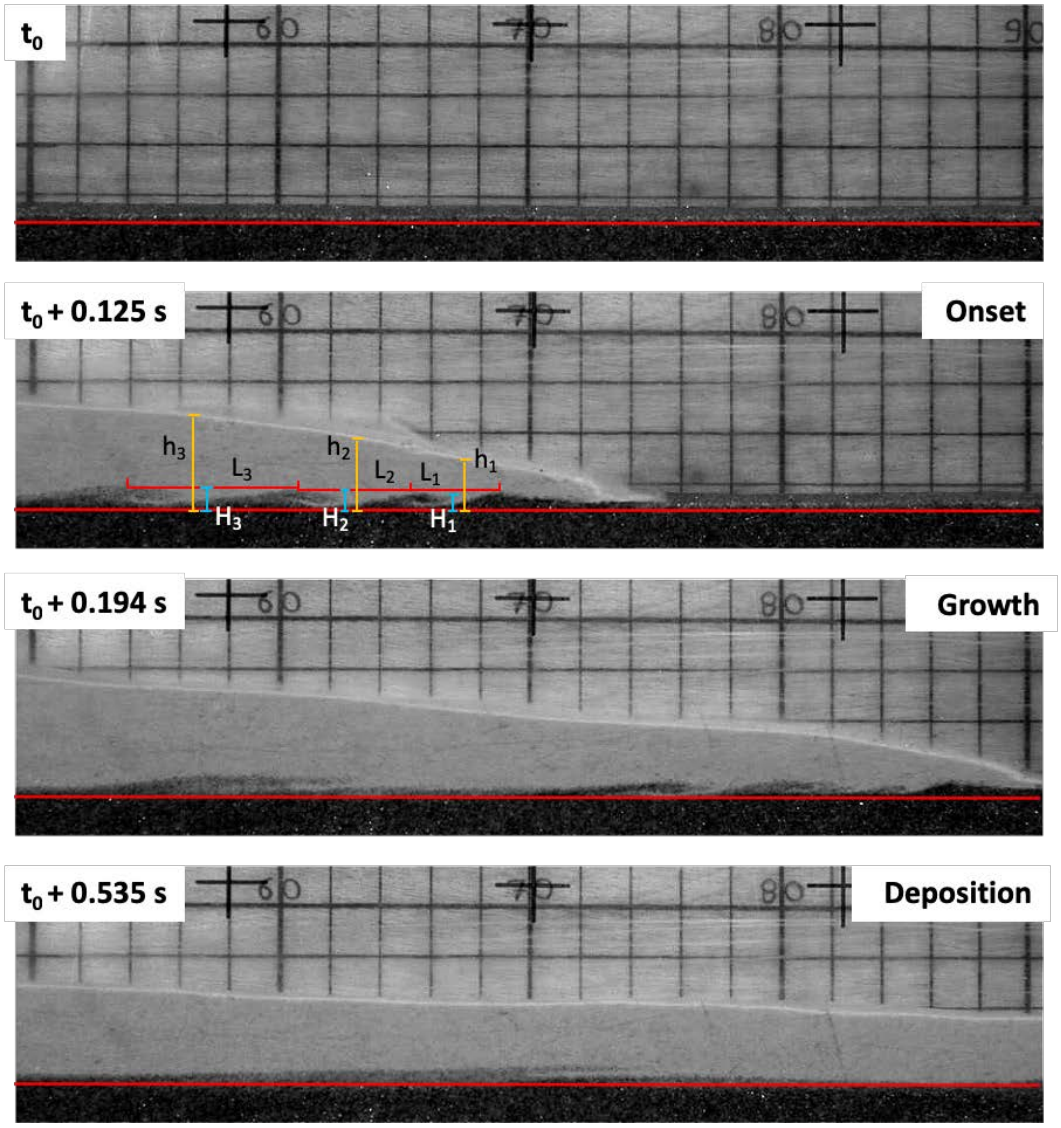

Figure 4.2 Example of three stages of mixing structure evolution: onset, growth, and deposition. The onset panel shows the scheme for measuring structure height (H), structure length (L), and the flow height (h).

Results

Flow front kinematics

The bed slope angle most significantly impacts flow front velocities, although the bed grain size also exerts some control on the velocity. As the bed slope angle increases from 0° to 20°, the flow velocities increase from an average of 1.6 $m \cdot s^{-1}$ at 0° to 2.7 $m \cdot s^{-1}$ at 20° (Figure 4.3a). However, the relationship between bed grain size and flow velocity is

more complex (Figure 4.3c); the fastest flow velocities occur when the flow travels over the finest bed grain size (40 μm), and the flows travel at the slowest velocities when travelling over a bed of 80 μm particles, which is the same grain size as particles in the flow. As the bed grain size increases from 375 to 700 μm, the flow velocities remain relatively constant between 2.35 and 2.5 $m \cdot s^{-1}$ (Figure 4.3b). The observation that flow velocities decrease when the bed contains 80 μm particles correlates with observations of previous experiments in which flows of 80 μm particles travel the shortest distances over beds of 80 μm particles (Chapter 3).

The flow velocities in our experiments remain nearly constant across the entire field of view, but this is likely affected by our choice of the viewing window for the experiments. The field of view for the videos is short relative to the total flow runout (30-50 cm viewing window vs 1-3 m total runout). Additionally, we chose the field of view to be in the middle of the total runout distance to maximize our chances of capturing mixing between the flow and bed. These choices for the field of view lead to capturing the flow during the second propagation phase of its evolution, the constant velocity phase, which is well documented by previous experiments (e.g, Roche et al. 2008; Roche 2012). Since our field of view and measurements only capture the second propagation phase, the data presented herein do not include the initial acceleration phase or the final deceleration phase.

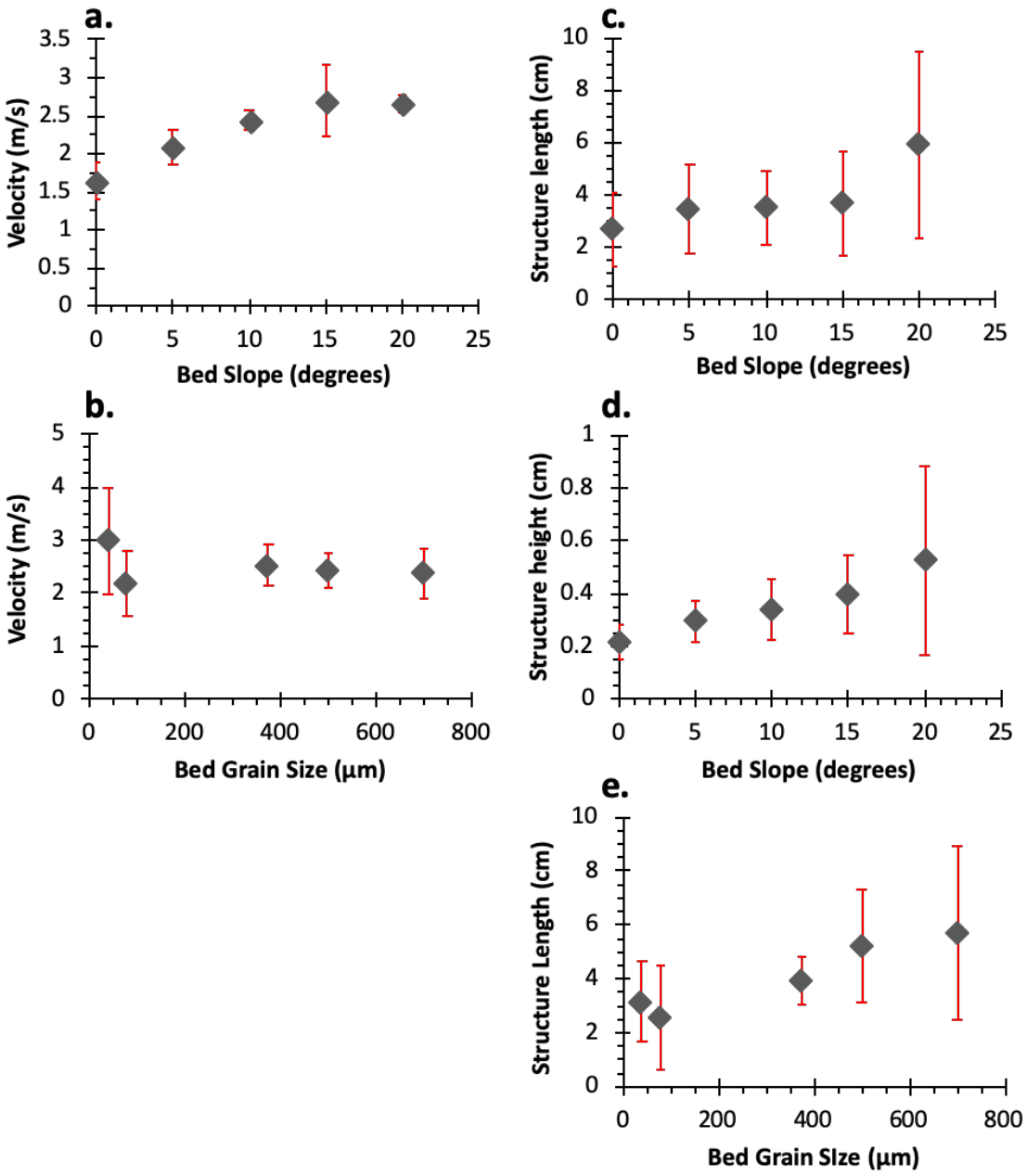

Figure 4.3 General trends of flow kinematics and mixing structure morphology. Averages indicated with gray diamonds and error bars show one standard deviation. (a) Flow velocity increases with increased bed slope. (b) Highest flow velocities occur for the finest bed grain size, while slowest flow velocities occur for flows travelling over 80 um bed. The flow velocity is relatively constant at higher bed grain sizes. (c) and (d) Structure length and structure height increase with increasing bed slope angle. (e) Structure length generally increases with increasing bed grain size, except for beds of 80 um particles, which produces the shortest structures on average.

Flow morphology

As the bed slope angle increases, the flow structure becomes increasingly complex. At slopes between 0° and 10°, the flow front is wedge shaped and gradually increases in thickness away from the front (Figure 4.4a and 4.4b). At slopes of 15° and 20°, the flow front becomes chaotic with splashing, thickening, and thinning of the flow overtop of the mixing structures (Figure 4.4c). We observe that at high slopes (10° to 20°) the upper surface of the flow mimics the shape of the mixing structures at the flow-bed interface (Figure 4.4b and 4.4c).

Mixing at the flow-bed interface

For all initial configurations, mixing occurs between the flow and the initially static bed, but the intensity of mixing varies based on the initial conditions. The mixing initially takes the form of small wave-like structures that occur with regular spacing along the flow-bed interface (Figures 4.2 and 4.4). As observed in the videos, the flow-bed interface evolves from initially planar to slightly wavy as the flow head passes, and as the flow continues the undulating surface evolves into breaking wave structures with billows that extend and thin in the downflow direction. As flow continues, the waves continue to elongate in the downflow direction until final deposition occurs.

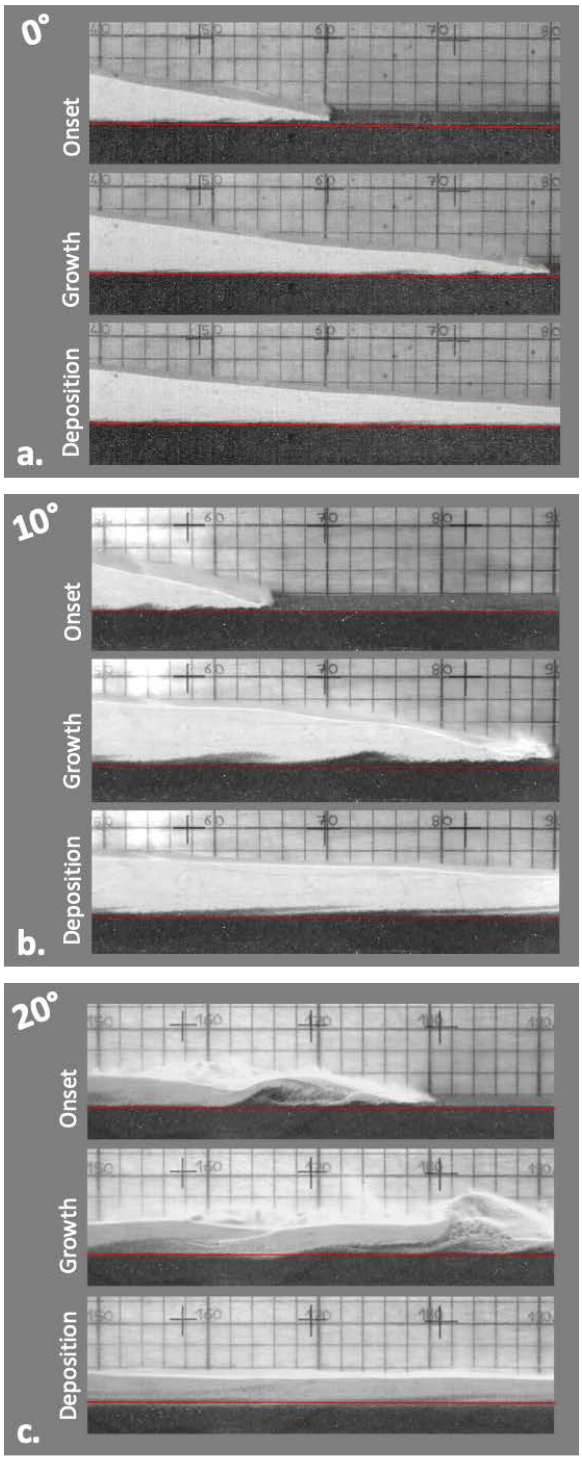

Figure 4.4 Three experiments all with a bed grain size of 700 um, but with increasing slope angle of 0° (a), 10° (b), and 20° (c). Note the similar wedge shape of the flow front on slopes of 0° and 10°, but when the slope is increased to 20°, the flow front behavior becomes more chaotic with splashing and thicknening and thinning of the flow overtop of the mixing structures. This behavior is similar for experiments run over the other bed grain sizes as well.

The dimensions of the mixing structures observed in the experiments relate to both the bed slope angle and the bed grain size. As the bed slope increases (and thus flow velocity as well), the length of the structures observed during the growth stage increases from an average of 2.6 cm at 0° to 5.9 cm at 20° (Figure 4.3c). Similarly, the height of structures increases as the bed slope increases, with structures averaging 0.2 cm in height at 0° and 0.5 cm in height at 20° (Figure 4.3d). Similar to the flow front velocity trends, the relationship between average structure length and bed grain size is slightly more complex. In general, the structure length increases with increasing bed grain size (Figure 4.3e), but the shortest structures occur when the bed grain size is 80 μm, which is also the grain size over which the flows travel the slowest (Figure 4.3b).

Over the three phases of mixing (onset, growth, and deposition), the morphology of the structures evolves in a predictable fashion. During onset of structure growth, the mixing structures are the most self-similar in form. Plotting all structures measured during the onset of structure growth shows a good correlation between the structure length and height ($R^2 = 0.62$; Figure 4.5a), but as the flow continues and structures continue to evolve until eventual deposition, the correlation progressively worsens (Figures 4.5a – 4.5c). Upon deposition, the correlation between structure length and height is relatively poor, although this correlation does appear to be negatively affected by a few outlier data points that mostly come from experiments on 20° ($R^2 = 0.29$; Figure 4.4c). Throughout these three phases, the structures gain most of their height between onset and growth, but the structures lengthen progressively until the structures are finally deposited as can be seen in the progressively decreasing slopes of the best-fit lines in Figures 4.5a, 4.5b, and 4.5c.

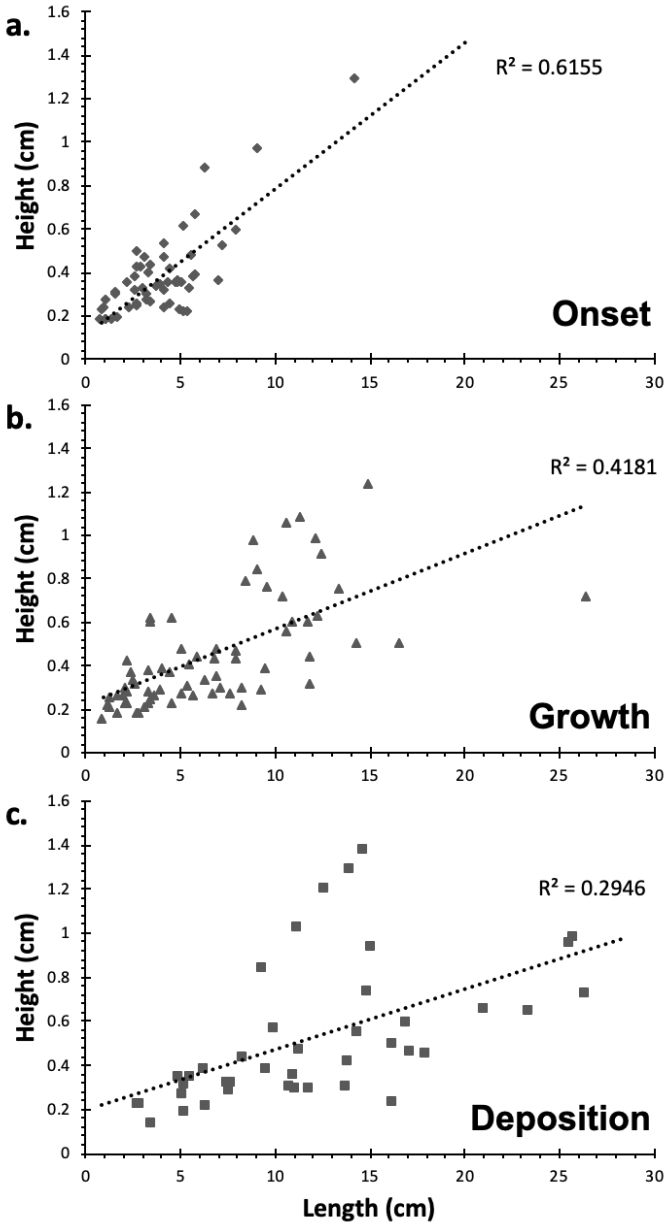

Figure 4.5 Mixing structure length versus height for the three phases of structure evolution: (a) onset, (b) growth, and (c) deposition. Note the decreasing correlation over the course of structure evolution. Height and length are best correlated during onset and growth, but poorly correlated upon deposition.

We also investigate the relationship between the height of the mixing structures and the total flow height above the structure and find that a moderate correlation exists during the onset and growth phases (Figure 4.6a and 4.6b). The structure height is best correlated with the flow height during the middle growth phase of the mixing structure evolution (R^2

= 0.45; Figure 4.6b). However, no correlation exists between the final structure height preserved in the deposit and the thickness of the deposit overtop of the structure (Figure 4.6c).

Internal mixing structure velocity

We also track the mixing structures as they propagate along the flow-bed interface and calculate their downstream velocity. Figure 4.7 shows the ratio of the mixing structure velocity to the flow front velocity plotted as a function of the distance the structure sits behind the flow front. Our hypothesis was that the farther from the flow front the mixing structure was, the slower the relative velocity would be; however, no correlation exists between these two parameters in our dataset. This observation suggests that for some flows, portions of the current far behind the flow front (up to 15 cm) can still propagate at velocities that are approximately half of the flow front velocity. Conversely, for other flows, portions of the flow just behind the flow front (3-4 cm) are propagating at less than a third of the flow front velocity. Perhaps the most interesting observation from this data is that there appears to be a maximum relative velocity. None of the mixing structures propagates at a velocity that is more than ~60% of the flow front velocity, and this maximum relative velocity remains constant regardless of the distance behind the flow front.

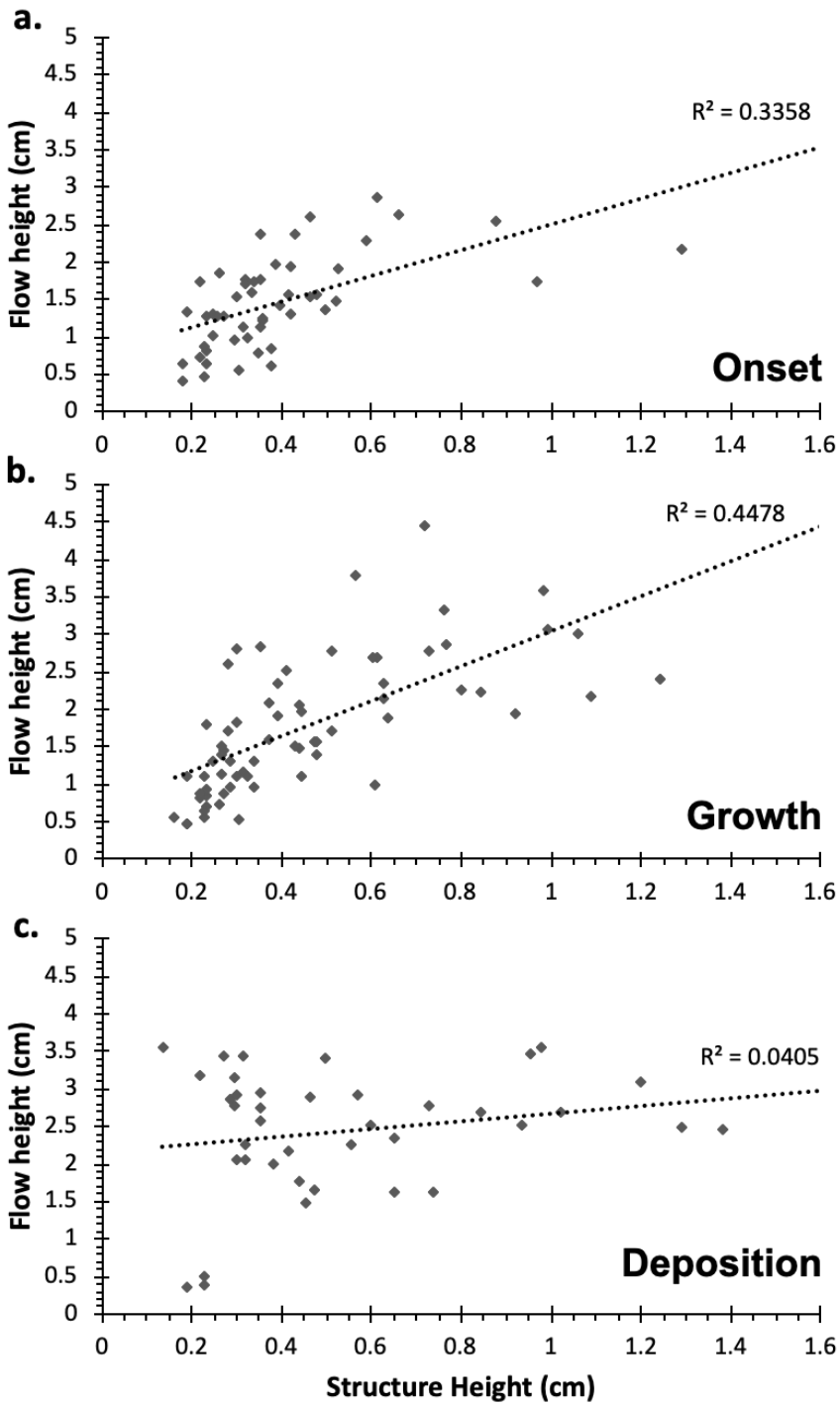

Figure 4.6 Mixing structure height versus flow height for the three phases of structure evolution: (a) onset, (b) growth, and (c) deposition. Note that the structures are best correlated with the flow height during the growth phase and essentially no correlation exists upon deposition. Additionally, little change in the structure height occurs between growth and deposition suggesting that the heights preserved in the deposits represent the heights of structures during growth.

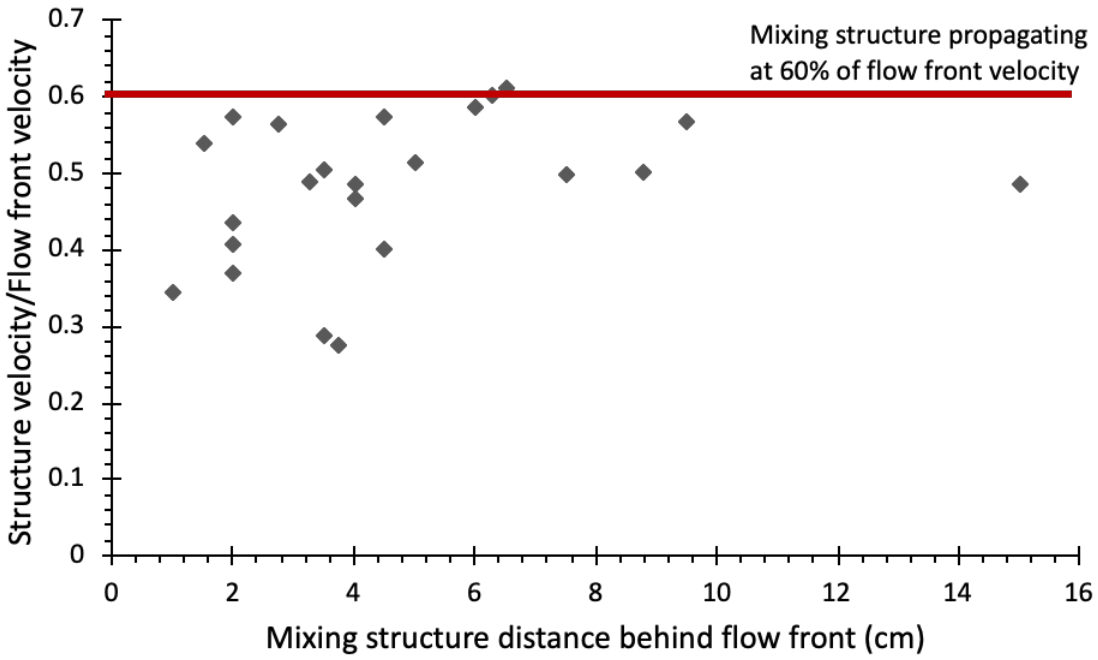

Figure 4.7 The velocity of the mixing structures relative the flow front velocity are plotted against the mixing structure's distance behind the flow front. No correlation exists between the relative flow velocity and distance behind the flow front. However, it appears that the mixing structures propagate at a maximum of 60% of the flow front speed indicated by the red horizontal line.

Discussion

Mechanism of mixing

The correlation of flow front velocity and bed roughness with the mixing structure length suggests that shear stress plays an important role in the onset and growth of the structures (Figures 4.3c and 4.3e). The shear stress, τ, in gravity currents is a function of the flow density and flow velocity (Allen 1985):

$$\tau = \frac{f_D}{8}\rho_{flow}^2 U^2 \qquad (Eqn.\ 4.1)$$

where ρ_{flow} is the flow density, U is the average flow front velocity, and f_D is a Darcy-Weisbach friction coefficient. The Darcy-Weisbach friction coefficient is a function of the bed roughness, the flow viscosity, velocity, and density (Papaevangelou et al. 2010).

While the flow density and viscosity likely do not vary by more than a factor of 2 in our experiments, the flow velocity and roughness vary by a factor of 3 and 17.5, respectively, which significantly changes the shear stress exerted on the bed depending on the initial conditions. The observation that structure length correlates with bed grain size and slope suggests that the larger magnitude changes in shear stress are causing the elongation of the mixing structures.

One way of investigating the effect of shear on the flow-bed interface is to calculate a local gradient Richardson number for the boundary in our experiments. The gradient Richardson number is the ratio between the stability of stratified flow due to buoyancy and the destabilizing effects of shear on that interface (Dufek 2016). The local gradient Richardson number is calculated as:

$$Ri_{grad} = \frac{\left(\frac{g}{\rho_{bed}}\right)\left(\frac{\partial \rho}{\partial y}\right)}{\left(\frac{\partial U}{\partial y}\right)^2} \qquad (Eqn.\ 4.2)$$

where g is gravity, ρ is the density, U is the velocity, and y is the vertical direction (Dufek 2016). The critical value of the gradient Richardson number is Ri ~ 0.25; when Ri<0.25, shear on the interface dominates and is sufficient to initiate mixing and entrainment, and when Ri>0.25 buoyancy dominates and the stratification of the two layers remains stable (Miles 1961; Dufek and Bergantz 2007a). A high density gradient across the interface will help to stabilize the interface, while a high velocity gradient will lead to mixing.

To investigate the stability of the flow-bed interface and calculate a gradient Richardson number, we approximate the flow and bed densities using the solid volume fraction and the particle density. Analogue experiments by Breard et al. (2018) use material

from the deposits of natural pyroclastic currents, and they measure solid volume fractions between 0.2 and 0.6 (Breard et al. 2018). While the scale and materials are different in their experiments relative to ours, the large range of solid volume fractions measured by Breard et al. (2018) likely captures the range of solid volume fractions in our flows because the flows are observed to be only minimally expanded from maximum packing ($\phi_{max} \sim 0.6$). We also assume the solid volume fraction of the bed is at loose random packing ($\phi_{bed} = 0.6$) as is expected for beads poured in to the channel (Dullien 1992).

In Figure 4.8a, we show the calculated gradient Richardson number for velocities of 0.5, 1.8, and 3.5 m· s^{-1} where 0.5 m·s^{-1} is the slowest internal (wavefront) velocity, 1.8 m·s^{-1} is the slowest flow front velocity, and 3.5 m·s^{-1} is the highest flow front velocity measured in our experiments. These velocities encapsulate the entire range of velocities observed in our experiments (shaded blue area in Figure 4.8a), and, as indicated with the red horizontal line, the calculated gradient Richardson numbers are less than 0.25 for all expected velocities and solid volume fractions. Unless the flow travels at especially slow velocities (0.1-0.5 m·s^{-1}) or is at very low solid volume fractions, these calculations suggest that the shear exerted by the flow onto the bed is sufficient to generate mixing at the flow-bed interface.

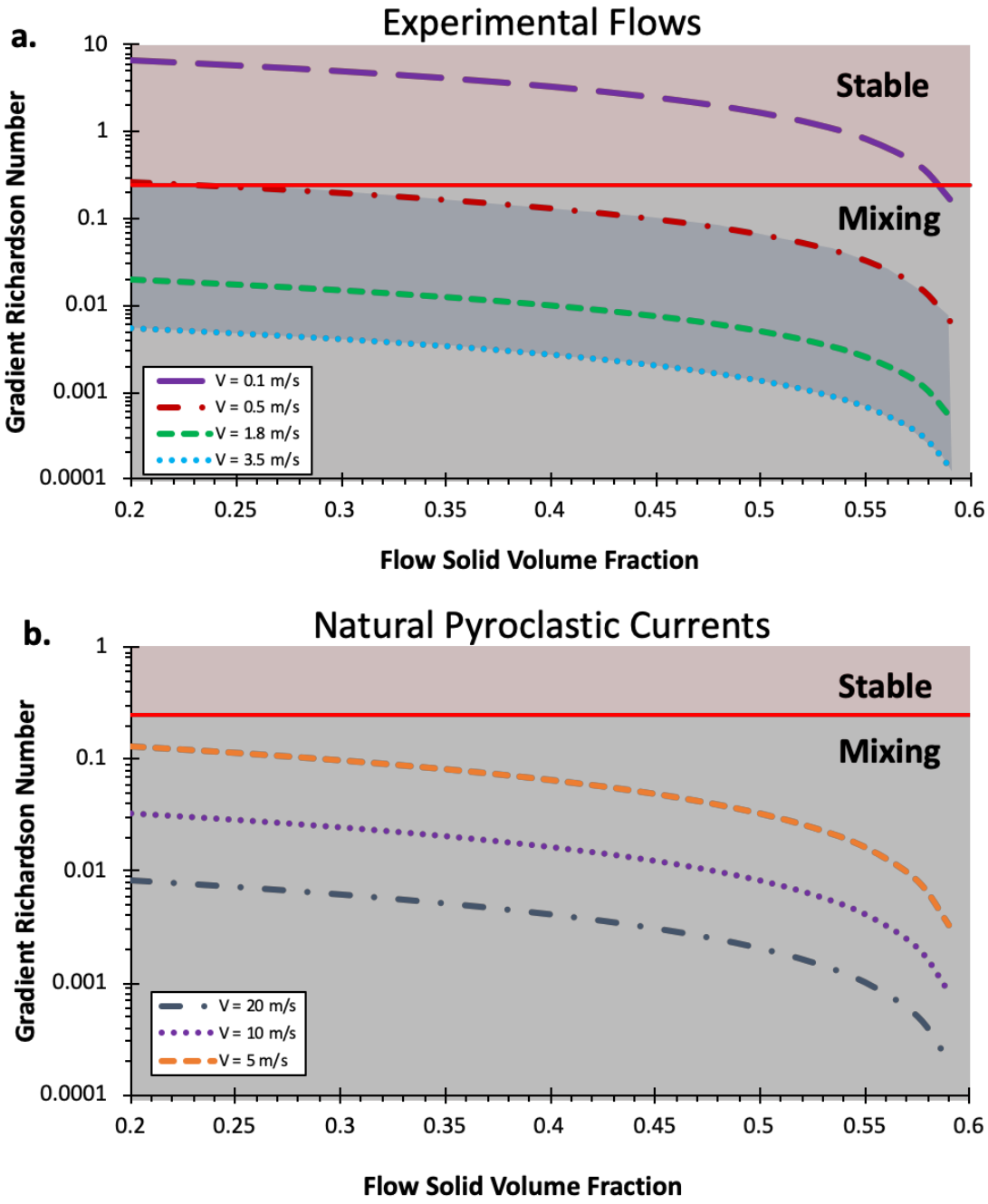

Figure 4.8 Calculated gradient Richardson numbers for (a) the experimental flows and (b) natural pyroclastic currents. Horizontal red line indicates the critical Richardson number, Ri = 0.25. Above this value of Ri the interface between the flow and the bed is stable, but below this value mixing will occur. Colored lines indicate the calculated Ri for a given flow front velocity over the range of solid volume fractions expected for experimental and natural flows. All measured and expected velocities fall below the critical Ri suggesting that mixing can occur for both the experimental and natural flows.

Additionally, we follow the approach of Rowley et al. (2011) and Farin et al. (2014) and investigate whether the mixing observed in our experiments could be due to the formation of granular shear instabilities akin to Kelvin-Helmholtz instabilities in pure fluids. The formation of instabilities along an interface between two shearing Newtonian fluids can be predicted using an instability growth criterion (Kundu and Cohen 2004). The criterion shows that for a given density contrast between the two fluids, instabilities will develop when the velocity difference across the interface exceeds a minimum threshold.

Rowley et al. (2011) and Farin et al. (2014) adapt the instability growth criterion for gas-particle flows and observe that the growth criterion predicts the formation of shear instabilities in their experiments. We similarly use the instability growth criterion and measurements of mixing structures produced in our experiments to investigate whether the onset of mixing is predicted by the instability growth criterion. From Rowley et al. (2011), the instability growth criterion states that an interface will be unstable, leading to the growth of shear instability waves, when:

$$v_1 - v_2 \geq \sqrt{\frac{g\lambda}{2\pi}\left(\frac{\phi_2}{\phi_1} - \frac{\phi_1}{\phi_2}\right)} \qquad (Eqn. 4.3)$$

where v_1 and v_2 are the velocities of the flow and bed, respectively, g is the acceleration due to gravity, and λ is the wavelength of the mixing structure. Here, $(\phi_2/\phi_1) - (\phi_1/\phi_2)$ is the relative solid volume fraction between the flow and the substrate, where ϕ_1 is the volume fraction of particles in the flow and ϕ_2 is the volume fraction particles in the substrate (Rowley et al. 2011). We assume the velocity of the substrate is negligible at the time of instability growth, and therefore:

$$v_1 \geq \sqrt{\frac{g\lambda}{2\pi}\left(\frac{\phi_2}{\phi_1} - \frac{\phi_1}{\phi_2}\right)} \qquad (Eqn.\ 4.4)$$

To solve for the velocity at the time of instability formation, we use the length of the mixing structures and the same assumptions as above regarding the solid volume fraction in the flow and bed.

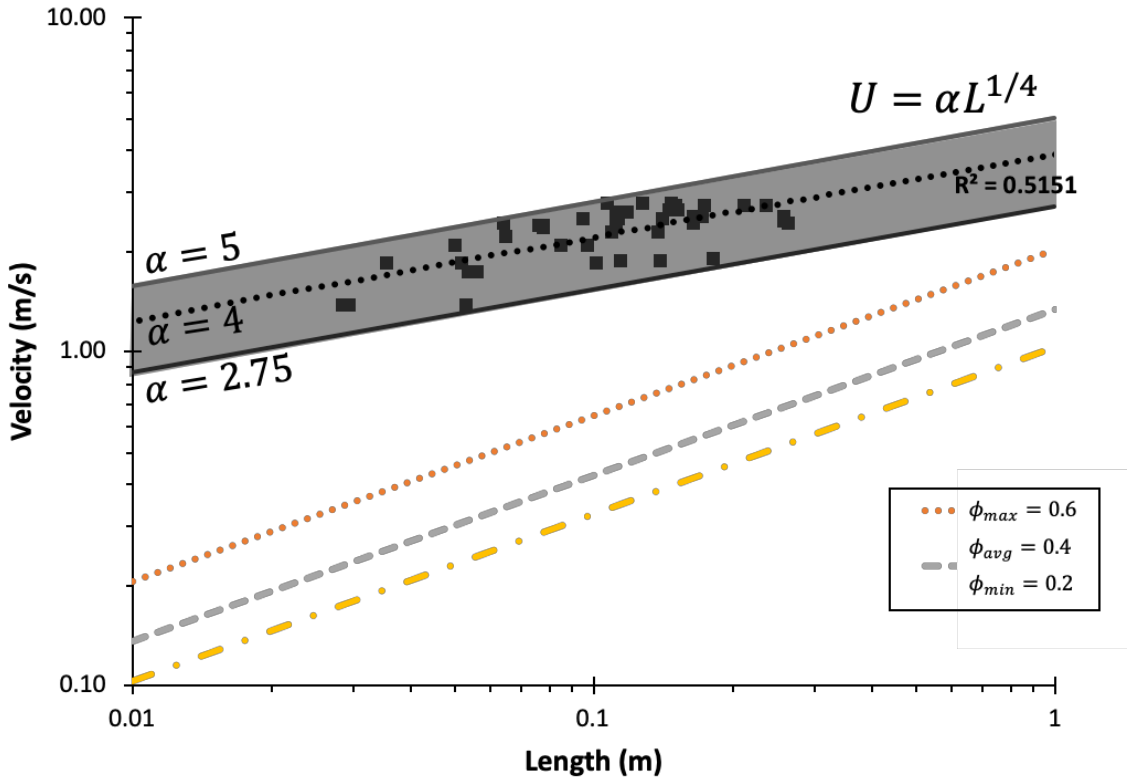

Figure 4.9 Gray squares indicate length of mixing structures measured following deposition for flows of a given velocity. A moderate correlation exists between the measured structure length and flow velocity. Colored lines show the necessary flow velocity to produce instabilities of a given length calculated from the instability growth criterion for Kelvin-Helmholtz instabilities. The different colors indicate different possible solid volume fractions expected in our experimental flows. Because all the experimental velocity measurements are above the theoretical velocities necessary to generate instabilities, the mixing observed in our experiments could be due to the formation of granular shear instabilities that are akin to Kelvin-Helmholtz instabilities. Additionally, the best fit line for the experimental data shows that the flow front velocity is proportional to $\alpha L^{1/4}$, where α is an experimentally derived constant that is equal to 4 for the best fit line, but ranges from 2.75 to 5 to capture the entire dataset.

Figure 4.9 shows the predicted wavelength for flows of a given velocity and solid volume fraction (colored lines showing ϕ_1 = 0.6, 0.4, and 0.2). The flow velocities necessary to generate instabilities on the scale of those generated in the experiments (0.03-0.26 m) are all less than the velocities achieved by out experimental flows. The lengths of structures preserved in the deposits and the associated flow velocities are also plotted in Figure 4.9 (dark gray squares). The measured flow velocities for mixing structures of a given length all exceed those necessary to generate instabilities.

Given that (1) the correlation of structure length with flow velocity and bed roughness, (2) the calculated gradient Richardson numbers suggest shear on the flow-bed interface is sufficient to initiate mixing, and (3) the instability growth criterion predicts the formation of instabilities for the flow velocities measured in our experiments and the expected solid volume fractions, we confirm the hypothesis that shear is responsible for the formation of the mixing structures observed in our experiments. Farthermore, we interpret the mixing observed in our experiments to result from granular shear instabilities formed at the flow bed interface, as Rowley et al. (2011) and Farin et al. (2014) do for their experiments. We discuss below the assumptions and limitations to our interpretations.

Relationships between structure morphology and flow parameters

Our experiments demonstrate that relationships exist between the morphology of the mixing structures and measurable flow parameters, including a correlation between structure length and flow velocity and between structure height and flow height. These relationships provide the potential to extract quantitative information about flow conditions based solely on measurements of mixing structure morphology, and thus can be applied to natural deposits. We follow the approach of numerous, similar studies that investigate the

relationships between the morphology of sedimentary features, such as dunes, ripples, and flute marks, and flow parameters, such as velocity, depth, and grain size (e.g. Yalin 1964; Allen 1968; Allen 1984; Komar 1985; Garcia 2008; Som et al. 2012).

Structure length and flow velocity

We observe a moderate correlation between the length of mixing structures preserved in the deposits and the flow front velocity (R^2 = 0.52; Figure 4.9). The relationship between the structure length (L) and flow velocity (U) is best described by a power law, such that $U = \alpha L^{\frac{1}{4}}$, where α is a constant that is determined from the experimental data. The best fit line is defined for α=4 but allowing α to vary between 2.75 and 5 captures the entire data set (Figure 4.9). Despite the scatter, using the entire range of α to describe the relationship between length and flow velocity provides a more conservative approach that leads to a range of velocity estimates for a given structure length that varies by a factor of 1.8.

One additional approach to constraining flow velocity using the measured structure length is via the Kelvin-Helmholtz instability growth criterion, as mentioned above. Using this predictive relationship, the measured length provides a lower bound on the flow velocity necessary to initiate the growth of instabilities on the flow-bed interface. According to the instability growth criterion, the flow velocities measured in our experiments all fall above the necessary velocity to initiate instabilities of the length observed in the experiments (Figure 4.9). However, using the instability growth criterion alone underpredicts the flow velocity by a factor of 2-4.

Structure height and flow height

The relationship between structure height and flow height changes depending the stage of the mixing evolution; during onset and growth, the structure height (*H*) is moderately well correlated with flow height (*h*), but upon deposition there is essentially no correlation between structure height and the deposit height (Figure 4.5a-4.5c). However, almost all of the change in structure height occurs between the onset and growth phases, and a change in height of only 11% occurs between the growth and deposition phases.

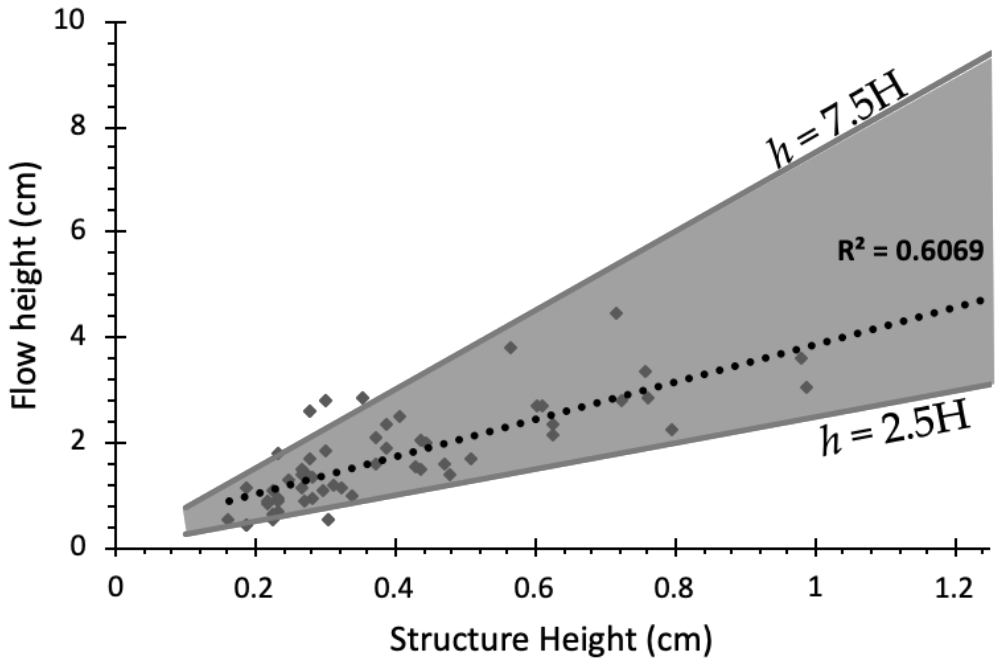

Figure 4.10 Gray diamonds are measured structure heights (H) relative to the flow height (h) overtop of the structure and indicate a moderate correlation between the two heights. The entire data set is bounded by the scaling relationships of h=2.5H and h=7.5H.

We use the height of structures preserved in the deposits to interpret flow conditions during the growth of the structures. Given that only a slight difference exists between the structure height from growth to deposition, we believe the structure heights as preserved

in the deposits can approximate the structure height during their growth. Therefore, the structure height preserved in the deposits are used to estimate the flow height while the structures were growing. For over 95% of our measurements, the flow height during structure growth is between 2.5*H* and 7.5*H*, with a mean of 3.5*H* (Figure 4.10).

Implications for pyroclastic currents

Structures similar to those produced at the flow-bed interface in our experiments occur in the deposits of pyroclastic currents (Rowley 2010; Rowley et al. 2011; Douillet et al. 2018; Pollock et al., 2019), tsunamis (Matsumoto et al. 2008), and turbidity currents (Dasgupta 1998). These structures are termed many things in the literature including vortical reworking features (Rowley et al. 2011), sheared wavelike structure (Roche et al. 2013), "shark fin" structures (Douillet et al. 2018), and sheared, recumbent, or truncated flame structures (e.g. Sparks et al. 1985; Matsumoto et al. 2008; Rowley 2010; Pollock et al. 2019). While there may be applications of our results to the deposits of tsunamis and turbidity currents, we focus our discussion on the mixing structures found in pyroclastic current deposits because that is the system to which our experiments are scaled.

First, we compare the dimensions of recumbent flame structures observed in the pyroclastic current deposits from the May 18, 1980 eruption at Mount St Helens (Brand et al. 2017; Pollock et al. 2019) to the mixing structures produced in our experiments. The structures found in the Mount St Helens deposits vary in size over two orders of magnitude, from a few centimeters to almost 20 meters in length, and the height of the structures is well correlated to the length (Pollock et al. 2019). When plotted together, the height and length of the recumbent flame structures and experimental mixing structures are extremely well correlated despite a variation of almost 5 orders of magnitude (R^2=0.96; Figure 4.11).

This observation suggests that both the field and experimental structures are produced by granular shear instabilities formed at the flow-bed interface (Rowley et al. 2011; Farin et al. 2014; Pollock et al., 2019).

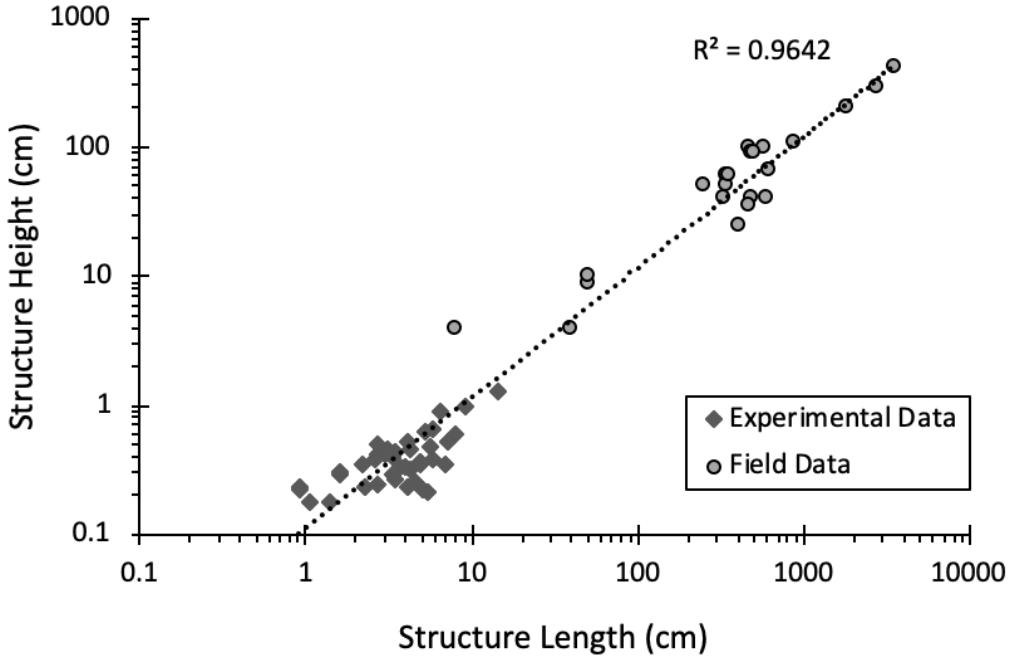

Figure 4.11 Structure length versus structure height plotted for our experimental data (gray diamonds) and field data from recumbent flame structures measured in the deposits of pyroclastic currents produced during the May 18, 1980 eruption of Mount St Helens (gray circles; data from Pollock et al. 2019). Strong correlation for the height versus length for both the experimental and field data suggesting the structures are all formed by the same process of granular shear instabilities generating mixing at the flow-bed interface.

Additionally, we use the relationships between structure dimensions and flow parameters derived from the experiments to estimate conditions in the pyroclastic currents at the time the recumbent flame structures formed. Previous studies estimated the flow velocity using the length of flame structures and the instability growth criterion although the velocity estimates were limited to a minimum velocity necessary to initiate the formation of instabilities (Pollock et al. 2019). Here we use the relationship $U = \alpha L^{\frac{1}{4}}$,

where $\alpha = 4$, to estimate the flow velocity necessary to produce structures of a given length. The longest recumbent flame structure observed in the deposits is 17.9 m long, and this relationship predicts a flow velocity of 8.2 $m \cdot s^{-1}$ at the time the structure was forming. The shortest flame structures are only 4-5 cm long; for these structures, the relationship predicts flow velocities of 3.1-3.3 $m \cdot s^{-1}$.

Previous studies use the modified instability growth criterion to estimate flow velocity based on the length of these same structures and assumptions about the relative densities of the flow and the bed (Pollock et al. 2019). The flow velocity estimates using the relationships derived from the experiments are all greater than those determined using the instability growth criterion. For example, the largest structure gives a velocity estimate of 2.9 – 7.5 $m \cdot s^{-1}$ versus 8.2 $m \cdot s^{-1}$ using the experimental relationship, and similarly the smallest structures produce velocity estimates of 0.2 – 0.5 $m \cdot s^{-1}$ and 3.2 $m \cdot s^{-1}$ for the instability growth criterion and experimental relationship, respectively.

There are two possible reasons for the greater velocities predicted by the experimental relationship. First, the experimental scaling relationship is based on the flow front velocity; whereas, the instability growth criterion may be predicting the shear velocity on the interface (Pollock et al. 2019), which our experimental data shows would be at most 60% of the flow front velocity (Figure 4.7). The second possible reason is that the instability growth criterion provides only a minimum flow velocity, but the experimental relationship is based on a best fit of the relationship between flow front velocity and structure length, which when applied to natural structures would produce an average velocity estimate.

While the lack of visual observations limits our ability to constrain the flow velocities for pyroclastic currents produced during the May 18, 1980 eruption at Mount St Helens, the velocity estimates for the longer structures (5-8 m·s-1; Table 1) compare favorably to flow velocities measured for a smaller pyroclastic current produced on August 7, 1980 at Mount St Helens (Hoblitt 1986; Levine and Kieffer 1991). Visual observations made at a distance of ~3 km from the vent and near the end of the pyroclastic current's runout estimate flow velocities of 5.4-9.7 $m \cdot s^{-1}$ (Hoblitt 1986; Levine and Kieffer 1991). While the August 7 current was smaller in volume and shorter in runout than the pyroclastic currents produced on May 18 (Rowley et al. 1981; Hoblitt 1986), the observed flow velocities demonstrate that our approach of using the mixing structure length to estimate flow velocity produces velocities that are reasonable for the May 18, 1980 Mount St Helens pyroclastic currents.

Finally, we use the relationships derived from the experiments to estimate the flow height at the time the Mount St Helens structures formed. The tallest structures observed in the field is 2 m tall, which suggests flow thicknesses between 5 and 15 m, while the shortest structures, only 4 cm tall, suggest flow thicknesses of 10-30 cm. These thickness estimates correspond to the thickness of the dense basal layer that sits at the interior of the pyroclastic current, and are reasonable given our current understanding of pyroclastic currents (Sulpizio et al. 2014). Based on the morphology of sedimentary structures, the dense, basal region of the current likely retains elevated pore fluid pressures and remains in a highly concentrated but also highly mobile state until final deposition occurs (i.e. Pollock et al., 2019).

Assumptions and future outlook

Our interpretation that the mixing structures formed due to granular shear instabilities implies that both the flow and the bed behave in a fluid-like fashion, promoting mixing across the interface. Our argument for this interpretation assumes that the mixing processes can be approximated with relationships that describe mixing between two pure fluids, including the gradient Richardson number and instability growth criterion for Kelvin-Helmholtz instabilities. Our experiments suggest that this assumption holds true as long as pore fluid pressure in the flow remains elevated, but the assumption of fluid-like properties is not true for the entire duration of flow propagation.

Fine-grained granular flows retain elevated pore fluid pressures over significant portions of their runout distance (Roche et al. 2008; Roche et al. 2010; Roche 2012), and while pore fluid pressures remain elevated, these flows share much of their behavior with inertial flows of water (Roche et al. 2008). If the large-scale kinematics of fluidized granular flows resemble those of pure fluids more closely than those of dry granular flows, as Roche et al. (2008) observe, it is possible that, as long as pore fluid pressures remain elevated, the mixing processes between fluidized granular flows and the bed would also share similarities with mixing processes in pure fluids. However, once the internal gas diffuses out of the flow and pore pressures become equal or nearly equal to the ambient, the flows behave like dry granular flows (Roche et al. 2008). Dry granular flows have a shear strength and can deposit on steep slopes that approach the angle of repose for the material (Cas and Wright 1988; Cagnoli and Manga 2004), and likely would not mix in the same fashion as pure fluids nor would the mixing process be governed by the same relationships as pure fluids. Because we observe mixing during the constant velocity phase,

a phase during which elevated pore fluids pressures are still present (Roche et al. 2010), we assume that the mixing occurs while the flow has fluid-like properties. Additionally, Pollock (Chapter 2) suggests that gas may diffuse down into a porous bed, which may aid in the uplift of bed material as mixing structures.

Additionally, while the scaling relationships derived for subaqueous bedforms accurately relate the morphology of the structures to flow conditions for the majority of flow conditions, we acknowledge that disagreement exists as to the applicability of the scaling relationships under some flow conditions (cf. Bradley and Venditti 2017). However, to our knowledge, our study represents the first attempt to describe scaling relationships for structures produced in gas-particle flows, and our results demonstrate that our approach provides a starting point from which future studies can farther constrain the relationships between structure morphology and flow parameters. Additionally, the sparsity of methods for extracting quantitative flow parameters from the characteristics of pyroclastic current deposits makes the types of constraints presented here essential as they could produce a dataset that would help test numerical models. Our results suggest that the approach presented here utilizing simple scaling relationships is both sufficiently conservative and informative to be useful in extracting quantitative information from the deposits of natural gas-particle flows.

Conclusions

Here we present the results of analogue laboratory experiments that investigate the interactions that occur at the flow-bed interface of fluidized granular flow and an initially static dry, granular bed. Regardless of the bed angle or the size of particles in the bed, mixing occurs between the flow and the bed in all experimental configurations, generating

wave-like mixing structures that propagate at the base of the flow. The evolution of the mixing structures is divided into three phases: onset, growth, and deposition. The length and height of the mixing structures scales with increasing flow velocity and increasing bed grain size. The ratio of the structure height and length is consistent during the onset and growth phases (Figure 4.5a and 4.5b), but upon deposition, the structures become elongated due to continuous deformation during deposition.

We demonstrate that the physical dimensions of the structures formed from deformation and mixing of a granular bed correlate with flow parameters and derive quantitative expressions for the scaling relationships. The structure length provides constraints on the flow velocity and the structure height constrains flow height. Based on calculations of the gradient Richardson number and a modified instability growth criterion, we suggest that the structures formed due to shear exerted on the flow-bed interface. The structures represent the formation of granular shear instabilities that are analogous to Kelvin-Helmholtz instabilities that form in pure fluids.

We demonstrate how the scaling relationships derived from the experiments can be applied to mixing structures preserved in the deposits of pyroclastic currents from the May 18, 1980 eruption of Mount St Helens. The relationships estimate flow velocities of ~ 8 $m \cdot s^{-1}$ for the largest structures and 2-3 $m \cdot s^{-1}$ for the smallest structures. The structures estimate the thickness of the highly-concentrated basal region in the pyroclastic currents to be 5-15 m and 0.1-0.3 m for the largest and smallest structures, respectively. The velocity estimates are slightly larger than the velocity estimates generated from the instability growth criterion, but the velocity estimates from the instability growth criterion are minimum velocities.

This approach shows promise for increasing our ability to extract quantitative information about flow parameters from the deposits of pyroclastic currents. We suggest that additional studies investigating the formation conditions of structures observed in the deposits of pyroclastic currents may continue to increase our capacity to extract this type of data from deposits. These quantitative constraints on the flow conditions of natural pyroclastic currents are essential to our ability to test numerical models, which are increasingly important to hazard and risk assessments. With continued synthesis of field, experimental, and numerical studies, we can farther our understanding of these dangerous volcanic phenomena.

Table 4-1. Measurements of sedimentary structures in the pyroclastic current deposits at Mount St Helens from Pollock et al. (2019) with estimates of flow velocity, flow height and deposition rates from relationships derived from experiments presented here.

Outcrop	Distance from vent (km)	Length (m)	Height (m)	Velocity from Instability Growth Criterion (m/s) from Pollock et al. (2019)	Velocity from Experimental Relation: $U = \alpha L^{\frac{1}{4}}$	Flow Height (m)	Deposition Rate (m/s)
B-2a	5.0	3.3	0.4	1.2-3.2	5.39	1 - 3	0.65
B-2a	5.0	2.5	0.5	1.0-2.8	5.03	1.25 - 3.75	1.01
B-2a	5.0	0.5	0.09	0.5-1.2	3.36	0.23 - 0.67	0.61
B-2a	5.0	0.5	0.1	0.5-1.2	3.36	0.25 - 0.75	0.67
B-2a	5.0	3.4	0.6	1.3-3.3	5.43	1.5 - 4.5	0.96
C-3	5.1	17.9	2.0	2.9-7.5	8.23	5 - 15	0.92
B-3	5.4	0.4	0.04	0.4-1.1	3.18	0.1 - 0.3	0.32
B-3	5.4	0.08	0.04	0.2-0.5	2.13	0.1 - 0.3	1.06
AD-3	5.9	3.4	0.5	1.3-3.3	5.43	1.25 - 3.75	0.80
AD-3	5.9	6	0.4	1.7-4.3	6.26	1 - 3	0.42
AD-3	6.1	3.5	0.6	1.3-3.3	5.47	1.5 - 4.5	0.94

CHAPTER FIVE: CONCLUSIONS

This dissertation research advances our understanding of the fundamental processes that control the behavior of pyroclastic currents. Through the synthesis of field and laboratory techniques, we now better understand the enigmatic processes that occur at the flow-bed interface. These basal processes exert strong control on the overall behavior and runout distance of pyroclastic currents, either increasing or decreasing the distance these dangerous flows can travel depending on the characteristics of the bed. Along with previous studies, this research farther demonstrates that when examining the controls on pyroclastic current behavior, we must consider the effects of erosion, mixing, and pore pressure diffusion processes that occur at the base of pyroclastic currents.

Both the field and laboratory investigations presented in this dissertation show that pyroclastic currents can maintain a fluid-like behavior up until the moments before final deposition. The fluid-like behavior promotes erosion and mixing with the bed. Field observations demonstrate that these mixing processes can be recorded in the deposits of pyroclastic currents as recumbent flame structures, wave-like sedimentary structures that represent the reworking of bed material due to shear exerted by the flow. The morphology of the recumbent flame structures as preserved in the deposits shows that pyroclastic currents maintain a highly concentrated but also highly mobile basal region up until the moments prior to final deposition likely as a result of elevated pore fluid pressure.

Synthesizing the experiments presented here with previous work demonstrates that for flows with elevated pore fluid pressures the characteristics of the bed exert strong

control on the overall flow behavior. When the bed is either impermeable, or thin and erodible, the pore fluid pressure is forced to diffuse upwards through the flow, which leads to extended run-out distances relative to dry granular flows. However, when fluidized flows travel over a bed that is thick and porous, pore fluid pressure can diffuse both up through the flow and also down into the porous bed. The bi-directional diffusion of pore fluid pressure decreases the timescale for pore fluid pressure diffusion, effectively decreasing the runout distance.

Additionally, in the experiments we observed mixing between the flow and the bed in all experimental configuration. Mixing takes the form of periodic wave-like structures generated at the flow bed interface that, once generated, propagate downstream. along with the flow. The dimensions of the mixing structures correlate with flow parameters such as flow velocity and flow thickness. We follow Rowley et al. (2011) and Farin et al. (2014) and interpret that these structures form as a result of granular shear instabilities formed at the flow-bed interface. Granular shear instabilities that form in our fluidized granular flows are akin to Kelvin-Helmholtz instabilities that form in pure fluids. We extract scaling relationships from the experimental data that relate mixing structure morphology to flow parameters; the structure length increases with flow velocity and the structure height increases with flow thickness.

The strength of the approach taken in this dissertation research is that it allows for the application of relationships derived from the experiments to the deposits of natural pyroclastic currents to extract quantitative information about natural flows. We apply the scaling relationships to the recumbent flame structures observed in the deposits of the May 18th 1980 eruption at Mount St Helens. This approach provides quantitative information

about the pyroclastic currents at the time the structures were forming, just prior to deposition. We are able to estimate flow velocities that range from 2.1 $m \cdot s^{-1}$ for the smallest structures and up to 8.2 $m \cdot s^{-1}$ and flow thicknesses that range from tens of centimeters up to 15 meters. Additionally, the flow velocities can be combined with measurements of the structures to constrain deposition rates, suggesting deposition rates up to 1 $m \cdot s^{-1}$. Such high deposition rates require that the deposits did not accumulate progressively over the entire flow duration, but rather accumulated in pulses via stepwise aggradation. The estimates of flow parameters compare favorably to other similar pyroclastic currents, but the lack of visual observations made during the May 18th, 1980 eruption prohibit direct comparison of our estimates to flow parameters from the May 18th pyroclastic currents. However, this also demonstrates the advantage of this technique; quantitative flow parameters can be extracted from the characteristics of the deposits alone.

Future Outlook

The ultimate goal of all research on pyroclastic currents should be to improve our understanding of the processes that control flow behavior so that we can provide the most accurate and reliable risk assessments for these dangerous flows. Most risk assessments involve the use of numerical models to constrain flow mobility and runout, but our lack of in situ measurements for natural pyroclastic current means that aspects of these models are largely untested against natural data. Data sets produced from this dissertation research can be used to directly test and validate the numerical models used in risk assessment for pyroclastic currents. Additionally, similar studies that synthesize field, experimental, and numerical methods have the potential to produce additional data sets that will refine our existing numerical models.

While the research presented here addresses many questions regarding the processes occurring in the basal region of pyroclastic currents, the results of the studies also generate new questions. Future studies could address the following research topics:

1. Here the experiments investigated the effect of an erodible and porous bed on the behavior of granular flows, but future experiments could explore how the presence of a porous but non-erodible bed affects the behavior of granular flows. This approach would allow us to isolate the effects of pore pressure diffusion into a porous bed without the complicating factor of erosion. The results of such a study would also provide insight into how much of the results presented here are due to erosion versus pore pressure diffusion.
2. While the experiments presented here explore the effect of bed characteristics such as slope and bed grain size on flow behavior, future experiments could investigate the effects of additional bed characteristics, including the effects of cohesion or a partially fluidized bed. Both of these characteristics are likely encountered by natural flows when they flow overtop of wet sediment or deposits of recent pyroclastic currents, respectively.
3. The deposits of pyroclastic currents contain a number of complex sedimentary structures that have yet to be studied in detail. Future studies could employ a similar approach to that presented here and synthesize experimental and field techniques to explore the formation of those sedimentary structures. Such a study provides the promise of finding additional methods to extract quantitative information about flow parameters from the deposits of pyroclastic currents.

Finally, the next major goal in the study of pyroclastic currents must be to obtain in situ measurements of natural flows. Accomplishing this requires instrumenting a valley with sensors capable of measuring important flow parameters such as velocity, solid volume fraction, basal forces including shear, and temperature, while also being able to withstand the harsh conditions inside a pyroclastic current. The resulting data set would allow us to test the numerous models of pyroclastic currents proposed over the last 50 years. The existing models are largely based on observations from deposits and experimental and numerical investigations, but until we have data from natural currents these models will go untested against natural data. To move our field forward, we must obtain a data set that allows us to test our existing models. Well-tested models will ensure that our risk assessments of the dangers posed by pyroclastic currents are as accurate as possible, which is the ultimate goal of our field.

REFERENCES

Albert MR, Perron FE (2000) Ice layer and surface crust permeability in a seasonal snow pack. Hydrol Process 14:3207–3214. doi: 10.1002/1099-1085(20001230)14:18<3207::AID-HYP196>3.0.CO;2-C

Allen JRL (1976) Bed forms and unsteady processes: Some concepts of classification and response illustrated by common one-way types. Earth Surf Process 1:361–374. doi: 10.1002/esp.3290010405

Allen JRL (1984) Sedimentary Structures: Their Character and Physical Basis, Volumes I and II. El Sevier, Amsterdam

Allen JRL (1968) Flute marks and flute separation. Nature 219:602–604

Allen JRL (1985) Principles of Physical Sedimentology. Springer Netherlands

Andrews BJ (2014) Dispersal and air entrainment in unconfined dilute pyroclastic density currents. Bull Volcanol 76:1–14. doi: 10.1007/s00445-014-0852-4

Andrews BJ (2019) Recognizing unsteadiness in the transport systems of dilute pyroclastic density currents. Bull Volcanol 81:. doi: 10.1007/s00445-018-1266-5

Andrews BJ, Manga M (2012) Experimental study of turbulence, sedimentation, and coignimbrite mass partitioning in dilute pyroclastic density currents. J Volcanol Geotherm Res 225–226:30–44. doi: 10.1016/j.jvolgeores.2012.02.011

Bartholdy J, Ernstsen VB, Flemming BW, et al (2015) On the formation of current ripples. Sci Rep 5:1–9. doi: 10.1038/srep11390

Benage MC, Dufek J, Mothes PA (2016) Quantifying entrainment in pyroclastic density currents from the Tungurahua eruption, Ecuador: Integrating field proxies with numerical simulations. Geophys Res Lett 43:6932–6941. doi: 10.1002/2016GL069527

Bernard J, Kelfoun K, Pennec J-L Le, et al (2014) Pyroclastic flow erosion and bulking processes: comparing field-based vs. modeling results at Tungurahua volcano, Ecuador. Bull Volcanol 76:1–16. doi: 10.1007/s00445-014-0858-y

Boano F, Revelli R, Ridolfi L (2007) Bedform-induced hyporheic exchange with unsteady flows. Adv Water Resour 30:148–156. doi: 10.1016/j.advwatres.2006.03.004

Bradley RW, Venditti JG (2017) Reevaluating dune scaling relations. Earth-Science Rev 165:356–376. doi: 10.1016/j.earscirev.2016.11.004

Bradley RW, Venditti JG (2019) Transport Scaling of Dune Dimensions in Shallow Flows. J Geophys Res Earth Surf 124:526–547. doi: 10.1029/2018JF004832

Brand BD, Bendaña S, Self S, Pollock N (2016) Topographic controls on pyroclastic density current dynamics: Insight from 18 may 1980 deposits at Mount St. Helens, Washington (USA). J Volcanol Geotherm Res 321:1–17. doi: 10.1016/j.jvolgeores.2016.04.018

Brand BD, Gravley DM, Clarke AB, et al (2014a) A combined field and numerical approach to understanding dilute pyroclastic density current dynamics and hazard potential: Auckland Volcanic Field, New Zealand. J Volcanol Geotherm Res 276:215–232. doi: 10.1016/j.jvolgeores.2014.01.008

Brand BD, Mackaman-Lofland C, Pollock NM, et al (2014b) Dynamics of pyroclastic density currents: Conditions that promote substrate erosion and self-channelization - Mount St Helens, Washington (USA). J Volcanol Geotherm Res 276:189–214. doi: 10.1016/j.jvolgeores.2014.01.007

Brand BD, Pollock NM, Sarocchi D, et al (2017) Field-trip guide for exploring pyroclastic density current deposits from the May 18, 1980, eruption of Mount St. Helens, Washington. USGS Sci Investig Rep 2017-5022-C

Branney MJ, Kokelaar BP (2002) Pyroclastic Density Currents and the Sedimentation of Ignimbrites, Issue 27. Geological Society of London

Branney MJ, Kokelaar P (1992) A reappraisal of ignimbrite emplacement: progressive aggradation and changes from particulate to non-particulate flow during

emplacement of a high-grade ignimbrite. Bull Volcanol 54:504–520

Breard ECP, Dufek J, Lube G (2018) Enhanced Mobility in Concentrated Pyroclastic Density Currents: An Examination of a Self-Fluidization Mechanism. Geophys Res Lett 45:654–664. doi: 10.1002/2017GL075759

Breard ECP, Jones JR, Fullard L, et al (2019) The Permeability of Volcanic Mixtures-Implications for Pyroclastic Currents. J Geophys Res Solid Earth. doi: 10.1029/2018JB016544

Breard ECP, Lube G (2017) Inside pyroclastic density currents – uncovering the enigmatic flow structure and transport behaviour in large-scale experiments. Earth Planet Sci Lett 458:22–36. doi: 10.1016/j.epsl.2016.10.016

Bridge JS, Best JL (1988) Flow, sediment transport and bedform dynamics over the transition from dunes to upper-stage plane beds: implications for the formation of planar laminae. Sedimentology 35:753–763. doi: 10.1111/j.1365-3091.1988.tb01249.x

Bristow CS, Balley SD, Lancaster N (2000) The sedimentary structure of linear sand dunes. Nature 406:56–59. doi: 10.1038/35017536

Buesch DC (1992) Incorporation and redistribution of locally derived lithic fragments within a pyroclastic flow. Geol Soc Am Bull 104:1193–1207. doi: 10.1130/0016-7606(1992)104<1193:IAROLD>2.3.CO;2

Burgisser A, Bergantz GW (2002) Reconciling pyroclastic flow and surge: the multiphase physics of pyroclastic density currents. Earth Planet Sci Lett 202:405–418

Cagnoli B, Manga M (2004) Granular mass flows and Coulomb's friction in shear cell experiments: Implications for geophysical flows. J Geophys Res 109:F04005. doi: 10.1029/2004JF000177

Calder ES, Sparks RSJ, Gardeweg MC (2000) Erosion, transport and segregation of pumice and lithic clasts in pyroclastic flows inferred from ignimbrite at Lascar Volcano, Chile. J Volcanol Geotherm Res 104:201–235. doi: 10.1016/S0377-0273(00)00207-9

Carey SN (1991) Transport and deposition of tephra by pyroclastic flows and surges. In: Fisher R V, Smith GA (eds) Sedimentation in Volcanic Settings. SEPM Special Publication, pp 39–57

Cas RAF, Wright HMN, Folkes CB, et al (2011) The flow dynamics of an extremely large volume pyroclastic flow, the 2.08-Ma Cerro Gal{á}n Ignimbrite, NW Argentina, and comparison with other flow types. Bull Volcanol 73:1583–1609. doi: 10.1007/s00445-011-0564-y

Cas RAF, Wright J V. (1988) Volcanic Successions. Chapman & Hall, New York City

Charbonnier SJ, Gertisser R (2011) Deposit architecture and dynamics of the 2006 block-and-ash flows of Merapi Volcano, Java, Indonesia. Sedimentology 58:1573–1612. doi: 10.1111/j.1365-3091.2011.01226.x

Chédeville C, Roche O (2014) Journal of Geophysical Research : Solid Earth. 1764–1776. doi: 10.1002/2013JB010554.Received

Chédeville C, Roche O (2015) Influence of slope angle on pore pressure generation and kinematics of pyroclastic flows : insights from laboratory experiments. 1–13. doi: 10.1007/s00445-015-0981-4

Chiarella D, Moretti M, Longhitano SG, Muto F (2016) Deformed cross-stratified deposits in the Early Pleistocene tidally-dominated Catanzaro strait-fill succession, Calabrian Arc (Southern Italy): Triggering mechanisms and environmental significance. Sediment Geol 344:277–289. doi: 10.1016/j.sedgeo.2016.05.003

Christiansen R, Peterson D (1981) Chronology of the 1980 eruptive activity. In: Lipman P, Mullineaux D (eds) The 1980 eruptions of Mount St Helens, Washington. U.S. Geological Survey Professional Paper 1250, pp 17–30

Ciamarra MP, Coniglio A, Nicodemi M (2005) Shear instabilities in granular mixtures. Phys Rev Lett 94:1–4. doi: 10.1103/PhysRevLett.94.188001

Clarke AB, Voight B (2000) Pyroclastic current dynamic pressure from aerodynamics of tree or pole blow-down. J Volcanol Geotherm Res 100:395–412. doi: 10.1016/S0377-0273(00)00148-7

Clifford NJ, Robert A, Richards KS (1992) Estimation of flow resistance in gravel-bedded rivers: A physical explanation of the multiplier of roughness length. Earth Surf Process Landforms 17:111–126. doi: 10.1002/esp.3290170202

Colbeck SC, Anderson EA (1982) The permeability of a melting snow cover. Water Resour Res 18:904–908. doi: 10.1029/WR018i004p00904

Cole PD, Calder ES, Druitt TH, et al (1998) Pyroclastic flows generated by gravitational instability of the 1996–97 Lava Dome of Soufriere Hills Volcano, Montserrat. Geophys Res Lett 25:3425–3428. doi: 10.1029/98GL01510

Collinson J (1994) Sedimentary deformational structures. In: Maltman A (ed) The Geological Deformation of Sediments. Chapman & Hall, London, pp 95–125

Collinson JD, Thompson DB (1989) Sedimentary Structures. Unwin Hyman, London

Criswell CW (1987) Chronology and pyroclastic stratigraphy of the May 18, 1980, eruption of Mount St. Helens, Washington. J Geophys Res Solid Earth 92:10237–10266. doi: 10.1029/JB092iB10p10237

Dartevelle S (2004) Numerical modeling of geophysical granular flows: 1. A comprehensive approach to granular rheologies and geophysical multiphase flows. Geochemistry, Geophys Geosystems 5:. doi: 10.1029/2003GC000636

Dasgupta P (1998) Recumbent flame structures in the Lower Gondwana rocks of the Jharia Basin, India — a plausible origin. Sediment Geol 119:253–261. doi: 10.1016/S0037-0738(98)00058-X

Davies TR (1990) Debris-flow surges - Experimental simulation. J Hydrol 29:18–46

De Vita S, Orsi G, Civetta L, et al (1999) The Agnano-Monte Spina eruption (4100 years BP) in the restless Campi Flegrei caldera (Italy). J Volcanol Geotherm Res 91:269–301. doi: 10.1016/S0377-0273(99)00039-6

Delannay R, Valance A, Mangeney A, et al (2015) Granular and particle-laden flows: from laboratory experiments to field observations. J Phys D Appl Phys. doi: 10.13140/RG.2.1.3718.8325

Dellino P, La Volpe L (2000) Structures and grain size distribution in surge deposits as a

tool for modelling the dynamics of dilute pyroclastic density currents at La Fossa di Vulcano (Aeolian Islands, Italy). J Volcanol Geotherm Res 96:57–78. doi: 10.1016/S0377-0273(99)00140-7

Douillet GA, Kueppers U, Mato C, et al (2018) Revisiting the lacquer peels method with pyroclastic deposits: Sediment plates, a precise, fine scale imaging method and powerful outreach tool. J Appl Volcanol 7:. doi: 10.1186/s13617-018-0080-2

Douillet GA, Taisne B, Tsang-Hin-Sun, et al (2015) Syn-eruptive, soft-sediment deformation of deposits from dilute pyroclastic density current: Triggers from granular shear, dynamic pore pressure, ballistic impacts and shock waves. Solid Earth 6:553–572. doi: 10.5194/se-6-553-2015

Druitt TH, Avard G, Bruni G, et al (2007) Gas retention in fine-grained pyroclastic flow materials at high temperatures. Bull Volcanol 69:881–901. doi: 10.1007/s00445-007-0116-7

Druitt TH, Calder ES, Cole PD, et al (2002) Small-volume, highly mobile pyroclastic flows formed by rapid sedimentation from pyroclastic surges at Soufrière Hills Volcano, Montserrat: an important volcanic hazard. Geol Soc London, Mem 21:263–279. doi: 10.1144/gsl.mem.2002.021.01.12

Dufek J (2016) The Fluid Mechanics of Pyroclastic Density Currents. Annu Rev Fluid Mech 48:459–485. doi: 10.1146/annurev-fluid-122414-034252

Dufek J, Bergantz GW (2007a) Suspended load and bed-load transport of particle-laden gravity currents: the role of particle–bed interaction. Theor Comput Fluid Dyn 21:119–145. doi: 10.1007/s00162-007-0041-6

Dufek J, Bergantz GW (2007b) Dynamics and deposits generated by the Kos Plateau Tuff eruption: Controls of basal particle loss on pyroclastic flow transport. Geochemistry, Geophys Geosystems 8:. doi: 10.1029/2007GC001741

Dufek J, Esposti Ongaro T, Roche O (2015) Pyroclastic density currents: Processes and models. In: The encyclopedia of volcanoes. pp 631–648

Dullien F AL (1992) Porous media: fluid transport and pore structure. Academic Press

Esposti Ongaro T, Clarke AB, Voight B, et al (2012) Multiphase flow dynamics of pyroclastic density currents during the May 18, 1980 lateral blast of Mount St. Helens. J Geophys Res Solid Earth 117:1–22. doi: 10.1029/2011JB009081

Esposti Ongaro T, Neri A, Todesco M, Macedonio G (2002) Pyroclastic flow hazard assessment at Vesuvius (Italy) by using numerical modelling. II. Analysis of flow variables. Bull Volcanol 64:178–191. doi: 10.1007/s00445-001-0190-1

Farin M, Mangeney A, Roche O (2014) Fundamental changes of granular flow dynamics, deposition, and erosion processes at high slope angles: Insights from laboratory experiments. J Geophys Res Earth Surf 119:504–532. doi: 10.1002/2013JF002750

Fauria KE, Manga M, Chamberlain M (2016) Effect of particle entrainment on the runout of pyroclastic density currents. J Geophys Res Solid Earth 1–17. doi: 10.1002/2016JB013263.Received

Felix M, Peakall J (2006) Transformation of debris flows into turbidity currents: mechanisms inferred from laboratory experiments. Sedimentology 53:107–123. doi: 10.1111/j.1365-3091.2005.00757.x

Fisher R V (1966) Mechanism of deposition from pyroclastic flows. Am J Sci 264:350–366

Flemming B (1988) Zur Klassifikation subaquatischer, stromungstrans versaler Transportkorper. Boch geol u geotechn 29:44–57

Forchheimer P (1914) Hydraulik. Teubner, Leipzig-Berlin

Garcia MH (2008) Sedimentation Engineering Processes, Measurements, Modelling and Practice. American Society of Civil Engineering, Reston, VA

Gase A, Bradford JH, Brand BD (2018) Estimation of porosity and water saturation in dual porosity pyroclastic deposits from joint analysis of compression, shear, and electromagnetic velocities. Geophysics 83:. doi: DOI: 10.1190/geo2017-0234.1

Gase AC, Brand BD, Bradford JH (2017) Evidence of erosional self-channelization of pyroclastic density currents revealed by ground-penetrating radar imaging at Mount St. Helens, Washington (USA). Geophys Res Lett 44:2220–2228. doi:

10.1002/2016GL072178

GDR MiDi (2004) On dense granular flows. Eur Phys J E 14:341–365. doi: 10.1140/epje/i2003-10153-0

Giannetti B, Luongo G (1994) Trachyandesite scoria-flow and associated trachyte pyroclastic flow and surge at Roccamonfina Volcano (Roman Region, Italy). J Volcanol Geotherm Res 59:313–334. doi: 10.1016/0377-0273(94)90085-X

Gilbert GK (1914) Transportation of Debris by Running Water. US Geol Surv Prof Pap 86

Girolami L, Druitt TH, Roche O, Khrabrykh Z (2008) Propagation and hindered settling of laboratory ash flows. J Geophys Res 113:B02202. doi: 10.1029/2007JB005074

Girolami L, Roche O, Druitt TH, Corpetti T (2010) Particle velocity fields and depositional processes in laboratory ash flows, with implications for the sedimentation of dense pyroclastic flows. Bull Volcanol 72:747–759. doi: 10.1007/s00445-010-0356-9

GLICKEN H (1996) Rockslide-debris avalanche of May 18, 1980, Mount St. Helens Volcano. Washington U S Geol Surv Open-file Rep 96–677

Goldfarb DJ, Glasser BJ, Shinbrot T (2002) Shear instabilities in granular flows. Nature 415:302–305. doi: 10.1038/415302a

Goren L, Aharonov E, Sparks D, Toussaint R (2010) Pore pressure evolution in deforming granular material: A general formulation and the infinitely stiff approximation. J Geophys Res 115:B09216. doi: 10.1029/2009JB007191

Gueugneau V, Kelfoun K, Druitt T (2019) Investigation of surge-derived pyroclastic flow formation by numerical modelling of the 25 June 1997 dome collapse at Soufrière Hills Volcano, Montserrat. Bull Volcanol 81:25. doi: 10.1007/s00445-019-1284-y

Hoblitt RP (1986) Observations of the Eruptions of July 22 and August 7, 1980 at Mount St. Helens, Washington, No. 1335

Hungr O (2000) Analysis of debris flow surges using the theory of uniformly progressive flow. Earth Surf Process Landforms 495:483–495

Iverson RM (1997) The physics of debris flows. Rev Geophys 35:245. doi: 10.1029/97RG00426

Iverson RM, Reid ME, Logan M, et al (2011) Positive feedback and momentum growth during debris-flow entrainment of wet bed sediment. Nat Geosci 4:116–121. doi: 10.1038/ngeo1040

Kieffer SW, Sturtevant B (1988) Erosional furrows formed during the lateral blast at Mount St. Helens, May 18, 1980. J Geophys Res 93:14793. doi: 10.1029/JB093iB12p14793

Komar PD (1985) The hydraulic interpretation of turbidites from their grain sizes and sedimentary structures. Sedimentology 32:395–407. doi: 10.1111/j.1365-3091.1985.tb00519.x

Kundu PK, Cohen IM (2004) Fluid Mechanics. Elsevier Academic Press, California

Kuntz M, Rowley P, Macleod N (1990) Geologic map of pyroclastic flow and related deposits of the 1980 eruptions of Mount St Helens, Washington: U.S. Geological Survey Miscellaneous Investigations Map I-1950, 1:12,000

Kuntz MA, Rowley PD, Macleod NS, et al (1981) Petrography and particle-size distribution of pyroclastic-flow, ash-cloud, and surge deposits. In: Lipman L, Mullineaux D (eds) The 1980 Eruptions of Mount St. Helens, Washington. U.S. Geological Survey Professional Paper 1250, pp 525–540

LaBerge RD, Giordano G, Cas RAF, Ailleres L (2006) Syn-depositional substrate deformation produced by the shear force of a pyroclastic density current: An example from the Pleistocene ignimbrite at Monte Cimino, northern Lazio, Italy. J Volcanol Geotherm Res 158:307–320. doi: 10.1016/j.jvolgeores.2006.07.003

Lajeunesse E, Mangeney-Castelnau A, Vilotte JP (2004) Spreading of a granular mass on a horizontal plane. Phys Fluids 16:2371–2381. doi: 10.1063/1.1736611

Lapotre MGA, Lamb MP, McElroy B (2017) What sets the size of current ripples? Geology 45:243–246. doi: 10.1130/G38598.1

Levine AH, Kieffer SW (1991) Hydraulics of the August 7, 1980, pyroclastic flow at

Mount St Helens, Washington. Geology 1121–1124

Louge MY, Carroll CS, Turnbull B (2011) Role of pore pressure gradients in sustaining frontal particle entrainment in eruption currents: The case of powder snow avalanches. J Geophys Res Earth Surf 116:1–13. doi: 10.1029/2011JF002065

Lube G, Breard ECP, Cronin SJ, Jones J (2015) Synthesizing large-scale pyroclastic flows: Experimental design, scaling, and first results from PELE. J Geophys Res Solid Earth 1–16. doi: 10.1002/2014JB011666.Received

Lube G, Breard ECP, Jones J, et al (2019) Generation of air lubrication within pyroclastic density currents. Nat Geosci 12:381–386. doi: 10.1038/s41561-019-0338-2

Macorps E, Charbonnier SJ, Varley NR, et al (2018) Stratigraphy, sedimentology and inferred flow dynamics from the July 2015 block-and-ash flow deposits at Volcán de Colima, Mexico. J Volcanol Geotherm Res 349:99–116. doi: 10.1016/j.jvolgeores.2017.09.025

Major JJ, Iverson RM (1999) Debris-flow deposition: Effects of pore-fluid pressure and friction concentrated at flow margins. Bull Geol Soc Am 111:1424–1434. doi: 10.1130/0016-7606(1999)111<1424:DFDEOP>2.3.CO;2

Mangeney A, Roche O, Hungr O, et al (2010) Erosion and mobility in granular collapse over sloping beds. J Geophys Res Earth Surf 115:. doi: 10.1029/2009JF001462

Martinius AW, Gowland S (2011) Tide-influenced fluvial bedforms and tidal bore deposits (Late Jurassic Lourinhã Formation, Lusitanian Basin, Western Portugal). Sedimentology 58:285–324. doi: 10.1111/j.1365-3091.2010.01185.x

Matsumoto D, Naruse H, Fujino S, et al (2008) Truncated flame structures within a deposit of the Indian Ocean Tsunami: Evidence of syn-sedimentary deformation. Sedimentology 55:1559–1570. doi: 10.1111/j.1365-3091.2008.00957.x

McArdell BW, Bartelt P, Kowalski J (2007) Field observations of basal forces and fluid pore pressure in a debris flow. Geophys Res Lett 34:L07406. doi: 10.1029/2006GL029183

McElwaine JN (2005) Rotational flow in gravity current heads. Philos Trans R Soc A

Math Phys Eng Sci 363:1603–1623. doi: 10.1098/rsta.2005.1597

McElwaine JN, Turnbull B (2005) Air pressure data from the Vallée de la Sionne avalanches of 2004. J Geophys Res 110:F03010. doi: 10.1029/2004JF000237

Miles JW (1961) On the stability of heterogenous shear flows. J Fluid Mech 10:496–508

Moldrup P, Yoshikawa S, Olesen T, et al (2014) Air Permeability in Undisturbed Volcanic Ash Soils. Soil Sci Soc Am J 67:32. doi: 10.2136/sssaj2003.3200

Owen G (1996) Experimental soft-sediment deformation: structures formed by the liquefaction of unconsolidated sands and some ancient examples. Sedimentology 43:279–293. doi: 10.1046/j.1365-3091.1996.d01-5.x

Owen G, Moretti M, Alfaro P (2011) Recognising triggers for soft-sediment deformation: Current understanding and future directions. Sediment Geol 235:133–140. doi: 10.1016/j.sedgeo.2010.12.010

Papaevangelou G, Evangelides C, Tzimopoulos C (2010) A new explicit equation for the friction coefficient in the Darcy–Weisbach equation. Proc Tenth Conf Prot Restor Environ PRE10 166:1–7

Pollock NM, Brand BD, Roche O (2016) The controls and consequences of substrate entrainment by pyroclastic density currents at Mount St Helens, Washington (USA). J Volcanol Geotherm Res 325:135–147. doi: 10.1016/j.jvolgeores.2016.06.012

Pollock NM, Brand BD, Rowley PJ, Sarocchi D, Sulpizio R (2019) Inferring pyroclastic current flow conditions using syn-depositional sedimentary structures. Bulletin of Volcanology.

Roche O (2015) Nature and velocity of pyroclastic density currents inferred from models of entrainment of substrate lithic clasts. Earth Planet Sci Lett 418:115–125. doi: 10.1016/j.epsl.2015.03.001

Roche O (2012) Depositional processes and gas pore pressure in pyroclastic flows: An experimental perspective. Bull Volcanol 74:1807–1820. doi: 10.1007/s00445-012-0639-4

Roche O, Buesch DC, Valentine GA (2016) Slow-moving and far-travelled dense

pyroclastic flows during the Peach Spring super-eruption. Nat Commun 7:10890. doi: 10.1038/ncomms10890

Roche O, Gilbertson MA, Phillips JC, Sparks RSJ (2006) The influence of particle size on the flow of initially fluidised powders. Powder Technol 166:167–174. doi: 10.1016/j.powtec.2006.05.010

Roche O, Montserrat S, Niño Y, Tamburrino A (2010) Pore fluid pressure and internal kinematics of gravitational laboratory air-particle flows: Insights into the emplacement dynamics of pyroclastic flows. J Geophys Res Solid Earth 115:1–18. doi: 10.1029/2009JB007133

Roche O, Montserrat S, Niño Y, Tamburrino A (2008) Experimental observations of water-like behavior of initially fluidized, dam break granular flows and their relevance for the propagation of ash-rich pyroclastic flows. J Geophys Res Solid Earth 113:B12203. doi: 10.1029/2008JB005664

Roche O, Niño Y, Mangeney A, et al (2013) Dynamic pore-pressure variations induce substrate erosion by pyroclastic flows. Geology 41:1107–1110. doi: 10.1130/G34668.1

Rodríguez Santalla I, Sánchez García MJ, Montoya Montes I, et al (2009) Internal structure of the aeolian sand dunes of El Fangar spit, Ebro Delta (Tarragona, Spain). Geomorphology 104:238–252. doi: 10.1016/j.geomorph.2008.08.017

Rossano S, Mastrolorenzo G, De Natale G (2004) Numerical simulation of pyroclastic density currents on Campi Flegrei topography: A tool for statistical hazard estimation. J Volcanol Geotherm Res 132:1–14. doi: 10.1016/S0377-0273(03)00384-6

Rowley P, Kuntz M, Macleod N (1981) Pyroclastic-Flow Deposits. In: Lipman P, Mullineaux D (eds). U.S. Geological Survey Professional Paper 1250, pp 489–512

Rowley PJ (2010) Analogue modelling of pyroclastic density current deposition. PhD Thesis 1–291

Rowley PJ, Kokelaar P, Menzies M, Waltham D (2011) Shear-Derived Mixing In Dense Granular Flows. J Sediment Res 81:874–884. doi: 10.2110/jsr.2011.72

Rowley PJ, Roche O, Druitt TH, Cas R (2014) Experimental study of dense pyroclastic density currents using sustained, gas-fluidized granular flows. Bull Volcanol 76:1–13. doi: 10.1007/s00445-014-0855-1

Sarocchi D, Sulpizio R, Macías JL, Saucedo R (2011) The 17 July 1999 block-and-ash flow (BAF) at Colima Volcano: New insights on volcanic granular flows from textural analysis. J Volcanol Geotherm Res 204:40–56. doi: 10.1016/j.jvolgeores.2011.04.013

Savage SB (1998) Analyses of slow high-concentration flows of granular materials. J Fluid Mech 377:S0022112098002936. doi: 10.1017/S0022112098002936

Savage SB (1984) The Mechanics of Rapid Granular Flows. pp 289–366

Savage SB, Iverson RM (2003) Surge dynamics coupled to pore-pressure evolution in debris flows. Debris-Flow Hazards Mitig Mech Predict Assessment, Ed by Rickenmann, D Chen, C-L, Millpress 1:503–514

Scott WE, Hoblitt RP, Torres RC, et al (1996) Pyroclastic flows of the June 15, 1991 climactic eruption of Mount Pinatubo. In: Newhall CG, Punongbayan S. (eds) Fire and Mud: eruptions and lahars of Mount Pinatubo, Philippines. Philippine Institute of Volcanology and Seismology, Quezon City, and University of Washington Press, Seattle, pp 545–570

Shanmugam G (2017) Global case studies of soft-sediment deformation structures (SSDS): Definitions, classifications, advances, origins, and problems. J Palaeogeogr 6:251–320. doi: 10.1016/j.jop.2017.06.004

Sheridan MF (1979) Emplacement of pyroclastic flows: A review. Geol Soc Am Spec Pap 180 125–136

Simon A, Klimetz D (2012) Analysis of Long-term Sediment Loadings from the Upper North Fork Toutle River System, Mount St Helens, Washington. Oxford, MS

Som SM, Catling DC, Harnmeijer JP, et al (2012) Air density 2.7 billion years ago limited to less than twice modern levels by fossil raindrop imprints. Nature 484:359–362. doi: 10.1038/nature10890

Sorby HC (1859) On the structure produced by the currents during the deposition of stratified rocks. Geologist 2:137–147

Southard JB, Boguchwal LA (1990) Bed configuration in steady unidirectional water flows; Part 2, Synthesis of flume data. J Sediment Res 60:658–679. doi: 10.1306/212F9241-2B24-11D7-8648000102C1865D

Sovilla B, Burlando P, Bartelt P (2006) Field experiments and numerical modeling of mass entrainment in snow avalanches. J Geophys Res Earth Surf 111:1–16. doi: 10.1029/2005JF000391

Sovilla B, Sommavilla F, Tomaselli A (2001) Measurements of mass balance in dense snow avalanche events. Ann Glaciol 32:230–236

Sparks RSJ (1976) Grain size variations in ignimbrites and implications for the transport of pyroclastic flows. Sedimentology 23:147–188. doi: 10.1111/j.1365-3091.1976.tb00045.x

Sparks RSJ, Bonnecaze RT, Huppert HE, et al (1993) Sediment-laden gravity currents with reversing buoyancy. Earth Planet Sci Lett 114:243–257. doi: 10.1016/0012-821X(93)90028-8

Sparks RSJ, Francis PW, Hamer RD, et al (1985) Ignimbrites of the Cerro Galan caldera, NW Argentina. J Volcanol Geotherm Res 24:205–248. doi: 10.1016/0377-0273(85)90071-X

Sparks RSJ, Gardeweg MC, Calder ES, Matthews SJ (1997) Erosion by pyroclastic flows on Lascar Volcano, Chile. Bull Volcanol 58:557–565. doi: 10.1007/s004450050162

Sparks RSJ, Wilson L, Hulme G (1978) Theoretical modeling of the generation, movement, and emplacement of pyroclastic flows by column collapse. J Geophys Res 83:1727–1739. doi: 10.1029/JB083iB04p01727

Steinkogler W, Sovilla B, Lehning M (2014) Influence of snow cover properties on avalanche dynamics. Cold Reg Sci Technol 97:121–131. doi: 10.1016/j.coldregions.2013.10.002

Sulpizio R, Dellino P (2008) Chapter 2 Sedimentology, Depositional Mechanisms and

Pulsating Behaviour of Pyroclastic Density Currents. In: Gottsman J, Marti J (eds) Developments in Volcanology. Elsevier, Amsterdam, pp 57–96

Sulpizio R, Dellino P, Doronzo DM, Sarocchi D (2014) Pyroclastic density currents: State of the art and perspectives. J Volcanol Geotherm Res 283:36–65. doi: 10.1016/j.jvolgeores.2014.06.014

Taddeucci J, Palladino DM (2002) Particle size-density relationships in pyroclastic deposits: Inferences for emplacement processes. Bull Volcanol 64:273–284. doi: 10.1007/s00445-002-0205-6

Thibodeaux LJ, Boyle JD (1987) Bedform-generated convective transport in bottom sediment. Nature 325:341–343

Todesco M, Neri A, Esposti Ongaro T, et al (2002) Pyroclastic flow hazard assessment at Vesuvius (Italy) by using numerical modeling. I. Large-scale dynamics. Bull Volcanol 64:155–177. doi: 10.1007/s00445-001-0189-7

Valentine GA (1987) Stratified flow in pyroclastic surges. Bull Volcanol 49:616–630. doi: 10.1007/BF01079967

Valentine GA, Buesch DC, Fisher R V (1989) Basal layered deposits of the Peach Springs Tuff, northwestern Arizona, USA. Bull Volcanol 51:395–414. doi: 10.1007/BF01078808

Valentine GA, Wohletz KH (1989) Numerical Models of Plinian Eruption Columns and Pyroclastic Flows. J Geophys Res 94:1867–1887

Williams H (1957) Glowing avalanche deposits of the Sudbury Basin. Ontario Dep Mines 65th Annu Rep 57–89

Wilson CJN (1980) The role of fluidization in the emplacement of pyroclastic claws: An experimental approach. J Volcanol Geotherm Res 8:231–249. doi: 10.1016/0377-0273(80)90106-7

Wilson CJN, Hildreth W (1997) The Bishop Tuff: New insights from eruptive stratigraphy. J Geol 105:407–440. doi: 10.1086/515937

Wilson CJN, Walker GPL (1982) Ignimbrite depositional facies: the anatomy of a

pyroclastic flow. J Geol Soc London 139:581–592. doi: 10.1144/gsjgs.139.5.0581

Wright J V., Walker GPL (1981) Eruption, transport and deposition of ignimbrite: A case study from Mexico. J Volcanol Geotherm Res 9:111–131. doi: 10.1016/0377-0273(81)90001-9

Yalin MS (1964) Geometrical properties of sand waves. J Hydraul Div ASCE 105–109

APPENDIX A

Experiment Figures

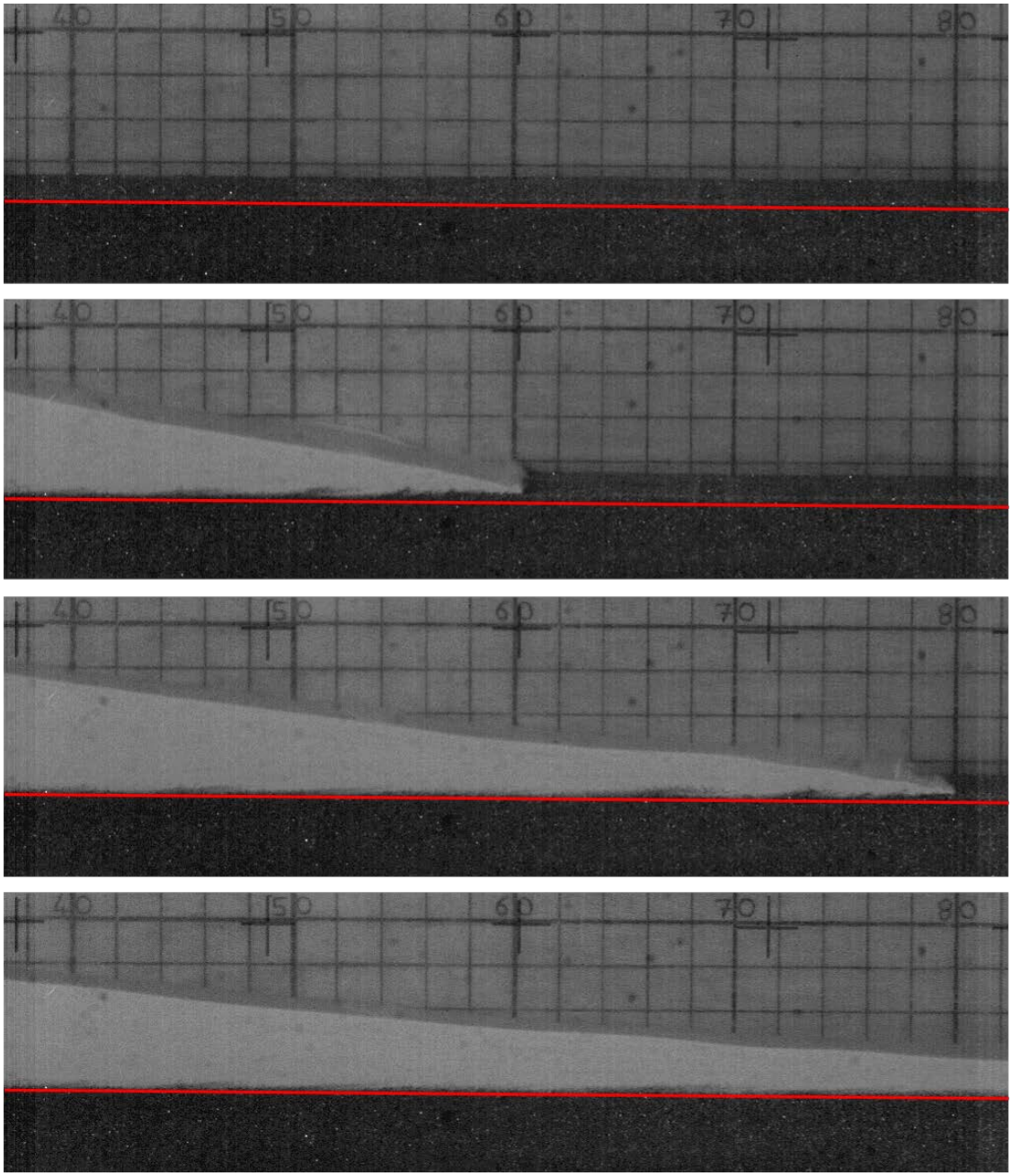

Appendix Figure 1. Experiment R7 - 0 slope, 700 micron bed particles, fluidized.

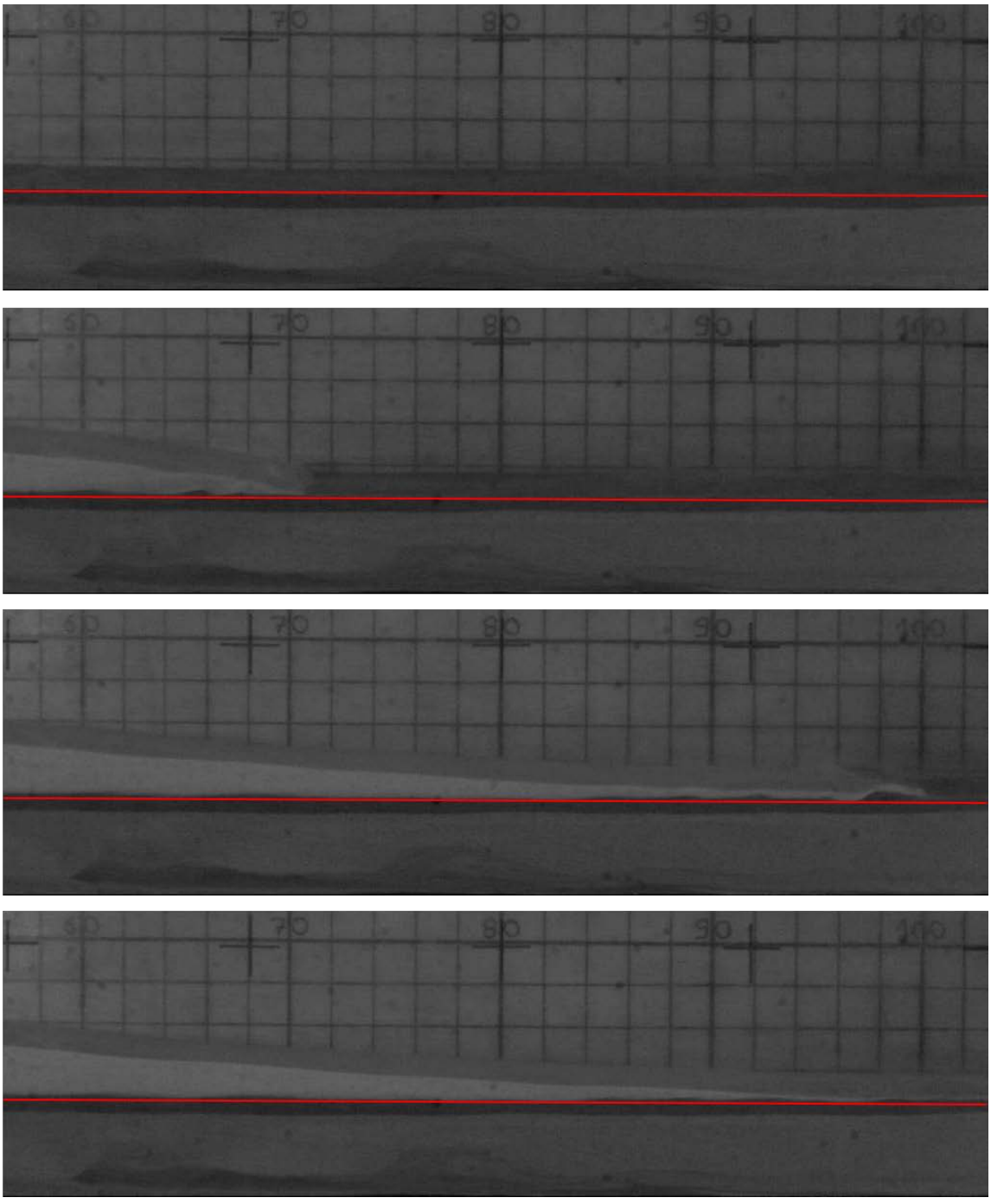

Appendix Figure 2. Experiment R11 - 0 slope, 80 micron bed, fluidized.

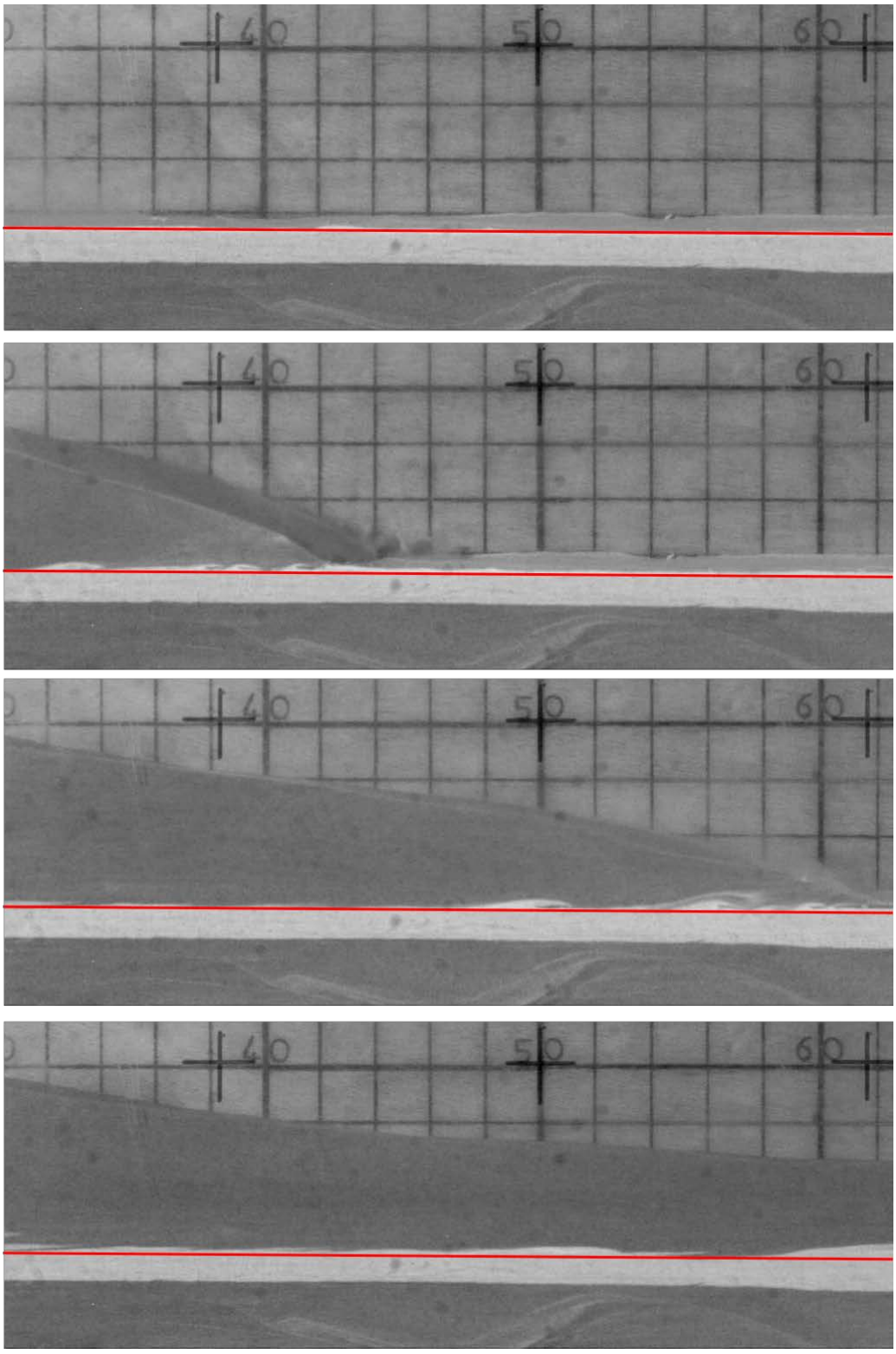

Appendix Figure 3. Experiment R16 - 0 slope, 40 micron bed, fluidized.

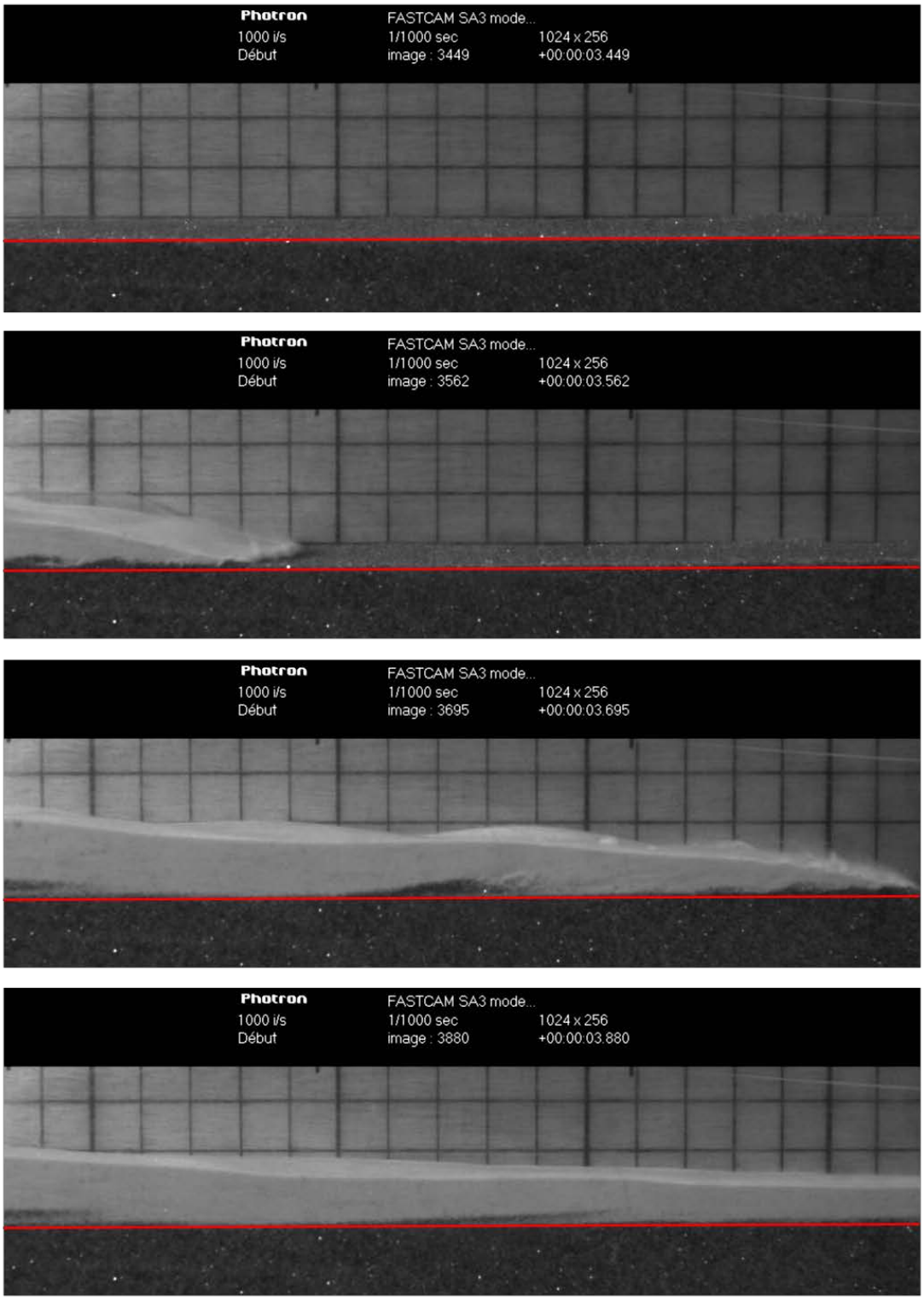

Appendix Figure 4. Experiment R19 - 5 slope, 500 micron bed, fluidized.

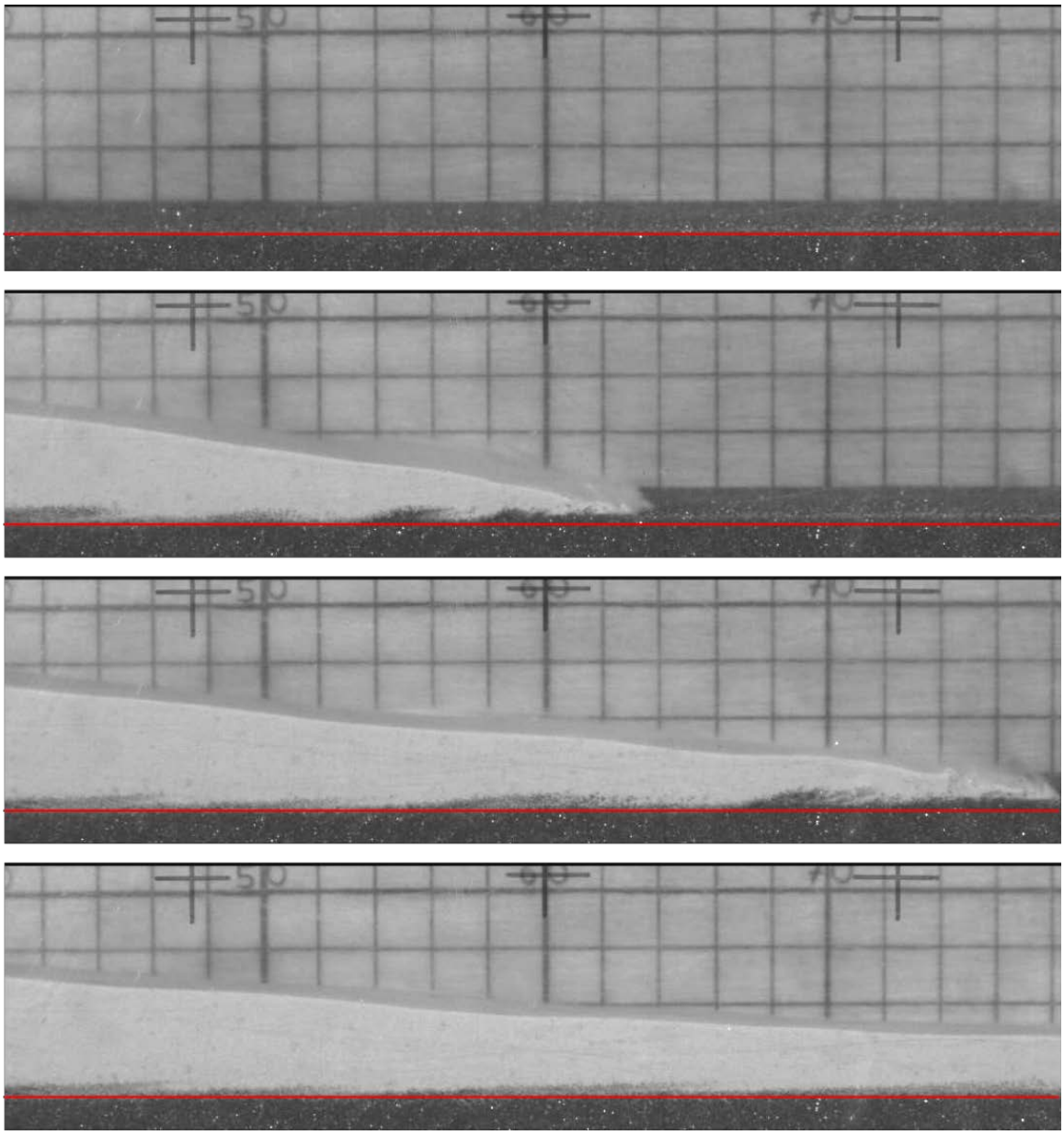

Appendix Figure 5. Experiment R25 - 5 slope, 700 micron bed, fluidized.

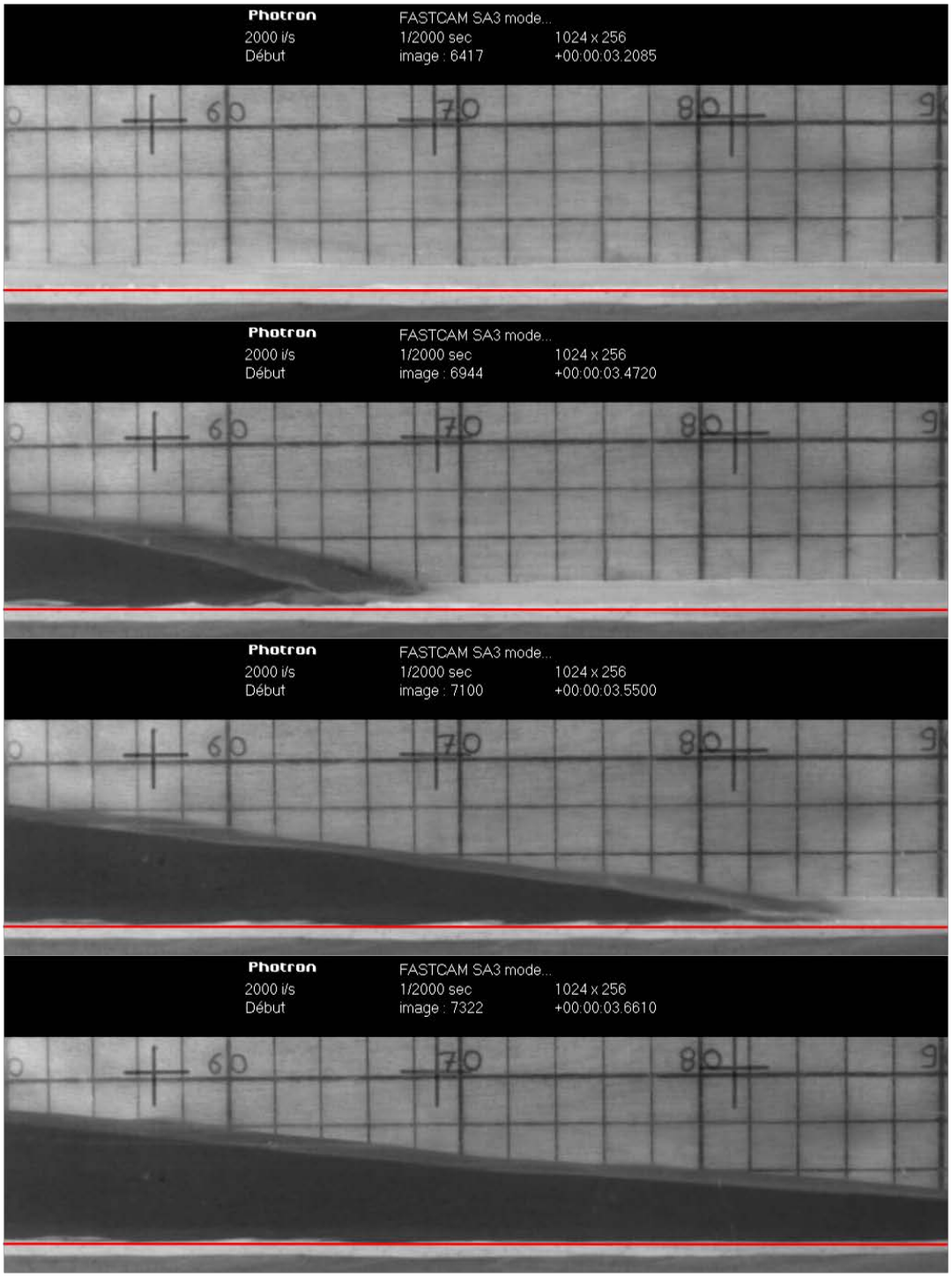

Appendix Figure 6. Experiment R31 – 5 slope, 40 micron bed, fluidized

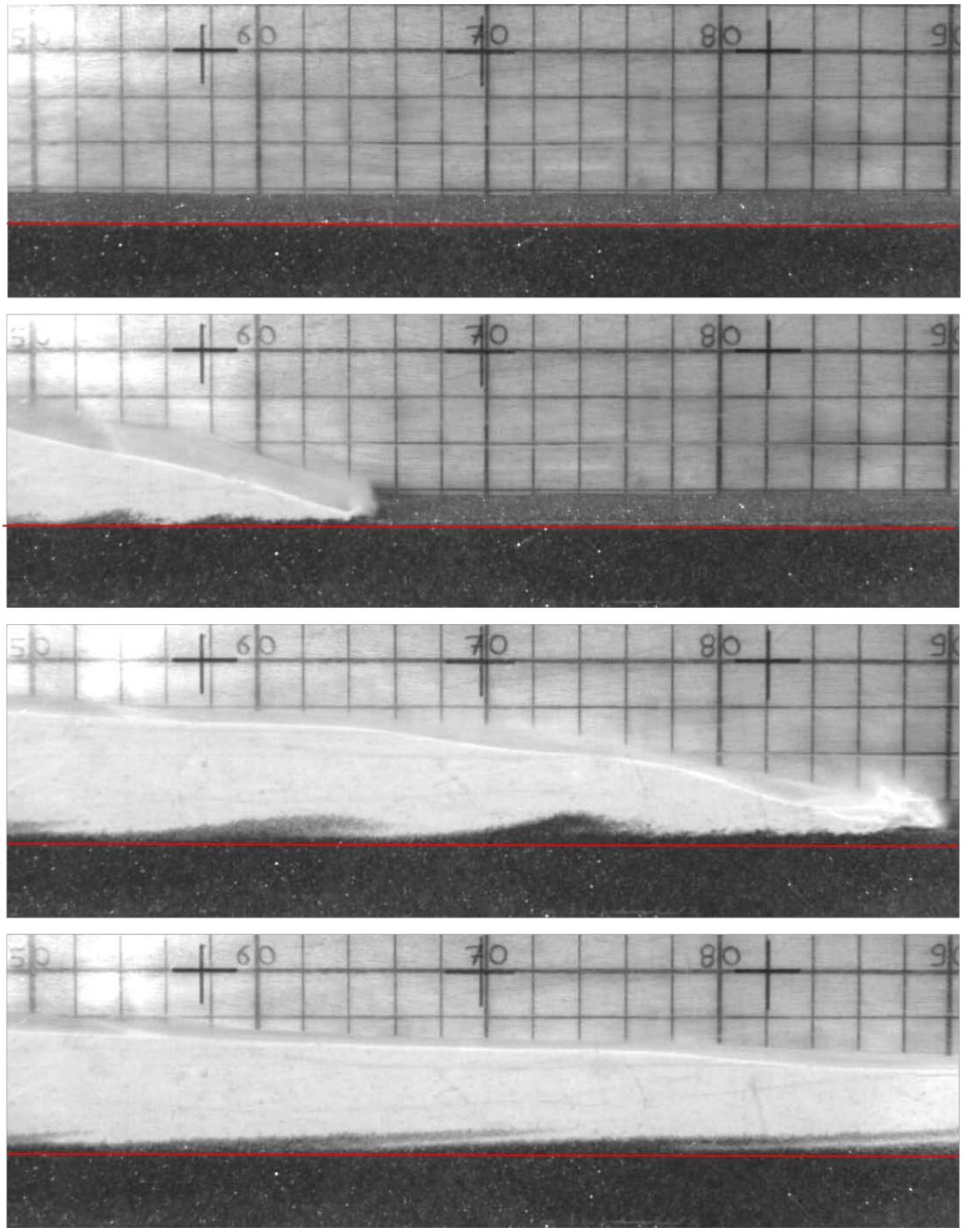

Appendix Figure 7. Experiment R34 - 10 slope, 700 micron bed, fluidized.

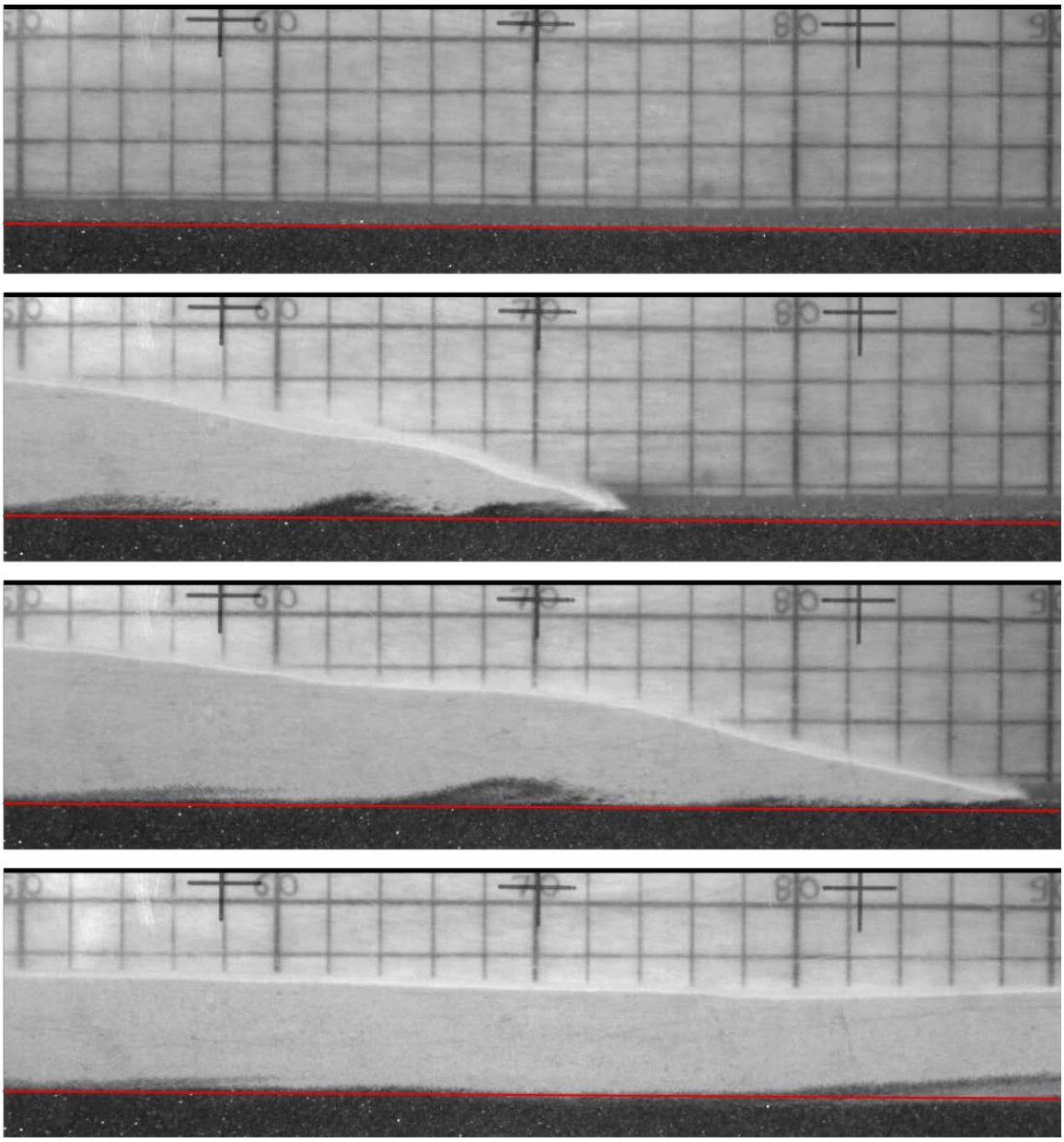

Appendix Figure 8. Experiment R49 - 15 slope, 700 micron bed, fluidized.

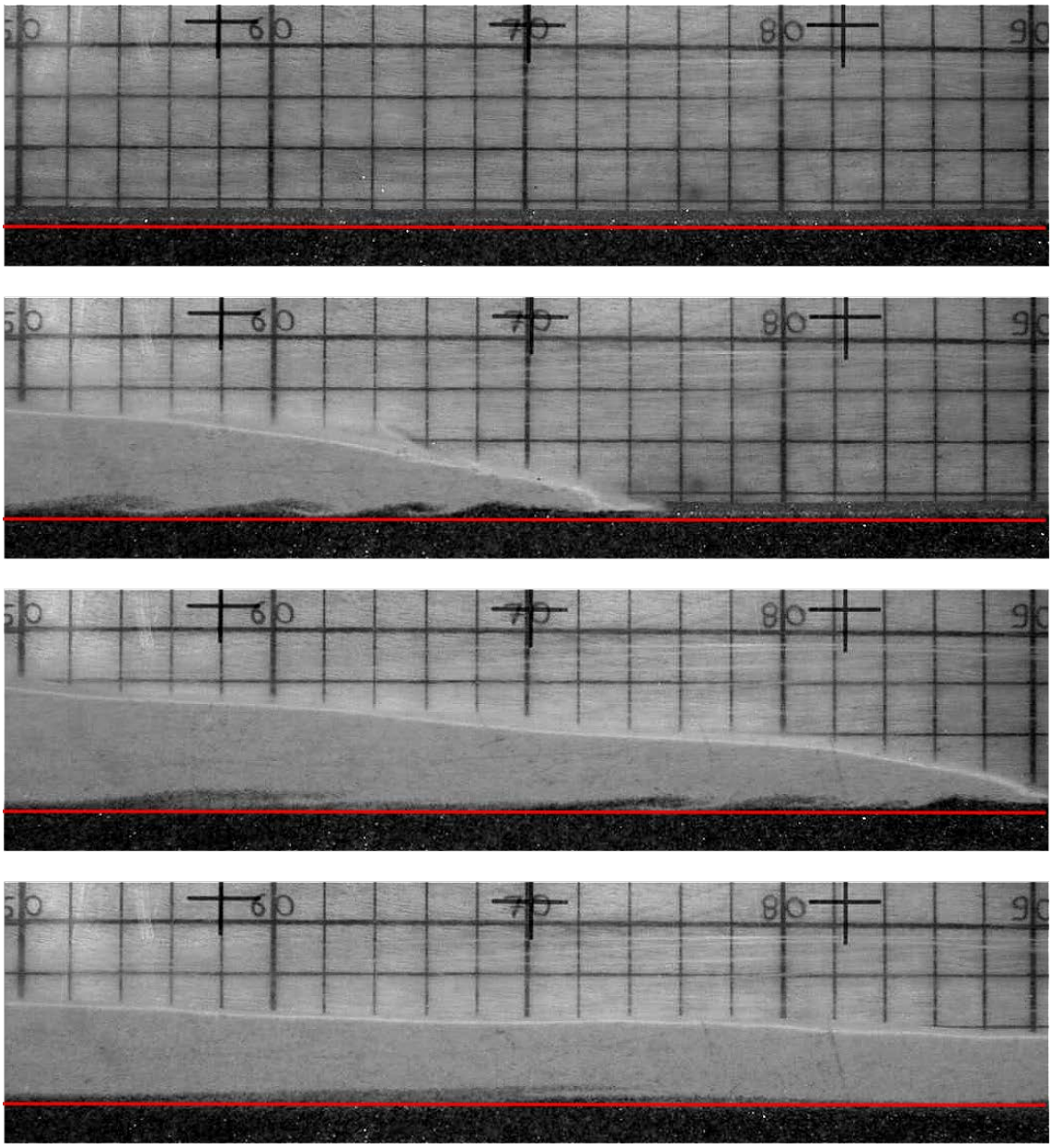

Appendix Figure 9. Experiment R52 - 15 slope, 500 mircon bed, fluidized.

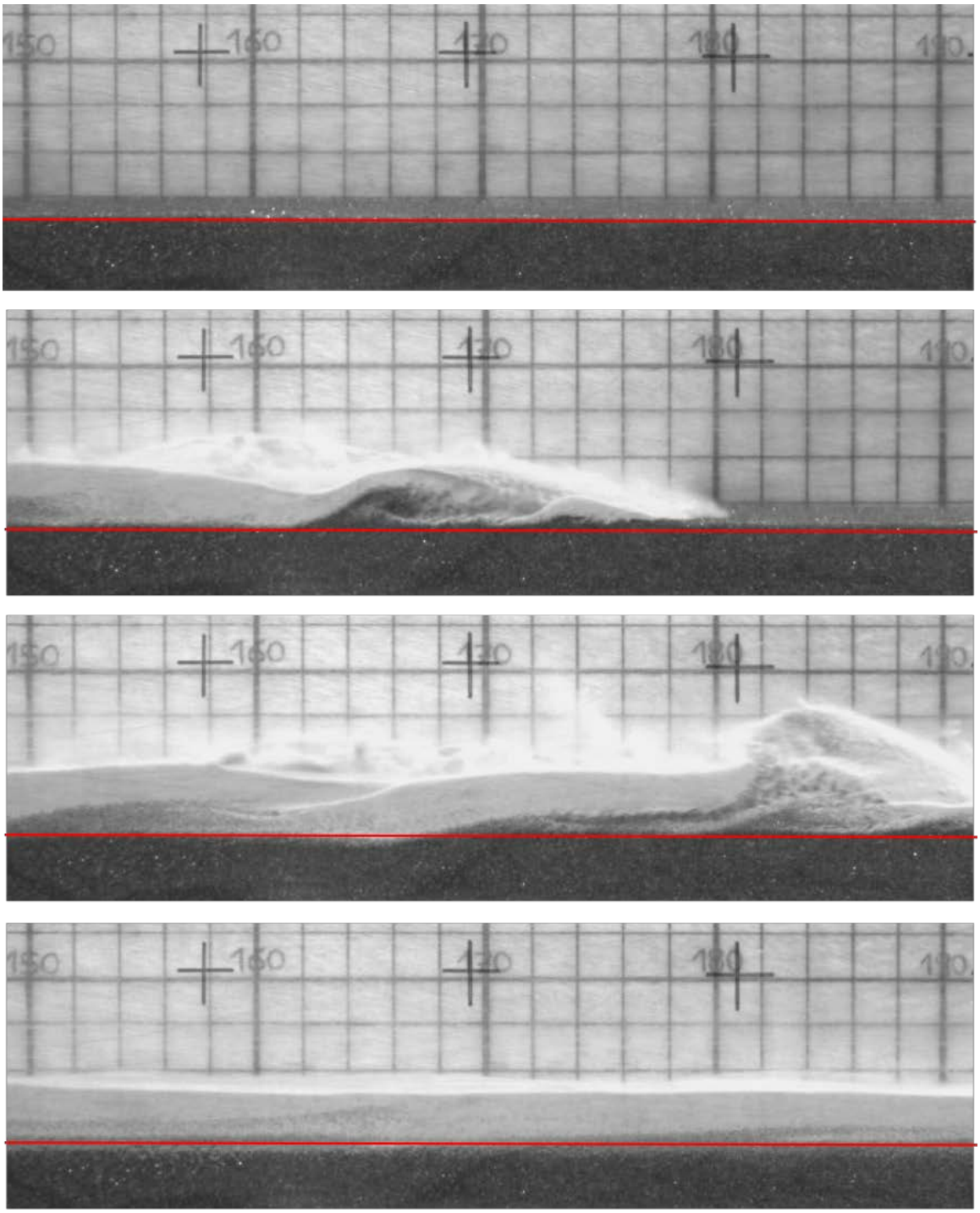

Appendix Figure 10. Experiment. R64 - 20 slope, 700 micron bed, fluidized.

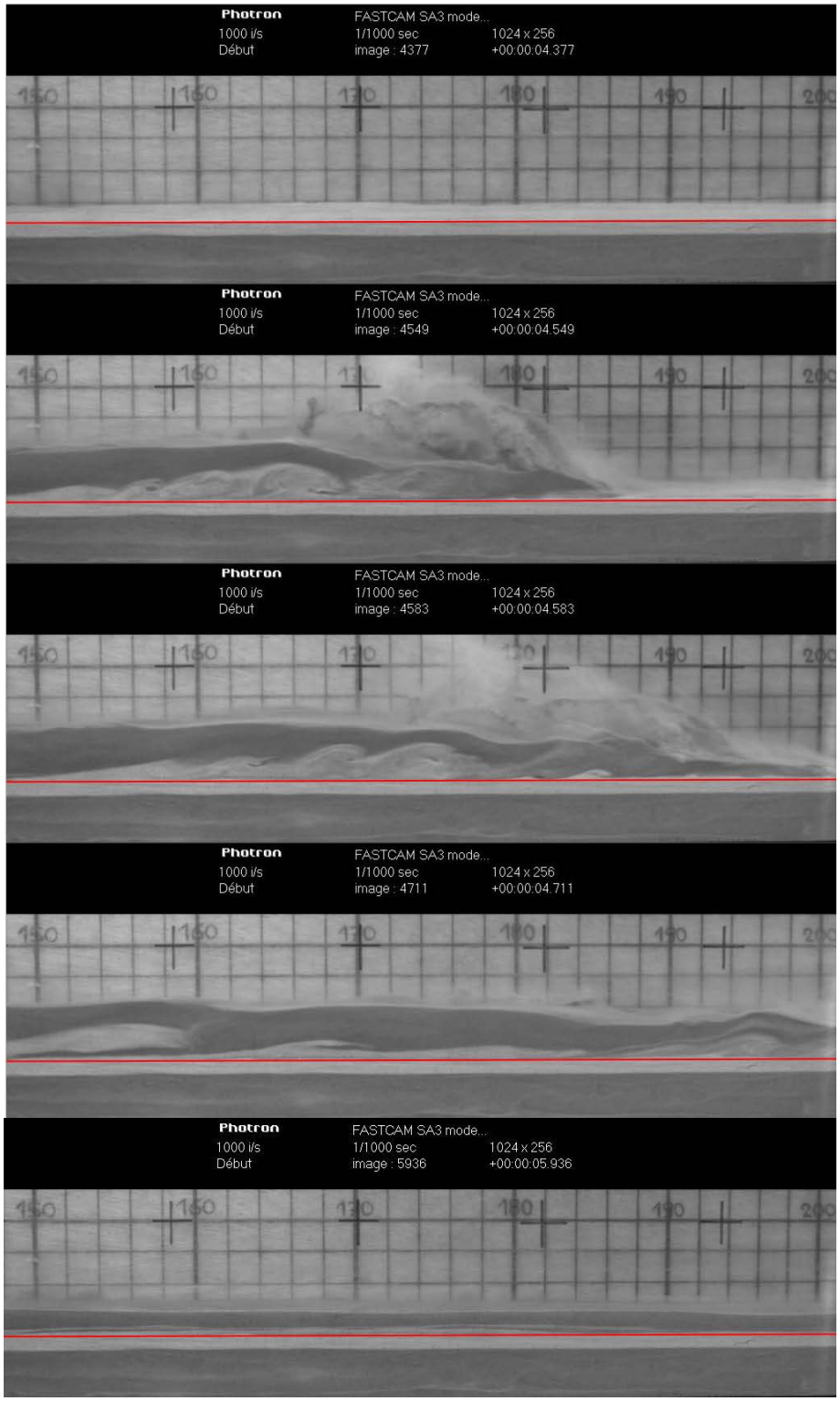

Appendix Figure 11. Experiment R77 - 20 slope, 40 micron bed, fluidized.

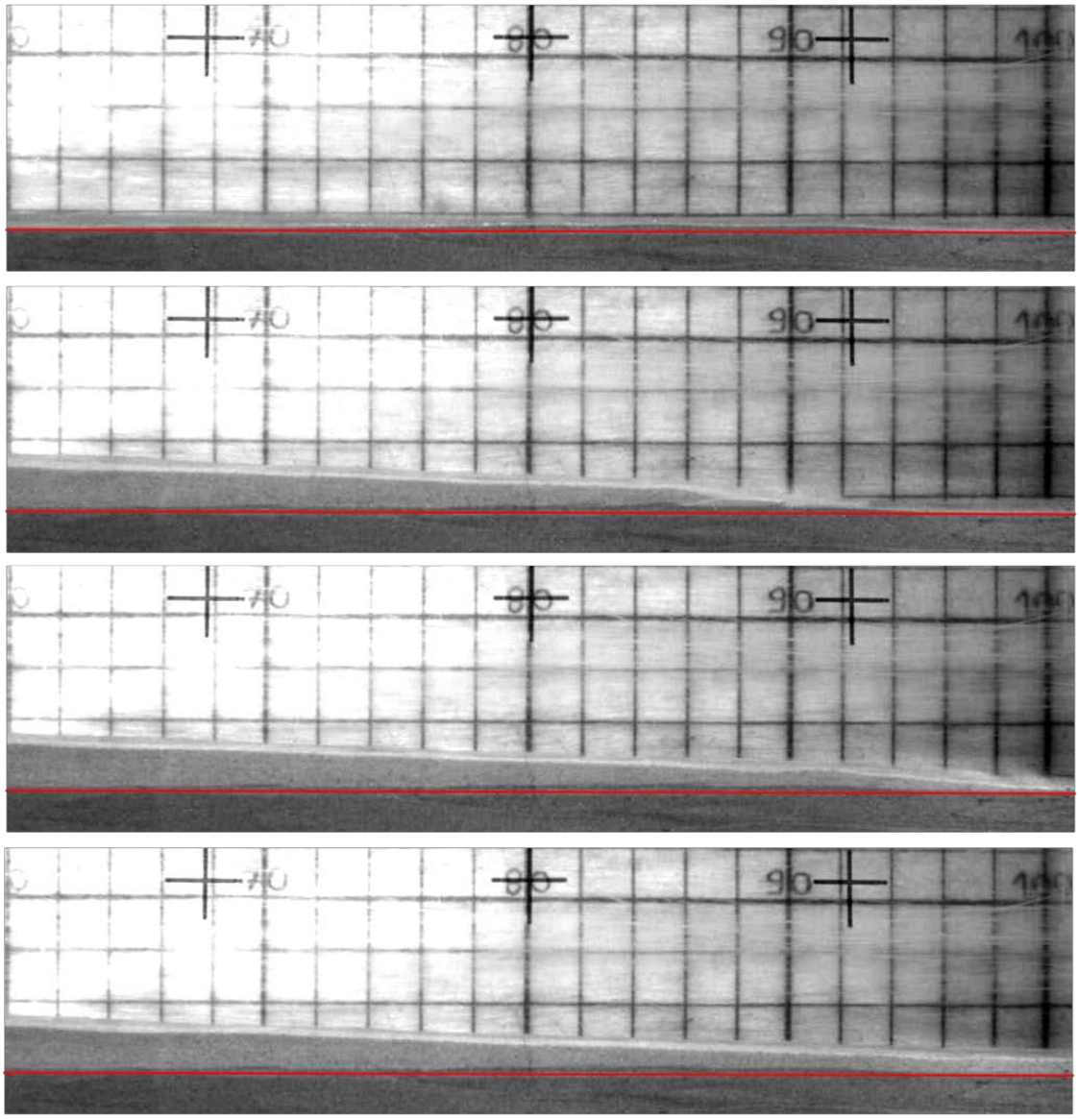

Appendix Figure 12. Experiment R107 - 10 slope, 80 micron bed, non-fluidized.

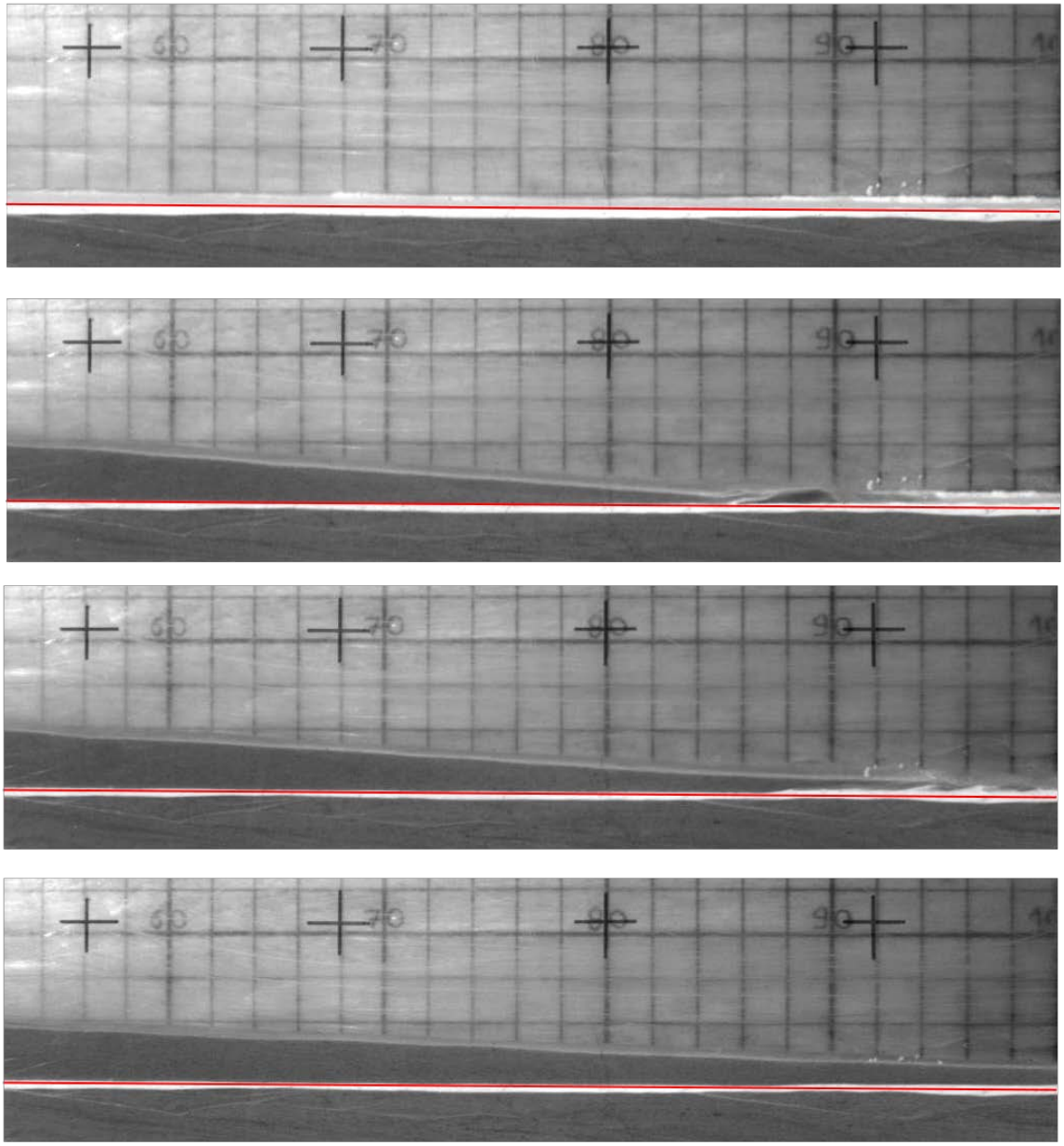

Appendix Figure 13. Experiment R108 - 10 slope, 40 micron bed, non-fluidized.

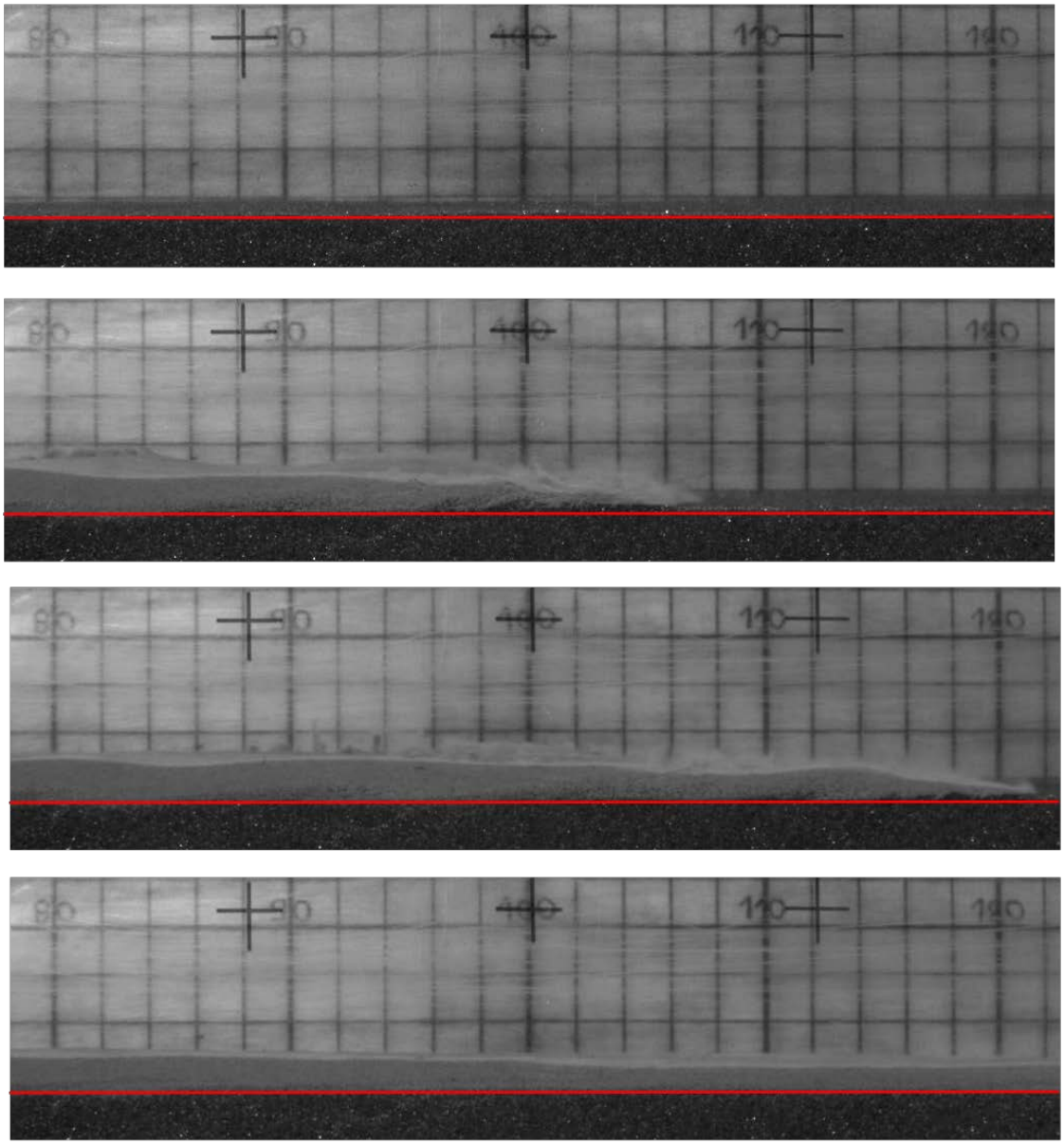

Appendix Figure 14. Experiment 109 - 10 slope, 700 micron bed, non-fluidized.

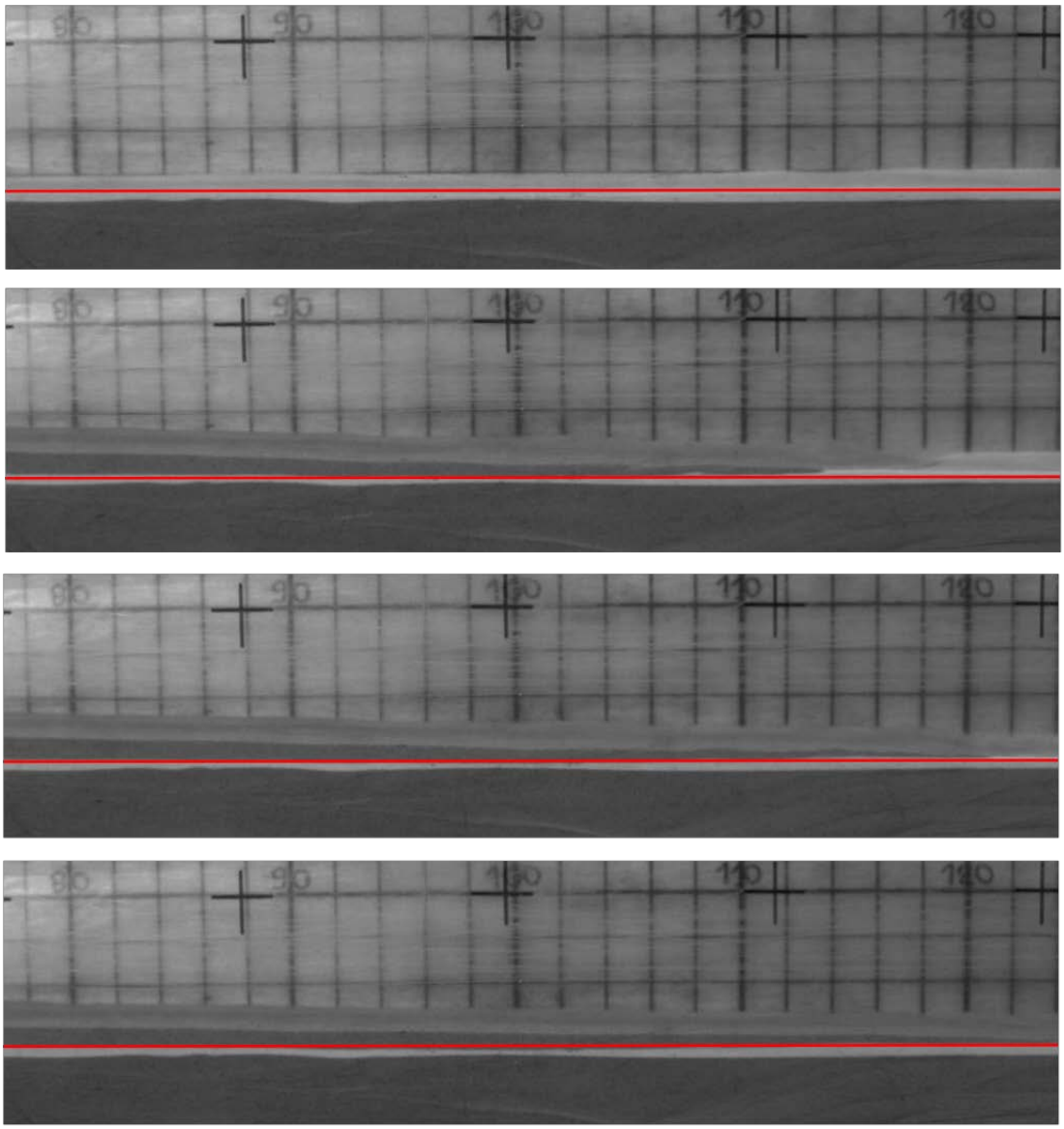

Appendix Figure 15. Experiment R110 - 15 slope, 80 micon bed, non-fluidized.

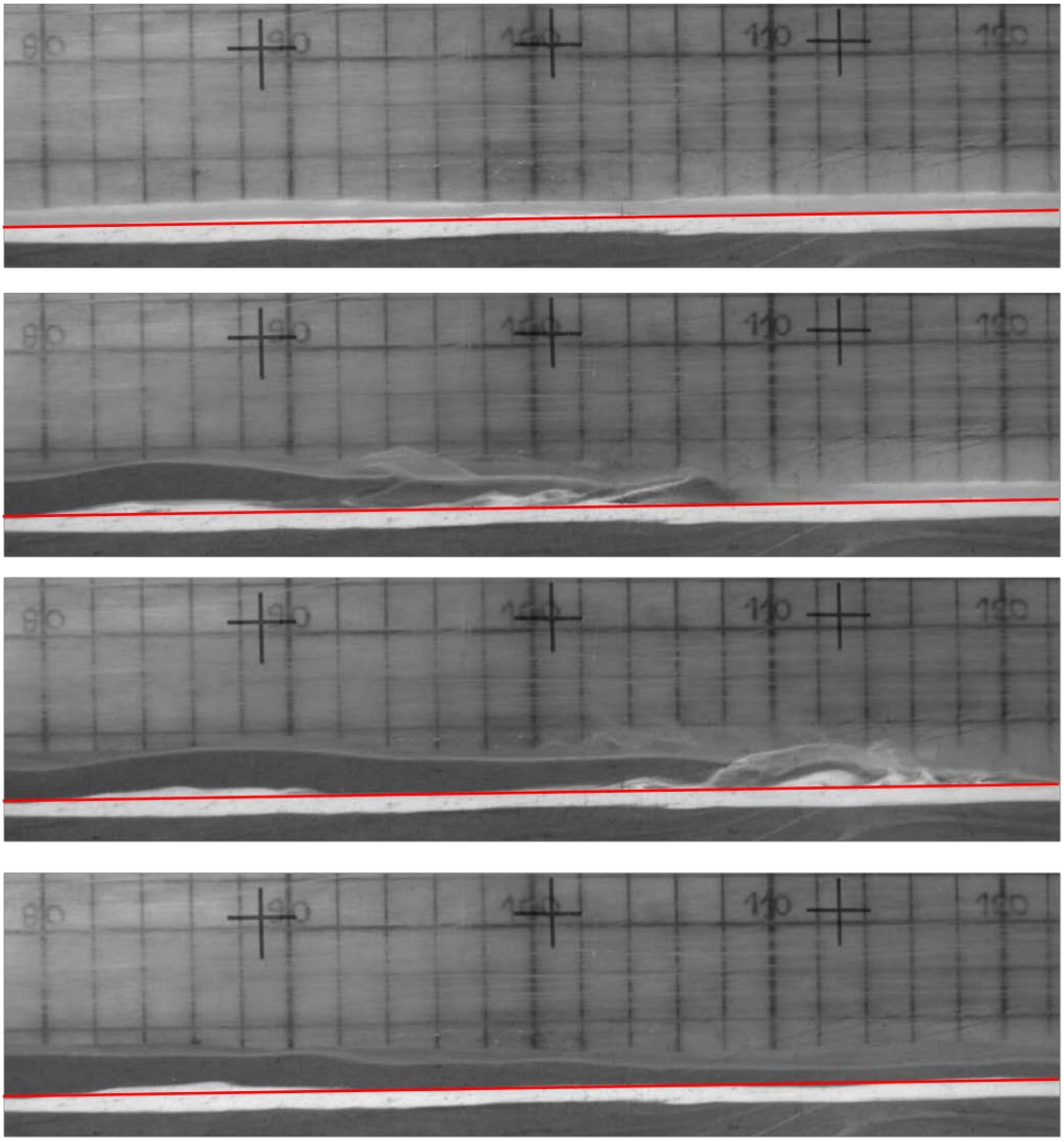

Appendix Figure 16. Experiment R111 - 15 slope, 40 micron bed, non-fluidized.

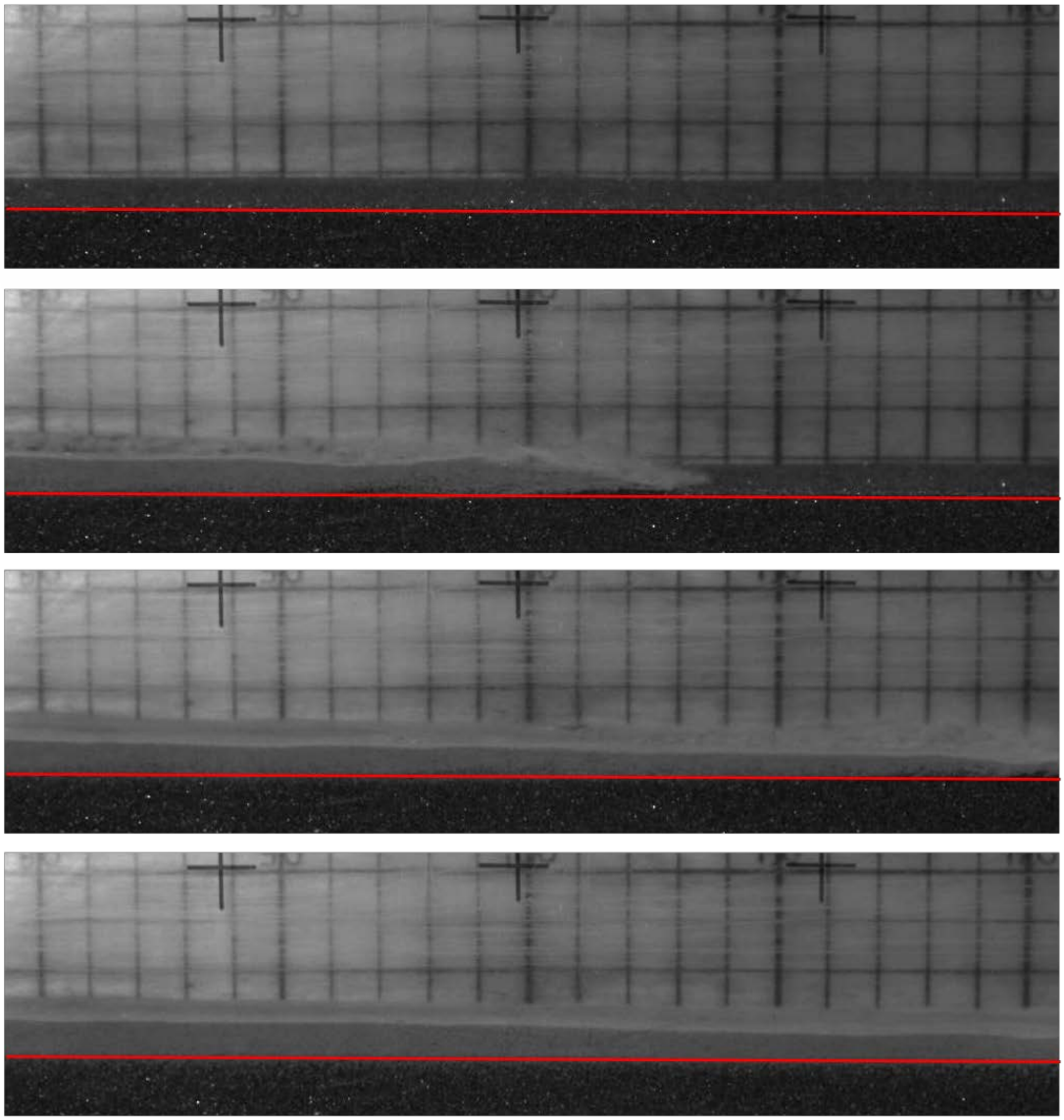

Appendix Figure 17. Experiment. R112 - 15 slope, 700 micon bed, non-fluidized.